UNIVERSITY OF CALIFORNIA SAN DIEGO

Assessing Myocardial Matrix Hydrogel Cellular Responses that Establish Tissue Repair

A dissertation submitted in partial satisfaction of the

requirements for the degree Doctor of Philosophy

in

Bioengineering

by

Raymond Ma Wang

Committee in charge

Professor Karen L. Christman, Chair
Professor Adam Engler, Co-Chair
Professor Sylvia Evans
Professor Toshiaki Kawakami
Professor Christian Metallo

2020

The Dissertation of Raymond Ma Wang is approved, and it is acceptable in quality and form for publication on microfilm and electronically:

_____

_____

_____

_____

_____

Chair

University of California San Diego

2020

TABLE OF CONTENTS

LIST OF ABBREVIATIONS

2D: Two-dimensional

ANOVA: Analysis of Variance Test

BMMC: Bone Marrow Derived Mast Cells

BrdU: Bromodeoxyuridine

BSA: Bovine Serum Albumin

DMEM: Dulbecco's Modified Eagle's Medium

DNA: Deoxyribonucleic Acid

DPBS: Dulbecco's Phosphate Buffered Saline

ECM: Extracellular Matrix

EDTA: Ethylenediaminetetraacetic Acid

EdU: 5-Ethynyl-2'deoxyuridine

FACs: Flow Cytometry Staining Buffer

FBS: Fetal Bovine Serum

H_2O_2: Hydrogen Peroxide

H&E: Hematoxylin and Eosin

HBSS: Hank's Balanced Salt Solution

HEPES: (4-(2-hydroxyethyl)-1-piperazineethanesulfonic Acid)

HMM: Human Myocardial Matrix

Hu-mice: Humanized Mouse

IFNγ: Interferon Gamma

IL: Interleukin

LV: Left Ventricular

MI: Myocardial Infarction

NDM: Non-Decellularized Myocardial Matrix

NK: Natural Killer

NSG: NOD.Cg-Prkdc^{scid}Il2rg^{tm1wjl}/SzJ (NSG)

OCT: Optimal Cutting Temperature

PBS: Phosphate Buffered Saline

PCM-1: Pericentriolar Material 1

PDGFR: Platelet-derived Growth Factor Receptor

PECAM: Platelet Endothelial Cell Adhesion Molecule

pHH3: Phosphohistone H3

PMM: Porcine Myocardial Matrix

PS: Penicillin Streptomycin

qRT-PCR: Quantitative Real-Time Polymerase Chain Reaction

RNA: Ribonucleic Acid

ROS: Reactive Oxygen Species

SDS: Sodium Dodecyl Sulfate

sGAGs: Sulfated Glycosaminoglycans

SMA: Smooth Muscle Actin

Th: T helper

TNF: Tumor Necrosis Factor

Tnnt: Troponin T

LIST OF FIGURES

LIST OF TABLES

ACKNOWLEDGEMENTS

I would like to thank my mentor, Dr. Karen Christman, Christman lab members, members of the Engler lab, and collaborators from the Dr. Sylvia Evans, Dr. Yang Xu, and Dr. Toshiaki Kawakami's labs, members of my committee, and friends at UCSD.

The Introduction. in part, is a reprint of the material as it is as it is published in: Raymond M. Wang and Karen L. Christman. "Decellularized myocardial matrix hydrogels: In basic research and preclinical studies." in Advanced Drug Delivery Reviews. 96, 77-82 (2016); and also, in part, is a reprint of the material as it is as it is published in Raymond M. Wang, Jingjin He, Yang Xu, and Karen L. Christman. Humanized mouse model for evaluating biocompatibility and human immune cell interactions to biomaterials. Drug Discovery Today: Disease Models *24*, 23–29. (2017); and also, in part, is a reprint of the material as it is published in the accepted book chapter: Raymond M. Wang and Karen L. Christman. "Biopolymers in the Treatment of Heart Failure and Cardiac Remodeling". In *Emerging technologies for heart diseases.* Elsevier Publishing Group. The dissertation author was a primary author of each of these works.

Chapter 1, in part is currently being prepared for submission for publication of the material. "Matrix material supporting a proliferative microenvironment for cardiomyocytes." Raymond M. Wang, Sylvia Evans, Karen L. Christman. The dissertation author was a primary author of this paper.

Chapter 2, in part, is a reprint of the material as it is published in: Raymond M. Wang, Todd D. Johnson, Jingjin He, Zhili Rong, Michelle Wong, Vishal Nigam, Atta Behfar, Yang Xu and Karen L. Christman. "Humanized mouse model for assessing the human immune response to xenogeneic and allogeneic decellularized biomaterials." Biomaterials 129, 98–110 (2017). The dissertation author was a primary author of this paper.

Chapter 3, in part is currently being prepared for submission for publication of the material. Raymond M. Wang, Toshiaki Kawakami, Karen L. Christman. "Mast Cells Contribute

to the Immunomodulatory Effect of the Biomaterial Microenvironment in a Gender Specific Manner.” The dissertation author was a primary author of this paper.

VITA

2013 Bachelor of Science in Biomedical Engineering and Biochemistry at Tufts University

2020 Doctor in Philosophy in Bioengineering at University of California San Diego

PUBLICATIONS

Wang RM*, Duran P*, and Christman KL. (2020) Chapter 1.3.6A Processed Tissues; In: Sakiyama-Elbert S (Ed) Biomaterials Science, Fourth Edition: An Introduction to Materials in Medicine. (*denotes equal contribution)

Wang RM, and Christman KL. (2020) Injectable Biopolymers in the Treatment of Heart Failure and Cardiac Remodeling; In: Nussinovitch U (Ed) Emerging Technologies for Heart Diseases; Volume 1: Heart Failure & Valvular Disorders.

Wang RM, He J, Xu Y, and Christman KL. (2017) Humanized mouse model for evaluating biocompatibility and human immune cell interactions to biomaterials. Drug Discovery Today: Disease Models *24*, 23–29.

Wang RM*, Johnson TD*, He J, Rong Z, Wong M, Nigam V, Behfar A, XY, and Christman KL. (2017) Humanized Mouse Model for Assessing the Human Immune Response to Xenogeneic and Allogeneic Decellularized Biomaterials. Biomaterials, *129*, 98–110. (*denotes equal contribution)

Wang RM, and Christman KL. (2016) Decellularized Myocardial Matrix Hydrogels: In Basic Research and Preclinical Studies. Adv Drug Deliv Rev, *96*, 77–82.

Sonnenberg SB, Rane AA, Liu CJ, Rao N, Agmon G, Suarez S, **Wang R**, Munoz A, Bajaj V, Zhang S, Braden, R.; Schup-Magoffin, P. J.; Kwan, O. L.; DeMaria, A. N.; Cochran, J. R.; Christman, K. L. (2015). Delivery of an engineered HGF fragment in an extracellular matrix-derived hydrogel prevents negative LV remodeling post-myocardial infarction. Biomaterials *45*, 56–63.

Lau JJ*, **Wang RM***, and Black III LD. (2014). Development of an Arbitrary Waveform Membrane Stretcher for Dynamic Cell Culture. Ann Biomed Eng *42*, 1062–1073.

Gershlak JR, Resnikoff JI, Sullivan KE, Williams C, **Wang RM**, and Black III LD. (2013). Mesenchymal stem cells ability to generate traction stress in response to substrate stiffness is modulated by the changing extracellular matrix composition of the heart during development. Biochemical and Biophysical Research Communications *439*, 161–166.

Zhang H, Nie S, Etson CM, **Wang RM**, and Walt DR. (2012). Oil-sealed femtoliter fiber-optic arrays for single molecule analysis. Lab Chip *12*, 2229–2239.

ABSTRACT OF THE DISSERTATION

Assessing Myocardial Matrix Hydrogel Cellular Responses that Establish Tissue Repair

by

Raymond Ma Wang

Doctor of Philosophy in Bioengineering

University of California San Diego, 2020

Professor Karen L. Christman, Chair
Professor Adam Engler, Co-Chair

Over the past several decades, coronary heart disease leading to myocardial infarction (MI) and subsequent heart failure has continued to the leading cause of death in the Western world and worldwide. Sudden death and limited renewal of cardiomyocytes post-myocardial leads to progressive expansion of tissue necrosis, negative left ventricular remodeling, and loss of function eventually causing heart failure. Treatments for end-stage heart failure, heart transplants and left ventricular assist devices, are hampered by healthy organ availability, limited medical resources, and negative impacts on patients' quality of life, thus prompting the need for novel therapies. Amongst hydrogel therapies, Injectable extracellular matrix (ECM) hydrogels derived from decellularized porcine left ventricular tissue have rapidly developed into

a leading injectable hydrogel therapy based on shown therapeutic potential post-myocardial infarction demonstrated in both small and large animal models. To continue developing this and general decellularized platforms, improved understanding of the underlying cellular mechanisms contributing to the observed myocardial repair is needed. Based on previous transcriptomic and histological assessments, further examination into the cellular response of cardiomyocyte and immune cell populations is studied to determine their involvement in the observed tissue repair. We show with pre-labeling methods to track events of DNA synthesis and proliferation in *in vivo* and *in vitro* models, respectively, that myocardial matrix material properties relevant to supporting proliferative characteristics in cardiomyocytes. Additional examination of immune cell populations has determined that the myocardial matrix supports a dynamic pro-inflammatory to pro-remodeling immune response indicative of induced tissue repair. Finally, we determined the involvement of mast cells in the biomaterial induced tissue repair, highlighting this understudied cell type for the field to consider when developing new biomaterial therapies.

INTRODUCTION

Cardiovascular Disease

Ischemic heart disease contributing to the development of myocardial infarction (MI and subsequent heart failure is the is both the leading cause of death in the western world[1] and worldwide accounting for 15.5% mortality in 2015[2]. Progression towards heart failure elicits changes to the 3D tissue structure from negative left ventricular (LV) remodeling and changes to the extracellular microenvironment due to extracellular matrix (ECM) degradation by increased matrix metalloproteinase activity and collagen deposition by myofibroblasts during scar formation[3]. Current solutions for the ever-growing patient population with end-stage heart failure are heart transplantation and LV assist devices[4]. However, the medical field is constantly under heavy demand for healthy donor tissue with over 10,000 patients added annually to the organ transplant waitlist, which was over 110,000 in the United States in 2016[5]. These methods are also hampered by burden on medical personnel and resources[6], and impact of patient quality of life [7], thus prompting the need for alternative therapies.

Importance of Biomaterial Bioactivity for Treating Cardiovascular Tissue Diseases

As opposed to replacing damaged tissue and function with heart transplant and LV assist devices, several therapies under investigation are designed to counteract mechanisms involved in negative LV remodeling and promote mechanisms of repair. The design versality and variety of material-based therapies has driven growing interest in their development for chronic tissue injury and disease treatments. Biopolymers are defined as naturally derived monomer subunits that combine through covalent bonds to form larger polymeric biomolecules such as proteins and polysaccharides[8]. These materials, in comparison to purely synthetic alternatives, provide favorable biocompatibility, biodegradability, and non-cytotoxic degradation products that are advantageous for translation to the clinic. However, synthetic materials offer greater control of specific material characteristics, thus, chemical alterations or composite

materials utilizing synthetic components are often utilized. In contrast to pharmacological and cellular therapies, biopolymers can provide physical, biomechanical, and biochemical cues in tandem for stimulating endogenous responses. Further advantages include longer retention at the site of deployment for more sustained treatment, and greater storage capability compared to cellular therapies given upstream culture and maintenance requirements[9]. The structure of biopolymers as porous scaffolds can further act as a vehicle for delivery of additional therapeutics promoting greater sustained delivery and retention. Material properties such as charge and sequestering ligands can further improve retention of factors within the material. These benefits and flexibility of the biopolymer platform allow for an assortment of potential approaches to develop novel therapies for treating heart failure.

Initial studies examined biopolymers in the heart for their potential to improve cell transplant survival. While this early work involving injection of fibrin glue did show an injectable biopolymer could improve cell survival, the most interesting result of these experiments were that the biopolymer alone (without cells) improved cardiac function[10, 11]. Since this time, numerous injectable biopolymers have been examined for treating MI and heart failure[12-15]. An early hypothesis in the field for the mechanism of action of such injectable biomaterials was that they acted as a structural support to increase wall thickness, thereby reducing wall stress. This thinking was based on the principles of the Law of Laplace where stress in the heart wall is perpetually increased from continued ventricular dilation and thinning of the LV wall during heart failure progression supporting cellular responses that promote pathological LV remodeling[16]. Alginate hydrogels have been the most extensively pursued based on this mechanism of action hypothesis leading to two that reached clinical trials, IK-5001 (originally named BL-1040) and Algisyl-LVR. However, clinical outcomes have been mixed and not fully reflective of the expected efficacy from preclinical testing similar to results with LV restraint devices, such as CorCap (NCT00630266)[17, 18] and HeartNet (PEERLESS-HF: NCT00291551, NCT00382863)[19-22], which were likewise developed as structural supports.

While modeling studies have suggested wall stress is reduced immediately following polymer injection[23-25], *in vivo* studies have suggested that this does not result in long term effects on negative LV remodeling[26, 27]. One issue with studies with biopolymers is that they all have some type of bioactivity, which makes it difficult to delineate their structural vs bioactive effects. For example, while IK-5001 was designed as a structural support, it also leads to increases in myofibroblasts[28]. In contrast, when a bio-inert poly(ethylene glycol) hydrogel was evaluated to specifically determine whether thickening of the heart wall and subsequent reduced heart wall stress based on the Law of Laplace provided therapeutic benefit, no benefits in cardiac function or reduction in negative LV remodeling was observed 6 weeks with magnetic resonance imaging post-injection compared to injection of saline despite an increase in wall thickness[26]. Other studies utilizing injections of calcium hydroxyapatite microspheres in carboxymethylcellulose gel carrier as a tissue filler for reducing local stress patterns in the infarct wall post-MI have similarly noted that these materials elicit a number of localized cellular responses that could be responsible for observed functional improvements from altered mechanotransduction[27].

Collectively, results from these studies and clinical trials have shown lack of translation efficacy based on the Law of Laplace hypothesis suggesting alternatives reasons likely explain the observed improved outcomes for alginate hydrogels at preclinical stages. Although designed around a physical and mechanical concept for mitigating negative LV remodeling, these therapies, ultimately, require downstream cellular responses to biomechanical cues from or elicited by these methods to promote endogenous repair. Qualities of substrate stiffness and dynamic forces in the extracellular environment have been shown to influence cell maturation, differentiation, and function[29-31]. One study directly compared methacrylated hyaluronic acid gels with different compressive moduli, similar and significantly greater than cardiac tissue stiffness ranging around 5 kPa and 45 kPa, respectively, in an ovine acute MI model[32]. Tissue evaluation found increased apical and basilar infarct wall thickness compared to nontreated

controls at 8 weeks post-MI. The higher stiffness material further had a significant decrease in infarct area at this timepoint, potentially from differences in mechanotransduction. However, no significant changes from echocardiographic measurements in normalized end-diastolic volume and end-systolic volume, ejection fraction, and cardiac output among the materials groups and infarct control were found at 2 and 8 weeks post-MI[32]. Alternatively, studies have suggested that maintaining biomechanical cues representative of the post-gestational cardiac tissue helps to sustain regenerative potential from these early development stages[33]. Therefore, while these materials are not commonly attributed for their bioactivity, delineating the relationship of altered biomechanical cues and material properties characteristic of induced cardiac repair at these preclinical studies is critical for determining whether this method is viable for successful clinical translation

Delving further into the concept of environmental cues influencing cellular responses, other biopolymers have alternatively focused on counteracting pathological signals from the damaged and unstable microenvironment during heart failure progression. In particular, the ECM, which is compositionally altered due to degradation and scar formation, plays a critical role in maintaining tissue homeostasis through both biomechanical and biochemical cues while destruction of this native microenvironment can be considered a hallmark of heart failure progression. Single component biopolymer platforms consisting of collagen[34], fibrin[10, 11, 34], and chitosan[35-38] were some of the initial demonstrations of biopolymer bioactivity alone contributing to lesser negative LV remodeling and improved cardiac function with favorable tissue responses such as being proangiogenic[34, 37, 38]. Notably, biopolymers derived from ECM proteins have mechanical stiffnesses lower than the native myocardium[39-41], further suggesting the material's bioactivity is the main contributor for inducing tissue repair rather than structural support to the tissue.

Immunomodulatory Influence of Biomaterials for Promoting Tissue Repair

The functionality of the immune system acting both as a protective barrier to foreign materials and a coordinator of tissue remodeling mechanisms makes it a critical response to evaluate for new biomaterial therapies. The immune response is a dynamic process involving recruitment, cytokine signaling, and phenotypic polarization of a plethora of cell populations. In particular, cell polarizations are considered indicators of the type of immune response elicited. For example, macrophage polarize between type 1 pro-inflammatory (M1) and type 2 pro-remodeling (M2) phenotype that correlate with the production of cytokines such as TNFα, IL-6, and IL-1β versus IL-12, IL-23, and IL-10, respectively[42]. Similarly, T-helper cells can polarize between type 1 (Th1) and type 2 (Th2) polarizations that release high levels of cytokines such as IL-2 and IFNγ versus IL-4, IL-5, IL-10, and IL-13, respectively[43]. Alternative categorizations of macrophage and T-helper cell polarization have also been designated based on their specific roles in the immune response[44, 45]. However, these strict designations are a classic and oversimplified representation of the *in vivo* immune response. *In vivo* responses also involve multiple states of polarized cells simultaneously, mixed phenotypic characteristics, and shifts in polarization over time based on environmental cues[46-48]. Changes to polarized response have been further associated with downstream tissue repair such as a dynamic M1 to M2 macrophage shift observed in healing tissue and enhanced biomaterial vascularization[49, 50]. Thus, proper controls and assessment of multiple markers at different timepoints during experimental evaluations are necessary to distinguish the overall response elicited.

Biomaterials modulate the immune response based on their biocompatibility and material characteristics. Immune cell populations respond to surface[51], physical[52], mechanical[53, 54], degradative[55, 56], and biochemical[57-59] material properties influencing the degree and timing of immune cell recruitment, subsequent polarization, and type of downstream tissue resolution. For non-biocompatible biomaterials, the immune response stimulates rapid recruitment and differentiation of immune cells leading to a high-density of pro-inflammatory polarized immune

cells to breakdown and reject the transplanted material. These cells include pro-inflammatory M1 macrophage, Th1 cells, natural killer (NK) cells, cytotoxic T cells, and foreign-body giant cells[60]. In contrast, biocompatible materials elicit milder immune cell recruitment along with alternatively polarized immune cell populations such as M2 macrophages and Th2 cells[61]. In comparison to bioinert materials that commonly form a fibrous capsule that walls off the material[62], bioactive materials seek to promote tissue ingrowth and endogenous repair mechanisms through these immune cell populations. Response of immune cells to biomaterial properties promote secretion of cytokines that influence downstream endothelial cell and fibroblast populations for promoting vascular development and restoration of a physiological ECM microenvironment[59, 63, 64]. Thus, the assessment of the immune cell populations can be utilized to determine whether specific downstream tissue remodeling resolutions will be effectively elicited by a biomaterial therapy.

Decellularized Myocardial Matrix Hydrogels for Eliciting Cardiovascular Repair

While research has attempted to combine different materials[65, 66] or incorporate naturally derived protein modifications[67] for improved efficacy, a major advancement in the creation of complex composite biopolymer materials is the development of decellularization methods to isolate the native ECM scaffold. As the ECM is heavily altered during heart failure, decellularized ECM materials provide a convenient shortcut to creating materials faithfully representative of the native extracellular microenvironment that is unattainable by current engineering methods. As these materials isolate the ECM itself, these materials can theoretically elicit a greater spectrum of tissue remodeling host processes and better represent the therapeutic efficacy of restoring extracellular cues from the healthy microenvironment. Decellularized ECM is isolated from tissue by detergents, enzymes, physical agents, and/or lysing and solubilizing solvents[68]. Further processing steps can also package the isolated ECM into various forms for delivery including patches, particles, particulates, and hydrogels. These

properties make isolated ECM an attractive platform for promoting physiological tissue remodeling as the ECM is known to influence numerous cellular responses including migration, proliferation, differentiation, metabolism, and maturation[69]. Since first demonstrated, a wave of research has produced decellularized ECM from various tissue sources to study their therapeutic potential for treating tissue diseases[12, 70].

Although numerous tissues could be attempted as sources for creating decellularized materials, theoretically, material derived from healthy myocardium would provide alternative tissue specific cues of the physiological extracellular microenvironment. The myocardial matrix hydrogel is a minimally invasive injectable hydrogel therapy made from decellularized porcine myocardium that can be delivered by percutaneous transendocardial injection. Safety and efficacy of myocardial matrix has been extensively supported in small murine animal and large porcine animal preclinical studies. Safety evaluations have been demonstrated for this material regarding hemocompatibility[71], favorable immune resolution[71], and being non-arrhythmogenic[72]. Hemocompatibility addressed concerns of potential leakage into the LV lumen as is common with transendocardial delivery and was determined to not cause platelet activation in human blood samples at standard concentrations with minimal activation at high concentrations tested[71]. Finally, testing by electrical stimulation through a pacing electrode determined that assembly of myocardial matrix hydrogels in cardiac tissue did not induce greater incidence of ventricular tachycardia compared to saline controls indicating the material was not proarrhythmogenic[72]; Holter monitoring post-injection in a porcine MI model likewise showed no evidence of arrhythmias[71].

Evaluations of efficacy in a rat ischemia reperfusion model treated by direct intramyocardial injection of myocardial matrix 2 weeks post-MI determined attenuation of negative LV remodeling and loss of cardiac function at 6 weeks post-MI compared to baseline values measured 1 week post-MI by magnetic resonance imaging[72]. In contrast, saline treated controls had significantly increased end-systolic volume and end-diastolic volume, and

decreased ejection fraction between 6 weeks post-MI and baseline values. In a large animal porcine MI model study, myocardial matrix was injected 2 weeks post-MI by transendocardial delivery performing 14-15 injections throughout the infarct area and borderzone based on guidance by NOGA mapping[71]. Assessments of matrix treatment versus saline or noninjected controls utilizing echocardiography showed significantly greater ejection fraction and global wall motion index, a measure of regional function, and lesser end-systolic volume and end-diastolic volume for myocardial matrix compared to controls measured at 3 months post-injection. Significantly less change in ejection fraction, end-diastolic volume, and end-systolic volume at 3 months post-injection from healthy pre-MI values were also determined for matrix treated compared to control animals. Change in end-systolic volume compared to pre-injection values was also significantly decreased compared to change in the control group. These preclinical studies have supported the investigation of myocardial matrix material at the clinical stage. Clinical evaluation of myocardial matrix hydrogels (VentriGel) has completed a phase I, open label and single group, clinical trial (NCT02305602) evaluate safety and feasibility in selected patients experiencing progression towards heart failure with an ejection fraction between 25-45%.

Along with determination of safety and efficacy of this material therapy, further research into the underlying mechanisms supporting the improved tissue conditions have also been investigated. Insight into the mechanism of action was provided by microarray analysis of myocardial matrix hydrogels versus saline controls in a rat ischemia reperfusion model treated 1 week post-MI[73]. This analysis determined early changes of numerous pathways including upregulation of vessel formation, oxidative metabolism, mitochondrial biogenesis, and cardiac development while apoptosis, hypertrophy, and fibrosis were downregulated. Confirmation by staining has determined significantly increased density of arterioles, c-kit+ cells, mast cells and PGC1α+, an energy metabolic marker, cardiomyocytes 1 week post-injection with significantly reduced interstitial fibrosis and hypertrophy based on cardiomyocyte area[73].

Immunohistochemistry analysis has also determined preservation of the damaged myocardium with significantly greater areas of cardiomyocytes retained in the infarcted tissue at 5 weeks post-injection in a rat ischemia reperfusion model compared to saline treated hearts[72]. Histological analysis of myocardial tissue isolated at the 3 month post-injection timepoint determined a significantly greater endocardial muscle layer and lesser infarct collagen content[71].

Scope of the Dissertation

Currently, myocardial matrix therapy has demonstrated bioactivity, safety and efficacy as a therapy post-myocardial infarction. As discussed in the previous section, analysis of the tissue has supported the tissue repair mechanisms that can be responsible for the observed repair. However, several of the observed results are not conclusive such as the potential of this material for forming new cardiac muscle and whether the influence on the immune response is further indicative of supported tissue repair. Furthermore, increased infiltration of mast cells is an unexpected observed result as these cells have most commonly been related to the allergy responses and pathological tissue remodeling. Several recent studies correlating mast cell presence with physiological tissue development and repair have raised questioned on whether mast cells play an expanded role in immune responses[74-76]. As a highly understudied cell type in the biomaterials, investigation into their contribution in biomaterial induced tissue repair could highlight another important cell type to focus on eliciting responses for biomaterial induced tissue repair. Based on these previous studies, our hypothesis for this thesis dissertation is that the myocardial matrix hydrogel supports tissue repair by promoting increased cardiomyocyte populations and modulation of the response of immune cell populations interacting with the material.

Thesis Goal and Outline

Chapter 1 examines whether myocardial matrix therapy post-myocardial infarction elicits responses *in vitro* and *in vivo* indicative of supporting cardiomyocyte renewal. We provide histological and transcriptional evidence that myocardial matrix material provides a microenvironment supportive of proliferative phenotypic characteristics of cardiomyocytes along with determination of material characteristics related to reactive oxygen species scavenger activity that could be responsible for these effects based on studies indicating reduction of oxidative stress maintains proliferative characteristics in cardiomyocytes.

Chapter 2 demonstrates the immune response of macrophages and T cells in wild-type and immune system humanized mouse model. From these assessments, we determined a dynamic polarization response from a pro-inflammatory to pro-remodeling phenotype of both macrophages and T cells indicative of induced tissue repair. Notably, the stronger response of human T helper cell subpopulations with type 2 dominant characteristics to porcine derived compared to human tissue derived material supports use of this xenogeneic material for clinical use. Finally, as this was the first demonstration of a biomaterial evaluation in a immune system humanized mouse model based on our literary reviews, this demonstrated the potential of this type of model for improved representation of the human immune response to biomaterial therapies.

Chapter 3 delves into investigation of the influence of mast cells on the immunomodulatory effects of myocardial matrix on surrounding immune cell populations. Through analysis of shifts in polarization in wild-type versus knockout and mast cell reconstituted rescue mice, this study demonstrated the importance of this cell type to proper polarization progression that deviated in a gender specific manner. The importance of this cell population for eliciting the expected physiological immune polarization progression supports further focus on this cell type for biomaterial induced tissue repair.

The final chapter summarizes the results of this dissertation and provides discussions on the contribution these results have on the overall scientific field. Finally, further potential work is also suggested based on these results that could provide improved understanding the underlying mechanisms supporting myocardial matrix and general biomaterial induced tissue repair.

Acknowledgements

The Introduction. in part, is a reprint of the material as it is as it is published in: Raymond M. Wang and Karen L. Christman. “Decellularized myocardial matrix hydrogels: In basic research and preclinical studies.” in Advanced Drug Delivery Reviews. 96, 77-82 (2016); and also, in part, is a reprint of the material as it is published in the accepted book chapter: Raymond M. Wang and Karen L. Christman. “Biopolymers in the Treatment of Heart Failure and Cardiac Remodeling”. In *Emerging technologies for heart diseases.* Elsevier Publishing Group. The dissertation author was a primary author of each of these works.

CHAPTER 1: Matrix material supports a proliferative microenvironment for cardiomyocytes

1.1 Introduction

Traditionally, the adult mammalian heart was considered to have no significant ability to regenerate damaged cardiac muscle tissue. However, studies in both mice and porcine cardiac injury models have determined that the mammalian heart during the fetal and immediate post-gestational neonatal stages can regenerate large regions of ligated ventricular myocardium without significant scar tissue formation[77-80]. These results have suggested that the mammalian heart had some mechanism of significant myocardium regeneration during early life stages that is rapidly lost with aging. Research determining shifts from expected ^{14}C content incorporation in health heart cardiomyocyte resulting from a pulse caused by increased atmospheric concentration from nuclear bomb testing provides potential evidence suggesting low levels of basal cardiomyocyte turnover maintained in adult human hearts. Turnover rates were estimated at less than 2% per year and decreased with age suggesting a mechanism of adult cardiomyocyte renewal[81]. Proliferative bursts at pre-adolescence have also been suggested[82, 83], however, difficulty replicating these results suggest raise questions on the validity of these results[84, 85].

Based on available cell sources, a dominant hypothesis suggests that either pre-existing cardiomyocytes or endogenous progenitor cells contribute to renewal in adult hearts. Research to determine why adult cardiomyocytes lose regenerative capability suggested cell cycle progression is arrested shortly after birth due to changes in hypoxia and metabolic demands of mature cardiomyocytes. Compared to fetal and neonatal hearts, adult heart tissue is less hypoxic making it more susceptible to oxidative DNA damage from heavy reliance on oxidative phosphorylation to support normal cardiomyocyte contractile activity[86]. Demonstrations of extensive cardiomyocyte dedifferentiation in zebrafish after cardiac injury[87] has also led to theories that hypoxic stress limits support for normal cardiomyocyte function eliciting an adaptive response by returning to an immature proliferative cardiomyocyte phenotype with lower

energy demands, lesser DNA damage and greater robustness[88, 89]. Dedifferentiation in mammalian cardiomyocytes has been demonstrated *in vitro* and *ex vivo* suggesting dedifferentiation could be inducible and potentially contributes minimally to native cardiac repair[90]. Based on these principles, hypoxia fate mapping techniques found proliferative cardiomyocytes in hypoxic heart regions, termed Hif-1α cardiomyocytes. These cardiomyocytes maintain immature characteristics and turnover rates similar to previously determined rates in human hearts suggesting their contribution[91]. Studies have also suggested involvement of endogenous progenitor cells populations native to the heart[92] or from alternative cell populations[93]. However, studies utilizing lineage tracing methods bringing into question the validity of the cardiomyocyte progenitor marker, c-kit, [94, 95] have led to investigation that determined the falsity and retraction of the initial studies supporting the use of c-kit as a cardiomyocyte progenitor marker.

Studies have tried to determine whether these endogenous cell populations can be induced to support repair post-MI. Investigation in the adult mice hearts post-MI produced conflicting results on whether pre-existing cardiomyocyte or progenitor cell populations formed new cardiomyocytes[96, 97]. However, results were hindered by low cell numbers considering limited native repair in the adult heart. Clinical results with cardiosphere-derived cell therapies found significant increases in cardiac muscle mass in treated patients based on magnetic resonance imaging analysis[98]. Further investigations in transgenic mouse models showed minimal cardiosphere-derived cell engraftment after one to two weeks and evidence of cardiomyocyte formation from both cardiomyocytes and endogenous progenitor cells, suggesting some paracrine mechanism based repair response[99].

Similar to cardiosphere-derived cell results, an increased endocardial muscle layer was observed in a disease pig model treated two weeks post-MI with myocardial matrix hydrogels when evaluated 3 month post-injection. In contrast, saline injected and non-treated controls contained minimal cardiac muscle[100]. Larger clusters of cardiomyocytes within the infarct region

in myocardial matrix versus saline groups were also observed in MI rat models after 4 weeks post-injection[72]. Mechanistic evidence from microarray analysis supported that myocardial matrix promotes reduced cardiomyocytes apoptosis, shifted cardiac metabolism and greater cardiac development[73]. Previous *in vitro* experiments also demonstrated that myocardial matrix promotes cardiomyocyte viability under oxidative stress. Since previous research suggests hypoxia favors an immature cardiomyocyte phenotype[86], preservation in the hypoxic infarct environment might support survival of Hif-1α cardiomyocytes and/or dedifferentiation of mature cardiomyocyte[88] that proliferate to form new cardiomyocytes. However, previous *in vitro* work determined myocardial matrix also supports cardiac progenitor cell growth and differentiation[101]. These observations and possibilities have investigation of whether PMM treatment is supportive of cardiomyocyte renewal from pre-existing cardiomyocyte populations.

1.2 Results

1.2.1 Confirmation of PCM-1 as a cardiomyocyte nuclei specific marker

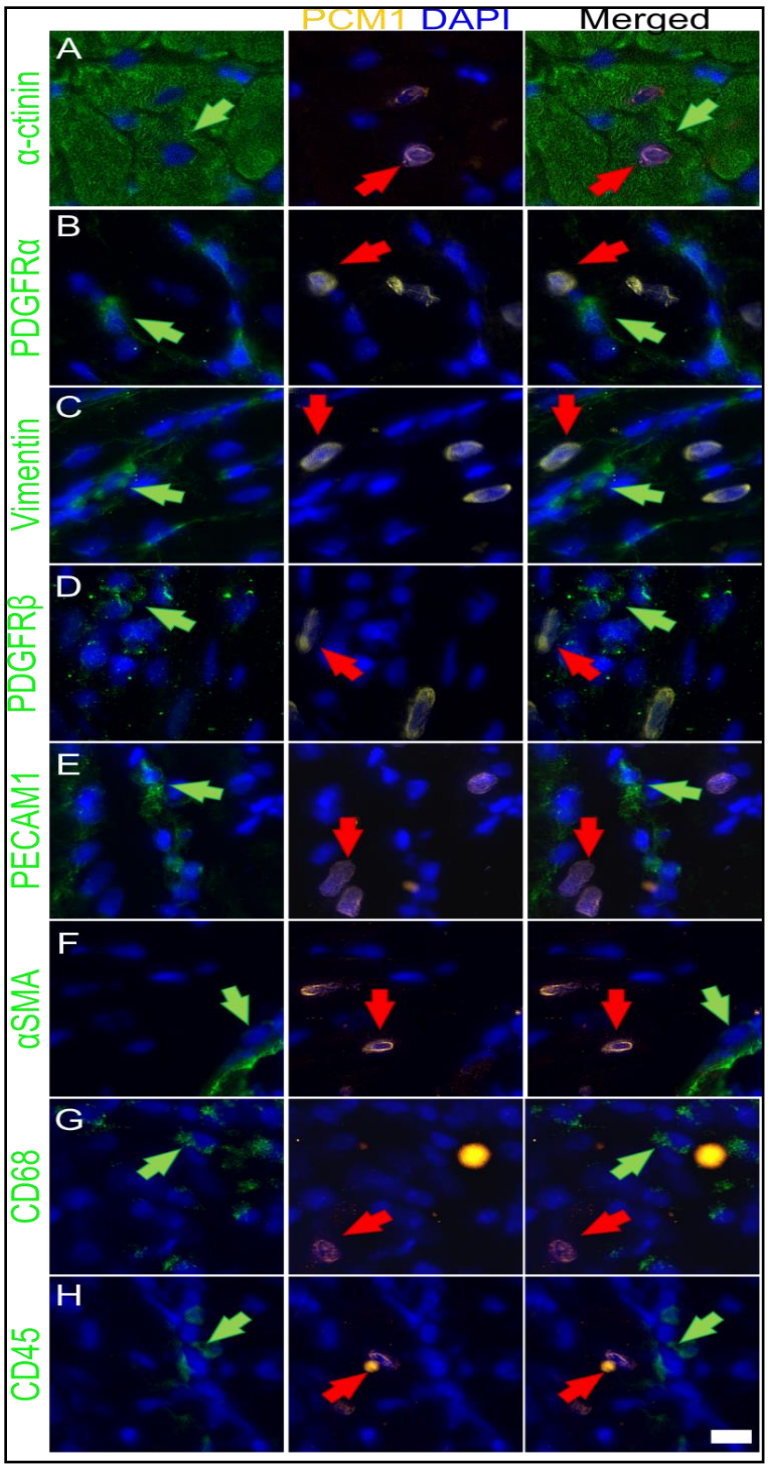

Figure 1.1: Validation of PCM-1 Cardiomyocyte Nuclei Specificity. (A-H) Representative images showing PCM-1 labeling overlaps with a cardiomyocyte marker (A) and lack of overlap with non-cardiomyocyte cell type markers (B-H). Left column shows staining with the marker listed on the left (green). Middle column shows PCM-1 staining (orange). Right column shows merged image. Nuclei staining (blue) is present in all images. Positive staining is indicated with an arrow. Scale bar is 10 μm.

As a method for tracking events of DNA synthesis and potential cardiomyocyte proliferation, thymidine analog incorporation and co-labeling with a cell specific marker is a commonly used for *in vivo* assessment. However, utilizing common cardimyocyte cytoplasmic stains such as Troponin T (TnnT) or α-actinin has risks of determining false positives due to the high cellular density and potential for overlapping cellular nuclei in the injured cardiac tissue. To address this issue, a previously described cardiomyocyte nuclei marker, pericentriolar material 1 (PCM-1)[81, 102], was selected. PCM-1 has been used in mice and human cardiomyocyte studies, but has not been extensively validated for cardiomyocyte nuclei staining in rat tissue[102]. PCM-1 was co-stained in rat heart tissue sections with another CM marker (α-actinin) along with markers for fibroblasts (PDGFR-α, vimentin), endothelial cells (PECAM-1), smooth muscle cells (α-SMA), immune cells (CD68, CD45). Results showed overlapping co-stain with α-actinin and no co-labeling with non-cardiomyocytes markers confirming PCM-1 is a cardiomyocyte nuclei specific marker[103] (Figure 1.1A-H). Further validation was performed with an alternative cardiomyocyte nuclei marker, Nkx2.5 showing colocalization of the two stains supporting specific labeling with PCM-1 (Figure 1.2). As PCM-1 further has a distinct pattern outlining the border of cardiomyocyte nuclei that makes it better for identifying a cardiomyocyte amongst overlapping nuclei, PCM-1 was selected for subsequent analysis of cardiac tissue for thymidine analog incorporation.

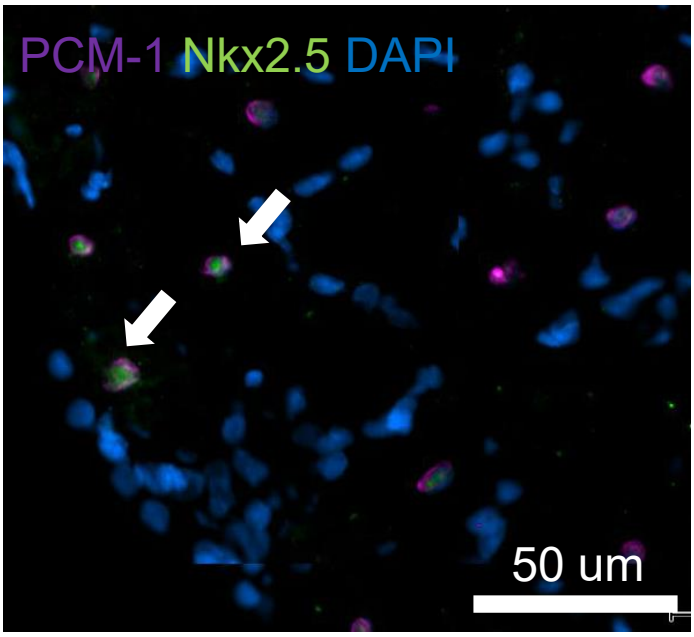

Figure 1.2: Costaining of PCM-1 and Nkx2.5 in cardiac tissue. Representative image of PCM-1 (magenta) and Nkx2.5 (green) stained in infarcted heart tissue samples demonstrating colocalization (white arrow) that was observed throughout the tissue.

1.2.2. Assessment of infarct size for assessing infarct size consistency

For analysis, hematoxylin and eosin staining and quantification of percent infarct area was performed to assess for outliers that should be excluded from subsequent analysis. From this assessment, two hearts (one from each group) were immediately excluded due to lack of visible infarct. The remaining hearts (n = 7 per group) were quantified by highlighting the infarcted area, tissue area (left ventricle and septum), and excluding area of the lumen for that section and recording pixel areas for regions of interest (Figure 1.3A). Sections for analysis were selected by identifying the location with the largest identified infarct and selecting two locations outward from that location. Based on this analysis, no outliers were determined within each group and differences in average infarct size were determined to be not significant (Figure 1.3B). Thus, these hearts were carried over for subsequent analysis.

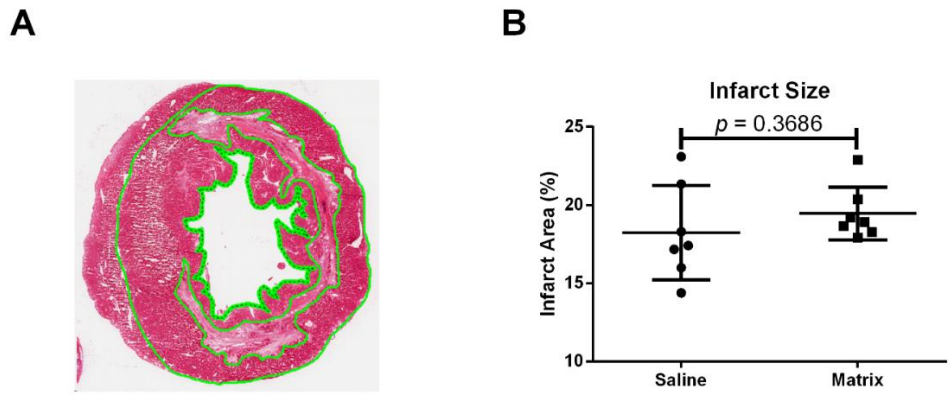

Figure 1.3 Percent infarct size analysis. (A) Image of analyzed heart for percent infarcts by highlighting (green) of the infarcted area, tissue area including left ventricle and septum, and the lumen area. (B) Quantified percent infarct size of the matrix versus saline treated hearts.

1.2.3 *In vivo* incorporation of thymidine analog in cardiomyocyte nuclei

For analysis of thymidine analog uptake, co-staining of EdU or BrdU with PCM-1, cardiomyocyte nuclei specific marker, was performed in the infarct and borderzone region. For consistently, the borderzone was identified by highlighting the infarct region in stained sections and expanding outwards from this highlighted region by 750µm. Analysis of these two regions identified co-staining mainly in the borderzone region (Figure1.4A) with no significant difference in the infarct region (Figure 1.4B) and a significantly increased $EdU^+PCM\text{-}1^+$ density only in the borderzone region of matrix treated hearts versus saline treated hearts (Figure 1.4C). Similarly, staining for $BrdU^+PCM\text{-}1^+$ cardiomyocytes were mainly identified in the borderzone region (Figure 1.4D). Significance was not found from $BrdU^+PCM\text{-}1^+$ analysis in the borderzone regions (Figure 1.4E) and no $BrdU^+PCM\text{-}1^+$ cardiomyocytes were found in the infarct region.

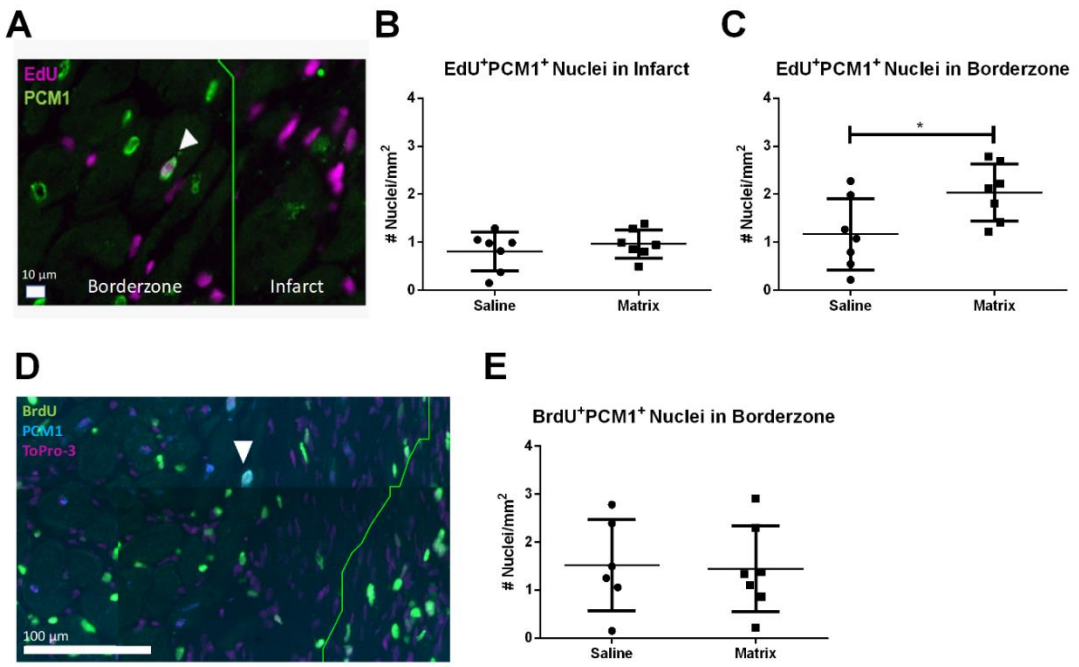

Figure 1.4: Thymidine analog uptake in cardiomyocyte nuclei. (A) Image of nuclei co-stain of thymidine analog EdU (purple) and cardiomyocyte nuclei specific marker PCM-1 (green) labeled by a white arrow. Density EdU+PCM-1+ nuclei in the (B) infarct. (C) infarct borderzone. (D) Image of nuclei co-stain of thymidine analog BrdU (green) and cardiomyocyte nuclei specific marker PCM-1 (blue) labeled by a white arrow with ToPro-3 nuclear counterstain. (E) Density BrdU+PCM-1+ nuclei in the infarct borderzone. (*$p < 0.05$, unpaired Student's t-test)

1.2.4. Lack of Early Burst of Thymidine Analog Positive Cardiomyocytes with Matrix Treatment and Limitations of Common Standard Proliferative Markers

Validation of thymidine analog incorporation is needed as positive staining could be indicative of alternative mechanisms such as DNA repair instead of cell cycle progression. As thymidine analog uptake was observed to be increased during the earlier timespan, a set of animals (n = 15) following a similar surgical procedure, but delivering EdU only for a week post-MI was processed similar to the previous set of animals. However, analysis of these animals determined no significant differences between saline and matrix treated animals (Figure 1.5A) suggesting that the matrix induced a gradual increase in EdU positive cardiomyocytes. Additionally, follow-up utilizing proliferative markers such as phosphohistone H3 (pHH3) was hindered based on observation of high number of positively stained cardiomyocytes in healthy

rat tissue, which suggests questionable interpretation of these staining methods in rat tissue for this examination (Figure 1.5B).

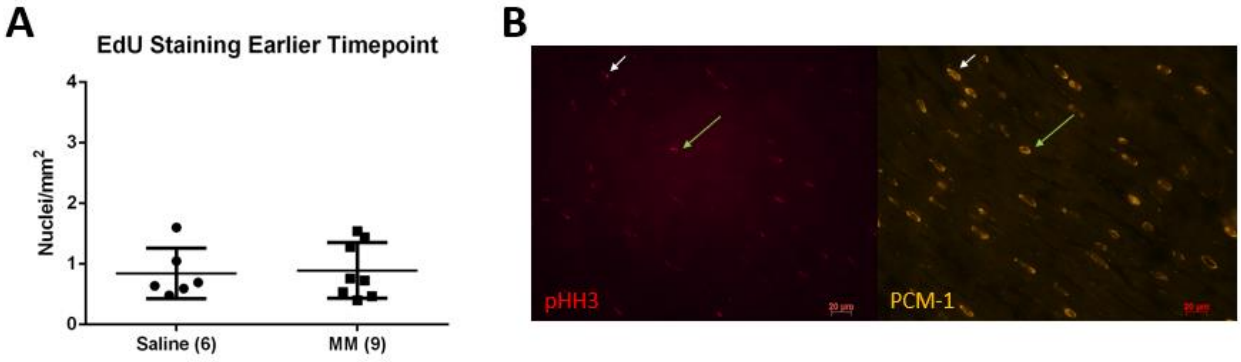

Figure 1.5: Non-specific staining of pHH3 staining. Density $EdU^{+}PCM\text{-}1^{+}$ nuclei in the (A) borderzone in saline and matrix treated hearts with 7 days of EdU labeling post-myocardial infarction. (B) Representative images showing several incidents of positive staining of a proliferative marker with cardiomyocytes in healthy rat tissue suggesting issues with false positive determination with these methods.

1.2.5. Increased proliferation of *in vitro* encapsulated neonatal cardiomyocytes

As our assessment of our material stimulating proliferative characteristics was limited utilizing standard staining of proliferative markers for rat tissue, we studied the response of cell interacting with our material for determining whether myocardial matrix stimulated increase cardiomyocyte proliferation. Utilizing CellTrace™, proliferation based on dye dilution into progeny was utilized to confirm whether cardiomyocyte underwent increased incidents of cytokinesis when encapsulated in our myocardial matrix material. Gating for analysis of progeny by dye dilution on a flow cytometer was confirmed by pre-labeling of cardiac cell populations in 2D culture on tissue culture plastic. Sample was collecting during various steps of the cell processing and after days of culture (Figure 1.6A). For specific determination of live cardiomyocytes, LIVE/DEAD™ Aqua and previously validated PCM-1 stained was utilized. Gating for PCM-1 flow cytometry was validated by fluorescent minus one and IgG isotype control (Figure 1.6B). Analysis of encapsulated cardiomyocytes with these optimized gates determined a significant decrease in the original generation 1 cardiomyocyte population and a

significant increase in cardiomyocyte progeny of the third generation relative to progeny distribution in collagen controls demonstrating increased proliferative characteristics of neonatal cardiomyocytes were maintained (Figure 1.6C).

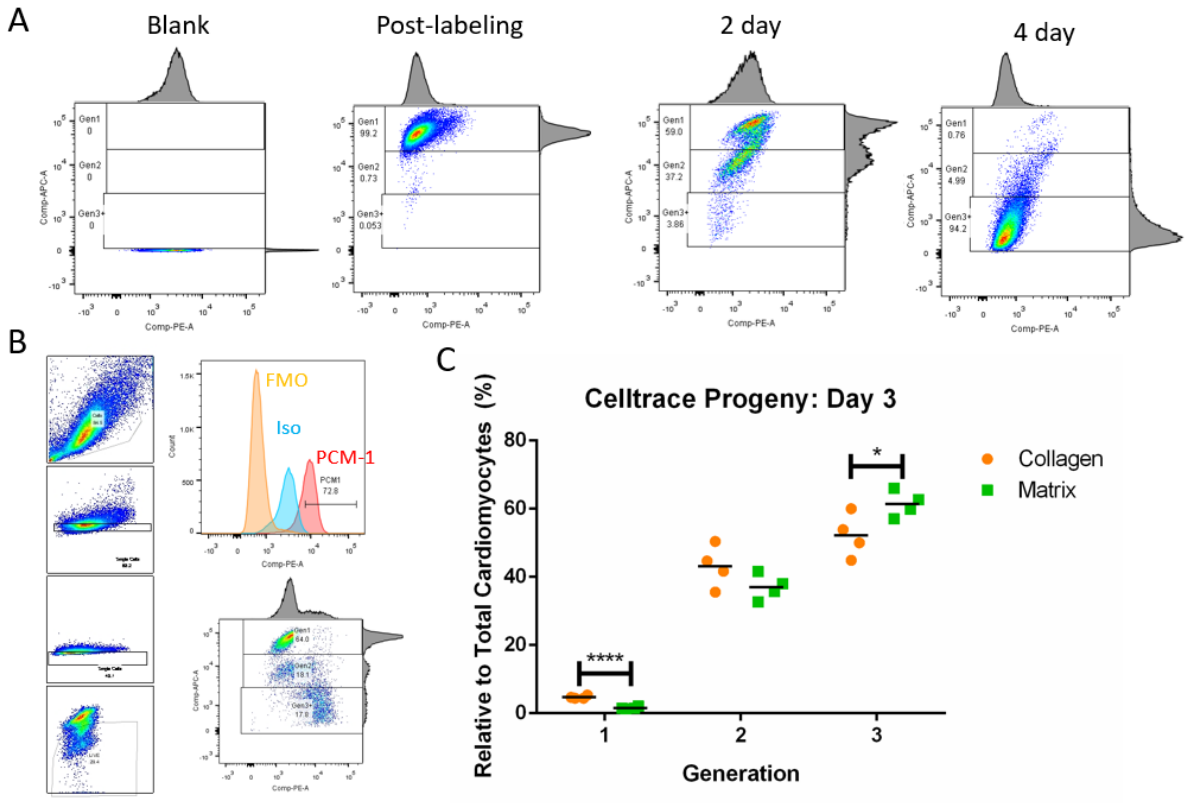

Figure 1.6: Increased cardiomyocyte progeny with encapsulation in myocardial matrix. (A) Samples for optimizing gating for proliferative analysis based on CellTrace™ FarRed. Gating was based on non-label cells, immediately labeled cells, pre-labeled cells following 2 days of culture, and 4 days of culture demonstrating distinct clustered dye dilution representing increased generation of progeny. (B) Representation gating scheme for distinguishing live singlet cells based on forward and side scatter and LIVE/DEAD™ Aqua signal. PCM-1 gating with fluorescence minus one and isotype control peaks for distinguishing the cardiomyocyte positive peak and distribution of progeny. (C) Percentage of cardiomyocytes over two progeny generations after 3 days of culture encapsulated in collagen or myocardial matrix hydrogels. *p< 0.05, ****p< 0.0001).

1.2.6. Decellularized Myocardial Matrix Function as a ROS Scavenger

Matrix interaction with ROS was examined based on studies demonstrating that reduced oxidative stress promotes proliferative characteristics in cardiomyocytes during the neonatal and

adult stages [104-106]. Incubation of H_2O_2 myocardial matrix hydrogels versus collagen gel controls over a time course study. Measurements over 5 days was also taken showing a significantly continuing decrease in H_2O_2 concentration for the myocardial matrix versus both PBS and collagen controls. Collagen also had a significant decrease to PBS, though the difference plateaued after a day, while H_2O_2 in PBS was relatively consistent (Figure 1.7A). Further confirmation and relative strength to an antioxidant reagent was assessed with a Cayman Chemical's Antioxidant Assay kit for comparison with antioxidant Trolox standard. In comparison to scavenger activity of Trolox, a 0.240 ± 0.0215 mM for 0.06mg myocardial matrix or 4.00 ± 0.359 mM Trolox/mg myocardial matrix compared to 0.0255 ±0.0627 for 0.025mg collagen or 1.02 ± 0.84 mM Trolox/mg collagen (Figure 1.7B). As myocardial matrix is a mixture of proteins, general ROS scavenger activity of protein mixtures is commonly linked to specific chemical groups such as thiol groups found in available cysteine amino acids. Utilizing a Cayman Chemical® Thiol Detection Assay Kit, thiol content was determined based on a glutathione standard curve, which similarly showed around a 4x amount compared to collagen of 75.77 ± 13.16 nmol/mg myocardial matrix versus 21.96 ± 10.16 nmol/mg collagen (Figure 1.7C).

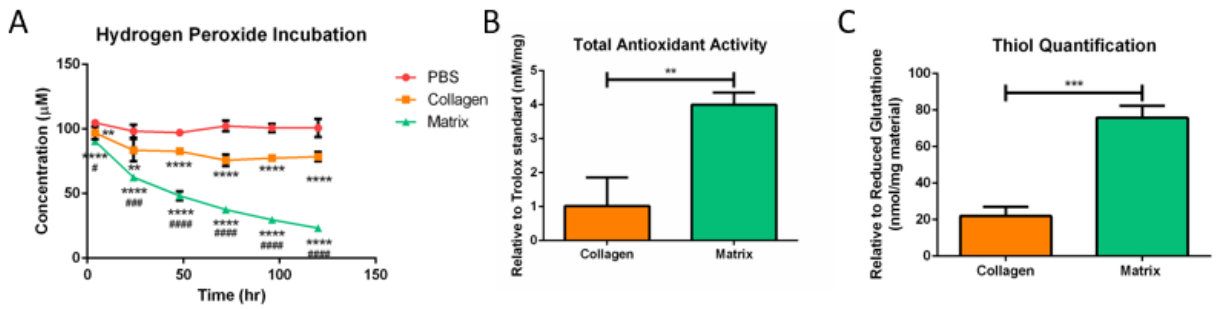

Figure 1.7: Reactive scavenger activity of myocardial matrix material. (A) 150 µL of 166.7 µM hydrogen peroxide diluted in PBS solution was applied to a solution only control (red), and 100 µL collagen (orange) and myocardial matrix (green) hydrogels (n = 5 each). Measurements at 4, 24, 48, 72, 96, and 120 hours of the hydrogen peroxide in the supernatant were measured showing a continuing decrease in concentration for myocardial matrix versus PBS and collagen controls. (B) Total antioxidant activity determined relative a Trolox antioxidant standard for myocardial matrix versus collagen in solution per mg of material (n = 4) (C) Thiol content was determined compared to glutathione standard in myocardial matrix versus collagen per mg of material (n = 4 each) (* is significance to PBS, # is significance to collagen gel, *p< 0.05, **p< 0.01, ***p< 0.001, ****p< 0.0001).

1.2.7. Myocardial Matrix Reduces Effects of Oxidative Stress

To determine whether this ROS scavenging environment lead to changes in cardiomyocyte phenotype, encapsulated neonatal cardiomyocytes after 2-3 days was treated with 2.5mM H_2O_2 in culture media for 4 hours. Change in redox metabolic activity was measured with alamarBlue assay showing a significantly greater change compared to collagen encapsulated gels (Figure 1.8A). mRNA was then isolated from encapsulated cells and expression of cell stress markers that lead to inhibition of cell cycle progression, p19ARF and p16, from oxidative stress were measured compared to GAPDH housekeeping gene. Difference in cycle number values relative to respective control gels in 10% fetal bovine serum supplemented DMEM/F12 media determined a significantly greater expression in collagen culture gels compared to matrix suggesting a reduction in activation of oxidative stress

pathways (Figure 1.8B).

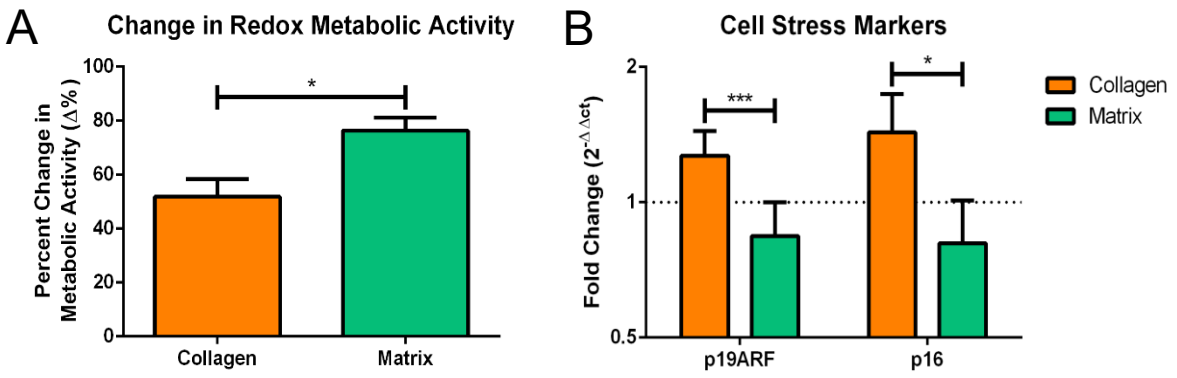

Figure 1.8: Shielding from oxidative stress with encapsulation in myocardial matrix hydrogel. 2.5mM hydrogen peroxide in 500µL of basal DMEM/F12 media was applied to 250,000 encapsulated neonatal cardiomyocytes in 25 µL collagen (orange) hydrogels and myocardial matrix (green) hydrogels for 4 hours. (A) Change in metabolic activity was determined with AlamarBlue assay, which is known to respond to alterations in redox metabolic activity (n = 4 each). (B) Assessment into expression of oxidative cell stress markers that inhibit cell cycle progression, p19ARF and p16, were determined relative to housekeeping gene, GAPDH (n = 4 each). (* is significance to PBS, # is significance to collagen gel, *p< 0.05, **p< 0.01, ***p< 0.001, ****p< 0.0001).

1.3 Discussion

As cardiac injury from myocardial infarction is known to lead to sudden and continuous cardiomyocyte death, various therapies have attempted to renew the loss cardiomyocyte population as a therapeutic strategy. Although various hypotheses on the potential of new cardiomyocytes to form in the adult tissue and source of these cardiomyocytes, the field seems to have settled on the following dominant hypotheses that: 1) the mammalian heart up to shortly post-gestation has significant proliferative capability[77-80], 2) mammalian cardiomyocyte renewal occurs from pre-existing cardiomyocytes similar to common non-mammalian animal models such as zebrafish studied in cardiac repair [77-80], and 3) the adult mammalian heart maintains has a low level of proliferative cardiomyocytes maintained in the adult myocardium [81]. An additional hypothesis that has gained momentum is that cardiomyocyte proliferation is hindered by increases in oxidative stress based on increase oxidative damage of DNA shortly post-

gestation, maintenance of a proliferative phenotype with ROS scavengers or systemic hypoxia and increased incidents of proliferative cardiomyocytes localized to sites of hypoxia in adult tissue [104-106].

Based on these observations, cardiomyocyte response to our material *in vivo* and *in vitro* were investigated for potential to stimulate increased cardiomyocyte renewal and material interactions that might be responsible for these effects. Results suggest that our material stimulates a mild increase cardiomyocyte proliferation when directly interacting with our material *in vitro* compared to collagen controls and evidence that increased cardiomyocyte cell cycle progression is stimulated *in vivo*. Unfortunately, due to results suggesting questionable interpretation of common staining methods for proliferation in rat cardiac tissue based on high basal expression for cardiomyocytes in healthy tissue despite known lack of cardiomyocyte proliferation in healthy tissue, further assessment based on these methods was halted as analysis would lead to false positives. Instead investigation of the material properties has highlighted functionality of decellularized myocardial matrix as a ROS scavenger, which is an underemphasized role in the biomaterials field. Given evidence suggesting that reducing oxidative stress can help maintain proliferative characteristics in cardiomyocytes and our demonstration of cardiomyocyte response encapsulated in our matrix material, these properties demonstrate the favorability of utilizing these decellularized material platforms for reducing effects of oxidative stress and damage in chronic tissue diseases.

1.4 Methods and Materials

1.4.1 Preparation of Myocardial Matrix Material for In vitro and In vivo application

Injectable aliquots of myocardial matrix material were created and assessed for material characteristics based on previously described protocols[107]. In brief, fresh porcine hearts were excised from adult pigs and the left ventricular tissue was isolated. Major vessels and fascia were removed and remaining muscle tissue was cut into less than 5 mm sized pieces. Tissue

will then be decellularized in 1% sodium dodecyl sulfate solution in 1x PBS under agitation for 4-5 days until tissue appeared completely white. An additional day of rinsing in water and repeated water rinsing with manual mixing was performed to remove all observable traces of SDS. Decellularized tissue was lyophilized and material from at least three hearts were combined to minimize batch-to-batch variability before being milled into a fine powder. Milled myocardial matrix was partially digested with a tenth mass of pepsin relative to matrix material in 0.1 M HCl at room temperature for 48 hours. For *in vivo* studies, the standard protocol was followed by neutralization with 1 M NaOH to a pH of 7.4, reconstitution to physiological salt concentration with 10x PBS and dilution to 6 mg/mL with 1x PBS. For *in vitro* studies, this protocol was modified utilizing neutralization with 10 M NaOH to a pH of 7.4 and solely neutralized myocardial matrix was aliquoted based on mass for subsequent experiments. Both preparations of material were frozen in a -80ºC freezer, lyophilized and stored with desiccate for long term storage at -80ºC.

1.4.2. *In vivo* Delivery of Thymidine Analogs Following Myocardial Matrix Hydrogel Delivery Post-myocardial infarction

All experiments in this study were performed in accordance with the guidelines established by the committee on Animal Research at the University of California San Diego, and the American Association for Accreditation of Laboratory Animal Care.

Two groups of Sprague Dawley rats (n = 8 per group) underwent a previously described ischemia-reperfusion procedures[72] accessing the heart by left thoracotomy for 35 minute temporary occlusion of the left coronary artery to induce infarction. After 1 week post-MI, animals were randomized for myocardial matrix or saline injection. Myocardial matrix aliquots that were salt reconstituted were resuspended with sterile water into a homogeneous suspension before injection. The heart was viewed through an excision in the diaphragm to deliver a 75 µL direct intramyocardial injection into the peri-infarct area[72, 73]. Following the

injection procedure, Alzet® osmotic pumps were implanted subcutaneously in the dorsal region as previously described[108] providing continuous delivery of 20 mg/kg/day of 5-Ethynyl-2'deoxyuridine (EdU) for 1.5 weeks. Afterwards, the initial pump was replaced with a second pump containing an alternative thymidine analog bromodeoxyuridine (BrdU) for an additional 1.5 weeks. To account for expected delay of thymidine analog to the heart based subcutaneous delivery, intraperitoneal injections of each respective thymidine analog at a concentration of 20 mg/kg was performed on the day preceding, immediately following, and the day after pump implantation. At day 29 post-infarction, rats were euthanized by 300 µL lethal dose of sodium pentobarbital delivered by intraperitoneal injection, excision of the heart, and fresh freezing the tissue in OCT for sectioning. An additional set of animals focusing on an earlier timespan with a 7 days post-MI EdU delivery was also examined to determine whether a burst increase in thymidine incorporation was observed and for obtaining tissue for staining transient markers indicative of cell cycle progression.

1.4.3. Histology and Immunohistochemistry

Fresh frozen tissue in OCT were cryosectioned to obtain a transverse section of the heart. Cryosections from 12-16 different evenly spaced locations were used for all immunohistochemistry. For infarct size analysis, hematoxylin and eosin staining and quantification of percent infarct area by ratio of infarct area to left ventricular and septal area to assess for outliers that should be excluded from subsequent analysis.

For immunohistochemical staining, slides were fixed with acetone or 4% paraformaldehyde and blocked with a buffered solution containing donkey serum, bovine serum albumin, and triton-X 100 based on the optimized antibody protocol. The following primary antibodies were incubated for 1 hour at room temperature or for 12-18 hours at 4°C for the following markers: PCM-1 (1:100 dilution, Sigma-Aldrich), PCM-1 (1:200, Santa Cruz), α-actinin (1:800, Biorad), PDGFR-α (1:200, Novus Biologicals), vimentin (1:200, Santa Cruz), Isolectin

Griffonia Fluorescein (1:150, Vector Laboratories), smooth muscle cells (1:800, α-SMA), CD68 (Biorad, 1:200), CD45 (Biorad, 1:200), BrdU (1:100, ThermoFisher Scientific), pHH3 (Sigma-Aldrich). The following secondary antibodies were incubated for 30-45 minutes at room temperature: anti-rat Alexa Fluor 568 (1:500 dilution), anti-rabbit Alexa Fluor 488 (1:800 dilution), anti-mouse Alexa Fluor 488 (1:800 dilution), anti-rat Alexa Fluor 488 (1:500 dilution), anti-rabbit Alexa Fluor 568 (1:500 dilution), and anti-rabbit Alexa Fluor 647 (1:500 dilution). Bright field images were taken with Leica Aperio ScanScope® CS^2 and fluorescent images with the Leica Ariol® system (Leica). EdU incorporation was stained by Click-iT™ Plus EdU Cell Proliferation Kit for Imaging, Alexa Fluor™ 647 dye (ThermoFisher Scientific) following secondary antibody staining. Stained tissue was scanned by Leica Ariol® system. Selection of region of interest around the infarct and confirmation of positive colocalization was drawn and visualized, respectively, in Aperio ImageScope software (Leica). Automated expansion around the infarct at 250 μm intervals for designated a borderzone region of interest and automated analysis of costaining was performed by custom MATLAB script (Mathworks, Natick, MA).

1.4.4. Material Characterization

Capability of myocardial matrix material as a ROS scavenger was investigated based on interaction of material with hydrogen peroxide and quantifying components of the matrix material. In brief, 100μL myocardial matrix (6mg/mL) and collagen gel controls (2.5 mg/mL, concentration for similar porosity and mechanical strength to matrix gel) was formed overnight in a microcentrifuge tube. 150 μL of 166μM H_2O_2 peroxide solution diluted in PBS was applied to each gel (100 μM final concentration). A solution only control to assess degradation of the hydrogen peroxide over time was also made. Samples were incubated at 37°C on a shaker plate set to 120 rpm and hydrogen peroxide content was determined by Pierce™ Quantitative Peroxide Assay Kit. Similar procedural set-up was applied to matrix and collagen material in

solution along with pre-milled myocardial matrix scaffold material incubation with hydrogen peroxide.

Total antioxidant activity and thiol content of myocardial matrix material and collagen controls was measured by Cayman Chemical's Antioxidant Assay kit and Cayman Chemical® Thiol Detection Assay Kit, respectively. Results were normalized to mass of material for comparison of antioxidant activity and thiol content.

1.4.5. Neonatal Cardiomyocyte Isolation and Hydrogel Encapsulation

P1 neonatal rat cardiomyocytes were isolated from Spague Dawley rats pups by Neonatal Cardiomyocyte Isolation System (Worthington Enzyme). Following manufacturer instructions collecting cardiac cell suspension from neonatal myocardial rat tissue, the cardiac cell suspension was pre-plated for 2 hours and the cell in solution were collected to enrich for cardiomyocytes. For assessment of cell proliferation, cells were pre-labeled by CellTrace™ Far Red before encapsulation while other cellular experiments proceeded with unlabeled cells. Encapsulation of cells was performed with some modifications for this specific cell type based on a previously describe protocol [109]. In brief, solely neutralized myocardial matrix in lyophilized aliquots were resuspended to a 6mg/mL concentration with cardiomyocyte culture media consisting of 1:1 DMEM/F12 solution (Gibco) supplemented with 10% fetal bovine serum (Gibco) and 1% penicillin streptomycin (Gibco). Cells for encapsulation were pelleted by 50 rcf centrifugation at 4ºC and resuspended with the matrix culture media mixture. 25 µL gels were formed containing 300,000 cells per gel by pipetting the mixture as a collected droplet in the center of each well in a 24 well plate and incubating in a 37ºC incubator for 1 hour. Following the 1 hour incubation, gel formation was confirmed by tilting the well plate vertically and observing maintained gel structure before adding 600 µL to each well for culture. Encapsulated cells were cultured at 37ºC and 5ºC CO_2 with media changed every 2-3 days.

1.4.6. Flow Cytometry Analysis

CellTrace™ prelabeled cells from encapsulations were removed from the well plate surface by a sterile spatula and at least three gels were batch per sample into an enzymatic digestion solution consisting of 1:1 solution of HBSS (calcium and magnesium supplemented) and 1% bovine serum albumin in PBS with and 1 µM HEPES (Gibco), 300 U/mL collagenase type IV (Worthington Biochemical), 60 U/mL hyaluronidase (Sigma-Aldrich) and 10 U/mL DNase I (Sigma-Aldrich). Gel in enzymatic digestion solution were incubated at 37ºC under mechanical agitation at 600 rpm on a thermomixer (Benchmark Scientific) for 20 minutes. Solutions were then kept in ice and FACs buffer consisting of 2% fetal bovine serum and 1mM EDTA in DPBS lacking calcium and magnesium to inactivate enzyme activity. Cells were centrifuged at 50 rcf centrifugation at 4ºC and resuspended in HBSS. Cell suspension was stained with LIVE/DEAD™ Fixable Aqua (ThermoFisher Scientific) for 10 minutes at 4ºC and excess dye was quenched with FACs buffer. Cells were fixed for 10 minutes and permeabilized with BD Cytofix/Cytoperm™ solution, respectively. PCM-1 antibody (1:400, Sigma-Aldrich) and concentration matched rabbit IgG isotype control (Novus Biologicals) were incubated with cells for 12-18 hours at 4ºC in BD Cytoperm™ solution. Secondary staining with donkey anti-rabbit PE (1:1500, Biolegend) was applied for 30 minutes at 4ºC and stained cells were resuspended in FACs buffer before flow analysis on a BD FACSCanto™ II (BD Biosciences). Gating and flow data were processed on FlowJo (FlowJo LLC).

1.4.7. Metabolic and Gene Expression Analysis

Encapsulated cells were assessed for redox metabolic activity by alamarBlue™ (ThermoFisher Scientific) in culture media alone and under oxidative stress from supplemented 2.5 mM H_2O_2 mixed into the culture media for 4 hours. Following 4 hour incubation, gels were removed from the well plate surface by a sterile spatula and at least three gels were batched per sample for RNA isolation. RNA was isolated by RNEasy kit (Qiagen, Germantown, MD)

along with an on-column DNase digestion step (Qiagen) to extract RNA with minimal genomic DNA contamination. Superscript III Reverse Transcriptase kit (Applied Biosystems, Foster City, MA) was used to synthesize cDNA. Then, SYBR Green PCR Master Mix (Applied Biosystems) was used with forward and reverse primers at a final concentration of 200 nM. Gene expression of cell cycle regulators p19ARF and p16 that are upregulated in response to oxidative stress leading to cell cycle arrest and apoptosis were assessed. Primers sequences were as follows: rat p19ARF (F: 5'- GGTTTTCTTGGTGCAGTTCCTG-3', R: 5'-GATCCTCTCTGGCCTCAACAC-3'), rat p16 (5'- GATCCAGGTCATGATGATGGG-3', R: 5'-: ATCAATCTCCAGTGGCAGCG-3') and GAPDH (F: 5'-CATCAAGAAGGTGGTGAAGC-3', R: 5'-GTTGTCATACCAGGAAATGAGC-3'). Samples were run in technical duplicates along with negative controls without template cDNA to confirm lack of contamination in PCR reagents. PCR reactions were run on a CFX95™ Real-Time System (Biorad, Hercules, CA) with the following thermal cycler settings: 30s at 50°C, 2 min at 95°C, 40 cycles of 10s at 95°C, and 30 secs at 63°C based on pre-determined optimal primer efficiency amplification temperature. After completing 40 cycles of PCR amplification, automated melting curve analysis, consisting of increasing the thermal cycler temperature from 50°C to 95°C at 5°C increments lasting 5s each, was used to confirm formation of a singular PCR amplicon for each primer set. Bio-Rad CFX Manager™ 3.0 (Biorad) was used for determining cycle threshold (ct) values from recorded SYBR green signal. Fold change was then determined by $2^{-(\text{Gene 1} - \text{GAPDH})}$ and normalized to fold change of respective gel material without H_2O_2 doped into the media.

1.4.8. Statistical Analysis

All data and plots are presented as mean ± SD. Significance was determined with a one-way ANOVA using a Tukey post-hoc test and an unpaired student's *t*-test based on number of sample groups with a $p<0.05$.

1.5 Acknowledgements

Chapter 1, in part is currently being prepared for submission for publication of the material. “Matrix material supporting a proliferative microenvironment for cardiomyocytes.” Raymond M. Wang, Sylvia Evans, Karen L. Christman. The dissertation author was a primary author of this paper.

CHAPTER 2: Immune System Humanized Mouse Model for the Assessment of Macrophage and T cell populations to Xenogeneic and Allogenic Derived Biomaterials

2.1 Introduction

Determination of a safe immunological response is critical for the application and continued study of therapeutics in human patients, which can provide critical data for successfully bringing novel therapeutics to clinical applications. The field of decellularized extracellular matrix (ECM) based biomaterials is rapidly growing and has developed therapies for numerous applications including wound healing, hernia repair, skeletal muscle defect repair, and myocardial infarction[110-113]. Decellularized ECM biomaterials are an attractive platform for biomaterial therapies since tissue derived ECM can promote tissue remodeling by influencing cellular metabolism, proliferation, migration, maturation, and differentiation[114]. In fact, these biomaterials, derived from xenogeneic and allogeneic tissue sources[115, 116], have been successfully implanted into millions of patients[117]. Xenogeneic materials, from porcine tissue for example, are readily available and can be produced from younger tissue sources, which is desirable for regenerative medicine therapies[118]. However, xenogeneic materials can have potential immunogenic issues, regulatory hurdles and xenogeneic disease transfer. Allogeneic materials avoid some concerns associated with xenogeneic materials, but are typically from older and more limited cadaveric sources, and can have larger batch variability.

While xenogeneic and allogeneic sources for decellularized ECM have been widely used to date, preclinical understanding of these scaffolds is mostly based off immune responses to these matrices in rodents and a few large animals[110, 119, 120]. Given difficulties with obtaining sequential patient biopsies, no one has thoroughly monitored or understood the human immune response to these materials. Although connected evolutionarily, rodents typically used for biocompatibility testing provide limited representation of the human immune response. Differences in immune cell receptors, cytokine expression and response to various stimuli highlight how responses in rodents might not correlate with outcomes in humans[121]. Even non-

human hominids have various biomedical differences from humans[122]. This combined with our incomplete understanding of the human immune system has led to the removal of several well characterized materials from the market[123, 124].

One method to address these shortcomings is the use of a humanized mouse (Hu-mice) model for preclinical assessment of the human immune response. Over the last 20 years, significant improvements have transformed Hu-mice into a valuable model for mimicking the human immune response[125-127]. In particular, Hu-mice developed by implantation of human fetal thymus tissue and injection of human $CD34^+$ fetal liver cells into immune compromised NSG mice have been shown to be robust and contain human T-cells, B-cells, and dendritic cells, allowing the ability to reject xenogeneic tissue[128]. This model has been used extensively for studying autoimmune disease, virus infections, xenogeneic transplantation, and more recently allogeneic stem cell transplantation[129]. However, it has yet to be exploited in the biomaterials field. In this study, we utilized this Hu- mouse model to assess the human immune response to decellularized ECM biomaterials, specifically injectable hydrogels derived from porcine or human myocardium, which were initially developed to treat the heart post-myocardial infarction[120, 130-132]. Our goal with this study was to evaluate the utility of the Hu-mice for evaluating biocompatibility and studying the human immune response to biomaterials prior to clinical translation. We hypothesized that this model would demonstrate different immune responses to human versus xenogeneic ECM, unlike a wild type rodent model.

2.2 Results

2.2.1 Cellular Infiltration into Biomaterial Core of Xenogeneic Versus Allogeneic ECM

Samples were sectioned and stained with hematoxylin and eosin (H&E) for histological analysis (Figure 2.1A). Based on cellular infiltration being observed to be unevenly distributed in the injected material, particularly towards the center in the Hu-mice samples (Figure 2.1A),

both overall cellular content versus cells that infiltrated 200 μm from the material border were analyzed[133].

Comparing differences in cell density throughput the whole biomaterial for PMM and HMM, significantly higher infiltration was observed in PMM in both Balb/c (Figure 2.1B) and Hu-mice (Figure 2.1C) at day 3, but no differences were observed between materials in either animal model at one week (Figure 2.1B, C). This same trend was observed when analyzing only the biomaterial core in Balb/c mice (Figure 2.1D); however, in Hu-mice, there was a slight greater infiltration of cells at the earlier day 3 timepoint with a significantly decreased infiltration into the HMM core compared to the PMM core at one week (Figure 2.1E). This decreased infiltration notably occurred in HMM, which is an allogeneic material for the Hu-mice. In contrast, PMM and HMM both represent xenogeneic ECM in the Balb/c mice where similar degrees of cellular infiltration at the later day 7 timepoint were observed.

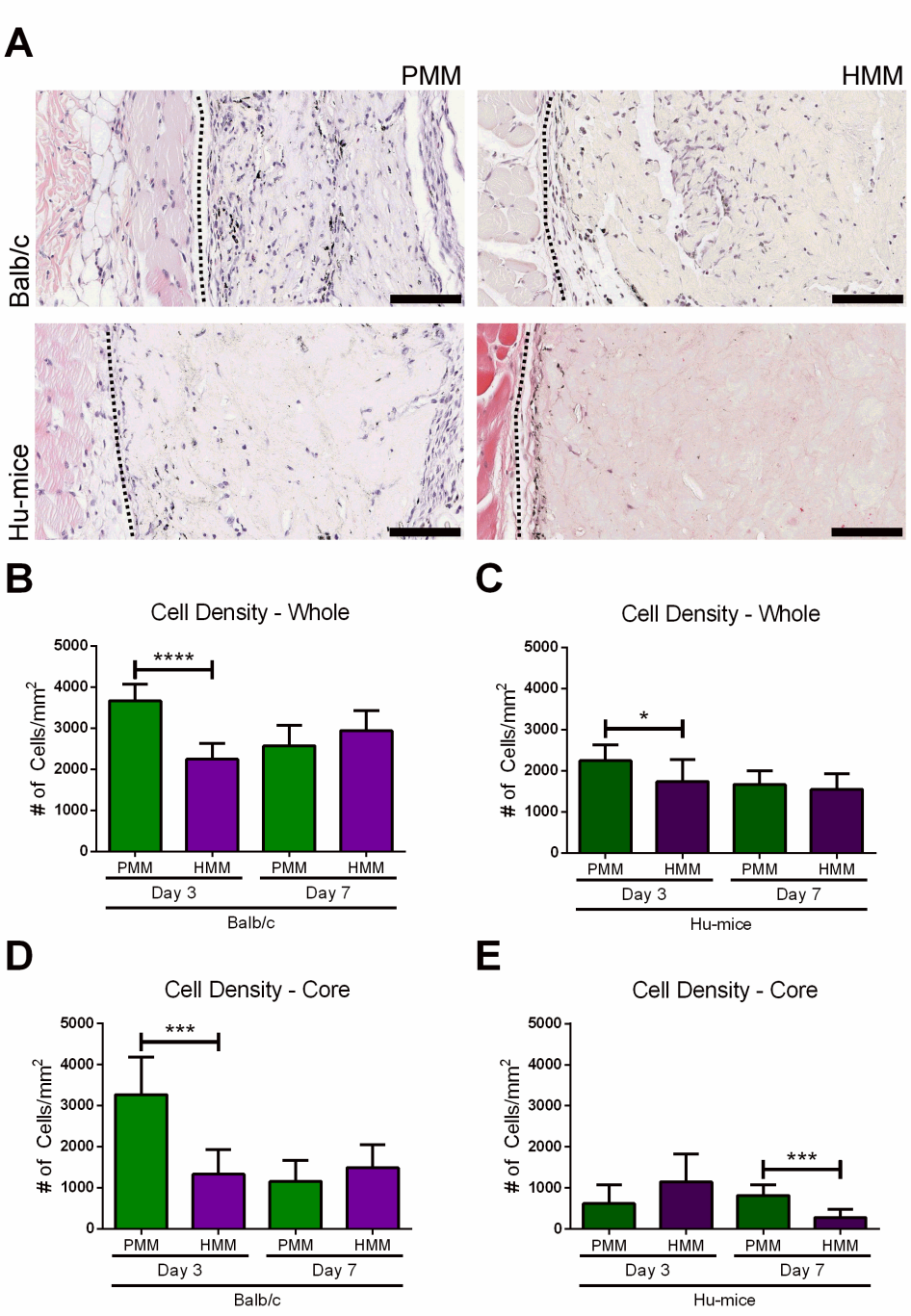

Figure 2.1: Total cell infiltration. (A) Hematoxylin and eosin (H&E) images represent local tissue immune response one week after subcutaneous injections of porcine myocardial matrix (PMM) or human myocardial matrix (HMM) in Balb/c and a humanized mouse model (Hu-mice). Quantification of cellular density for the whole biomaterial (B, C) and infiltration into the core (D, E) of the biomaterial for each group is also shown (*$p<0.05$, ***$p<0.001$, ****$p<0.001$). On the left of each image is the panniculus carnosus muscle layer of the dermal tissue and on the right is the injected biomaterial. The biomaterial and dermal tissue are separated by a black dotted line. Scale bars are 100 μm.

2.2.2 Minimal Human Cellular Infiltration for Allogeneic ECM

After investigation by histological analysis of the total cell density, we then investigated differences in human specific cell infiltration with a human nuclei marker. Similar results and low numbers of infiltrating cells were observed at day 3, but a notable difference in the prevalence and location of cells stained for human nuclei between PMM and HMM was observed at one week in the Hu-mice (Figure 2.2A). Both analyses based on percentage relative to total nuclei content and cellular density of human cells trended higher in PMM compared to the HMM for the overall material, with a significant difference in cell density based on assessment in the material core regions (Figure 2.2B-E). This demonstrated that human cells distinguished between the allogeneic versus xenogeneic biomaterial and suggested that these were immune cells recruited during later time spans during the immune response.

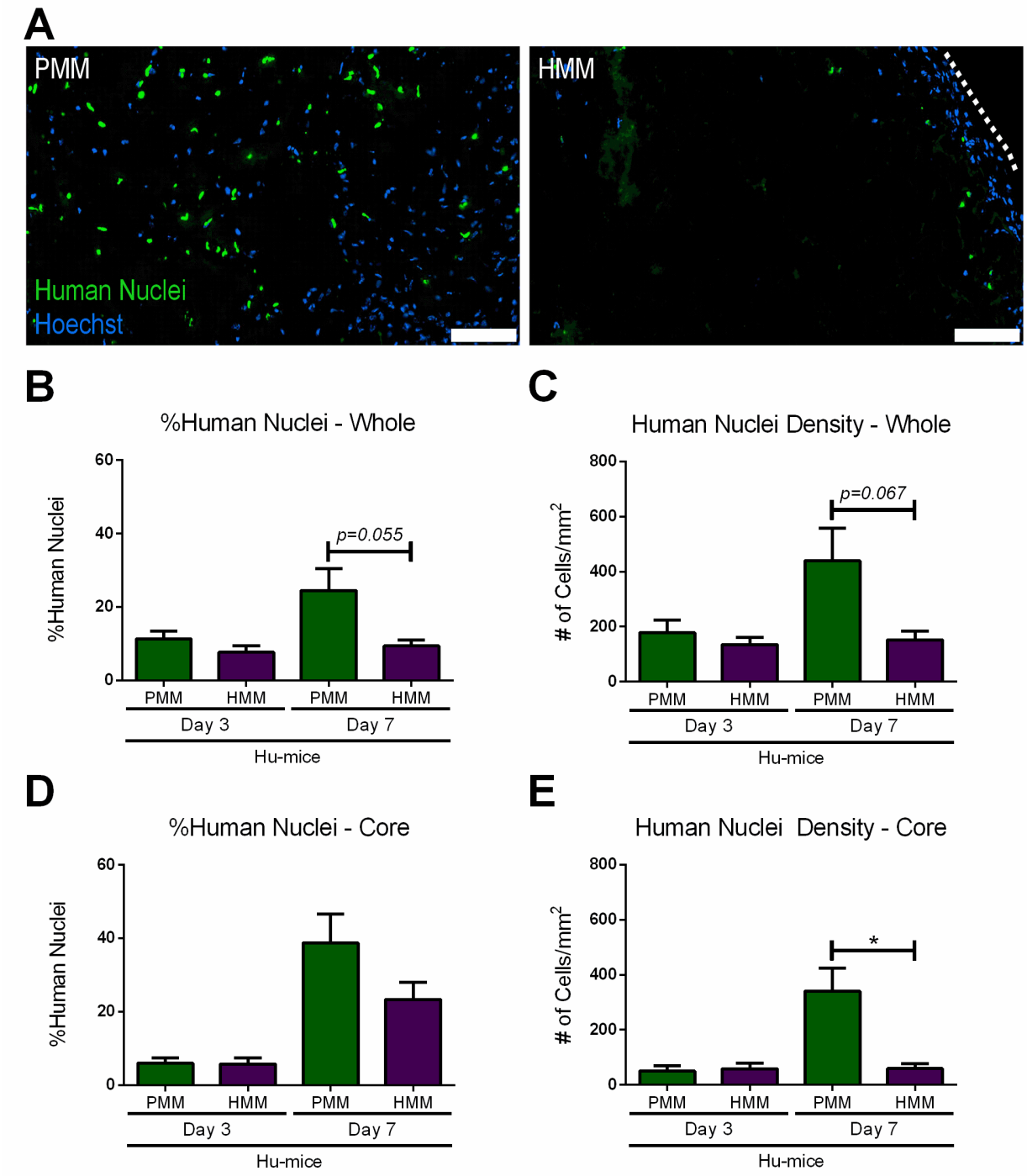

Figure 2.2: Human nuclei infiltration. (A) Representative images of Hoechst stained nuclei (blue) and human nuclei staining (green) of humanized mice (Hu-mice) injected with either porcine myocardial matrix (PMM) or human myocardial matrix (HMM) at one week. The dotted white line indicates edge of HMM biomaterial. Quantification of percent and density of human nuclei in the whole biomaterial (B, C) and into the core (D, E) of the biomaterial (*p<0.05). Scale bars are 100 μm.

2.2.3 Greater T-helper Cell Infiltration in Xenogeneic ECM Compared to Allogeneic ECM

Since the Hu-mouse model showed significant differences in the number of cells infiltrating between the allogeneic and xenogeneic materials, we then investigated differences in specific types of recruited immune cells. T-cells have been shown to be important for eliciting the pro-remodeling transition from early pro-inflammatory immune responses to ECM biomaterials supporting tissue repair[134]. Immunohistochemistry was used to visualize cell infiltration and quantify spatial distribution of T-helper cells and cytotoxic T-cells in the PMM and HMM materials in the Balb/c and Hu-mice (Figure 2.3A). Nondecellularized porcine myocardial matrix (NDM) was also compared as a pro-inflammatory control in both mouse models.

Comparing the ratio of T-helper to cytotoxic T-cells, no significant differences were found among all materials at day 3 both in the whole and core biomaterial in both mouse models (Figure 2.3B, C). T-helper infiltration was generally low at this timepoint (Figure 2.4A, B) and NDM consistently recruited significantly greater cytotoxic T-cell densities compared to the decellularized materials for both Balb/c and Hu-mice (Figure 2.4C, D). By day 7, minimal numbers of cytotoxic T-cells were found in PMM and HMM groups, while cytotoxic T-cell infiltration continued to increase in NDM in both animal models (Figure 2.4C, D). For all materials in both animal models, T-helper cell densities increased by day 7 with the decellularized materials becoming T-helper cell dominant compared to NDM (Figure 2.3B, C). This transition for the decellularized materials from a cytotoxic to a T-helper cell response has been previously observed[135] and suggests only NDM was being rejected as expected. Comparing the T-helper versus cytotoxic T-cell response between the decellularized materials, no significant differences were observed in the Balb/c mice and in the Hu-mice when the whole biomaterial was examined (Figure 2.3B). However, for the core analysis in the Hu-mice, PMM was significantly human T-helper cell dominant compared to both HMM and NDM (Figure 2.3C) with a significantly higher T-helper cell density than HMM (Figure 2.4B). This corresponded with

previous human nuclei data (Figure 2.2E) indicating that PMM elicited greater human cell infiltration at one week. Collectively, these results showing minimal cytotoxic T-cell density and greater T-helper density in PMM in the Hu-mouse model suggested that the xenogeneic PMM material stimulated a greater pro-remodeling response compared to the allogeneic HMM material.

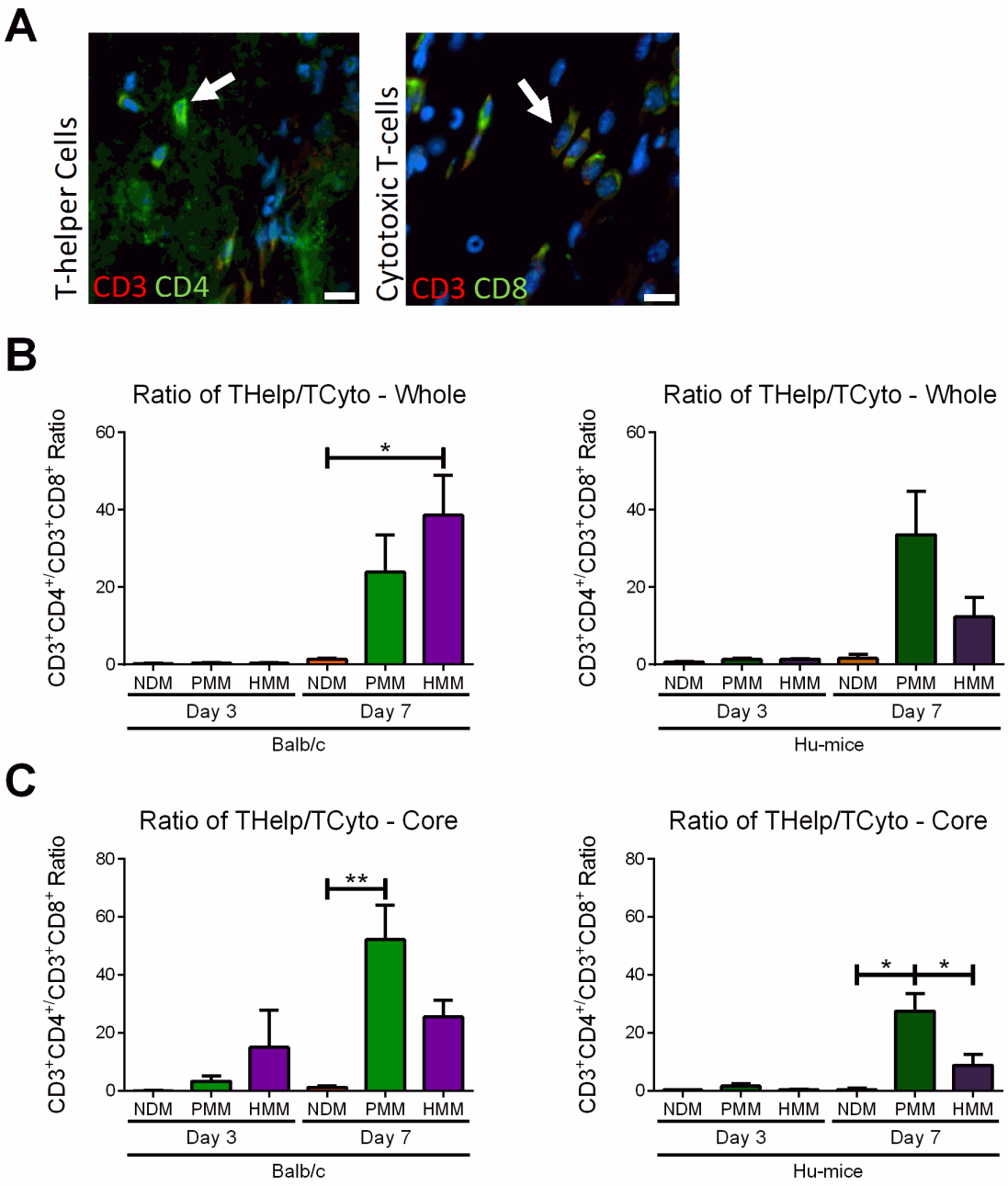

Figure 2.3: T-helper cell and cytotoxic T-cell infiltration. (A) Representative images of T-helper cells and cytotoxic T-cells with arrows indicating positive staining. Hoechst staining was used to label cellular nuclei (blue). T-helper cells were labeled by co-staining with CD3 (red) and CD4 (green). Cytotoxic T-cells were labeled by co-staining with CD3 (red) and CD8 (green). Ratios of cell density quantification of T-helper cells versus cytotoxic T-cells in whole biomaterial (B) and biomaterial core (C) in nondecellularized (NDM), porcine (PMM) and human myocardial matrix (HMM) at day 3 and 7 in Balb/c or Hu-mice. (*p<0.05, **p<0.01). Scale bars are shown at 10 μm.

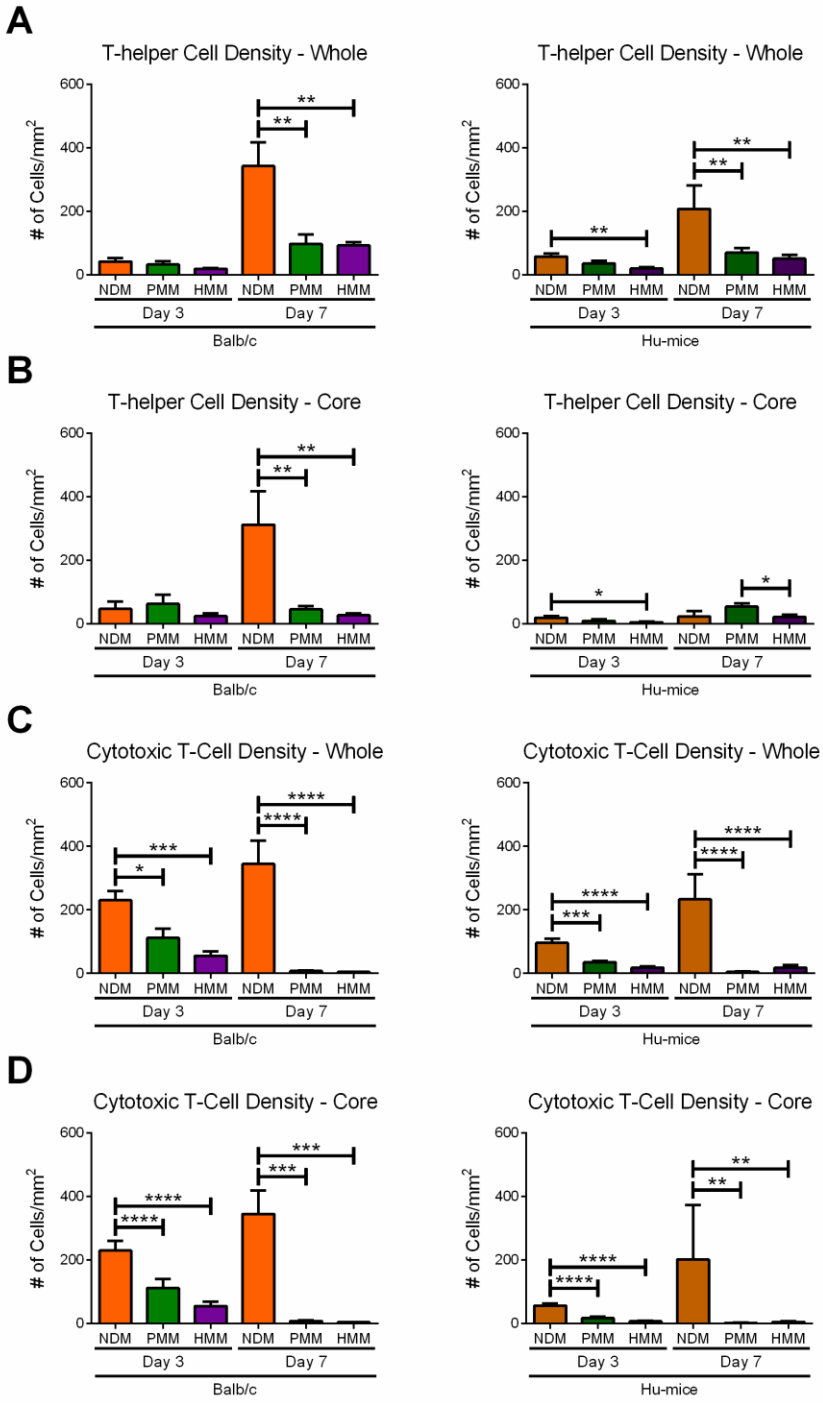

Figure 2.4: Quantified cell density for T-Helper cells and Cytotoxic T-cells. Cell density quantification of T-helper cells in whole biomaterial (A) and biomaterial core (B) in nondecellularized (NDM), porcine (PMM) and human myocardial matrix (HMM) at three days and one week in Balb/c and Hu-mice. Cytotoxic T-cell density in whole biomaterial (C) and biomaterial core (D) at three days and one week in Balb/c and Hu-mice. (*p<0.05, **p<0.01, ***p<0.001, ****p<0.0001).

2.2.4 Similar Macrophage Infiltration and Polarization between Xenogeneic and Allogeneic ECM

Macrophage presence was also analyzed since macrophage phenotypic expression has been shown to be an important indicator of tissue remodeling outcomes for ECM based biomaterials[136, 137]. Although the presence of human macrophages has been previously demonstrated in this mouse model, Hu-mice mice derive from a immunodeficient mouse model that still maintains mouse macrophage populations that were highly abundant compared to minimal to no human macrophage infiltration observed into the biomaterial. Since the response was dictated by mouse macrophages, we evaluated the infiltration and polarization of these cells in both mouse models to determine if interaction with the human T cells lead to a unique immune response. Macrophage polarization is plastic and complex[138-140], but is often simplified into pro-inflammatory M1 and pro-remodeling M2 phenotypes[141]. Macrophages were identified with pan-macrophage marker F4/80, and polarization was evaluated with common markers for M2 (CD206) and M1 (iNOS) for pro-remodeling versus pro-inflammatory macrophages, respectively (Figure 2.5A)[59, 142]. In both mouse models at day 3, the ratio of M2/M1 macrophages for all three materials was below 1 in both whole and core biomaterial, suggesting that the short-term macrophage response was M1 dominant (Figure 2.5B, C). However, the total macrophage (Figure 2.6A) and M1 macrophage cell density (Figure 2.6C) was significantly greater in NDM compared to the decellularized materials in both animal models. At one week, NDM remained M1 dominant, while in the Balb/c and Hu-mice the decellularized materials switched to a M2 dominant response based on both whole and core biomaterial analysis (Figure 2.5B, C). Assessment of cell densities indicated that M2 macrophage cell density increased in all materials for both mouse models from day 3 to one week (Figure 2.6E, F). However, density of M1 macrophages remained greater or increased by one week in NDM while M1 density generally decreased in the decellularized materials in both mouse models (Figure 2.6C, D). This demonstrated a transition from a pro-inflammatory to pro-remodeling macrophage

polarization for the decellularized materials, which is characteristic of wound healing[143]. This was also notably similar to the transition observed from our T-cell analysis (Figure 2.3B, C). Although, no distinct differences were observed in the response between PMM and HMM for the two animal models, these results showed that macrophages were dynamically responsive in the Hu-mouse model similar to a wild-type model. Interestingly, dual stained macrophages with both M1 and M2 markers were commonly observed, especially at the biomaterial border for all material groups (Figure 2.6G, H). This observation is not unique since previous studies have observed these results *in vivo,* and some studies have suggested that dual polarized macrophages are involved in angiogenesis[59]. As a result, these cells were separately grouped and not considered specifically M1 and M2 polarized in the ratio analysis.

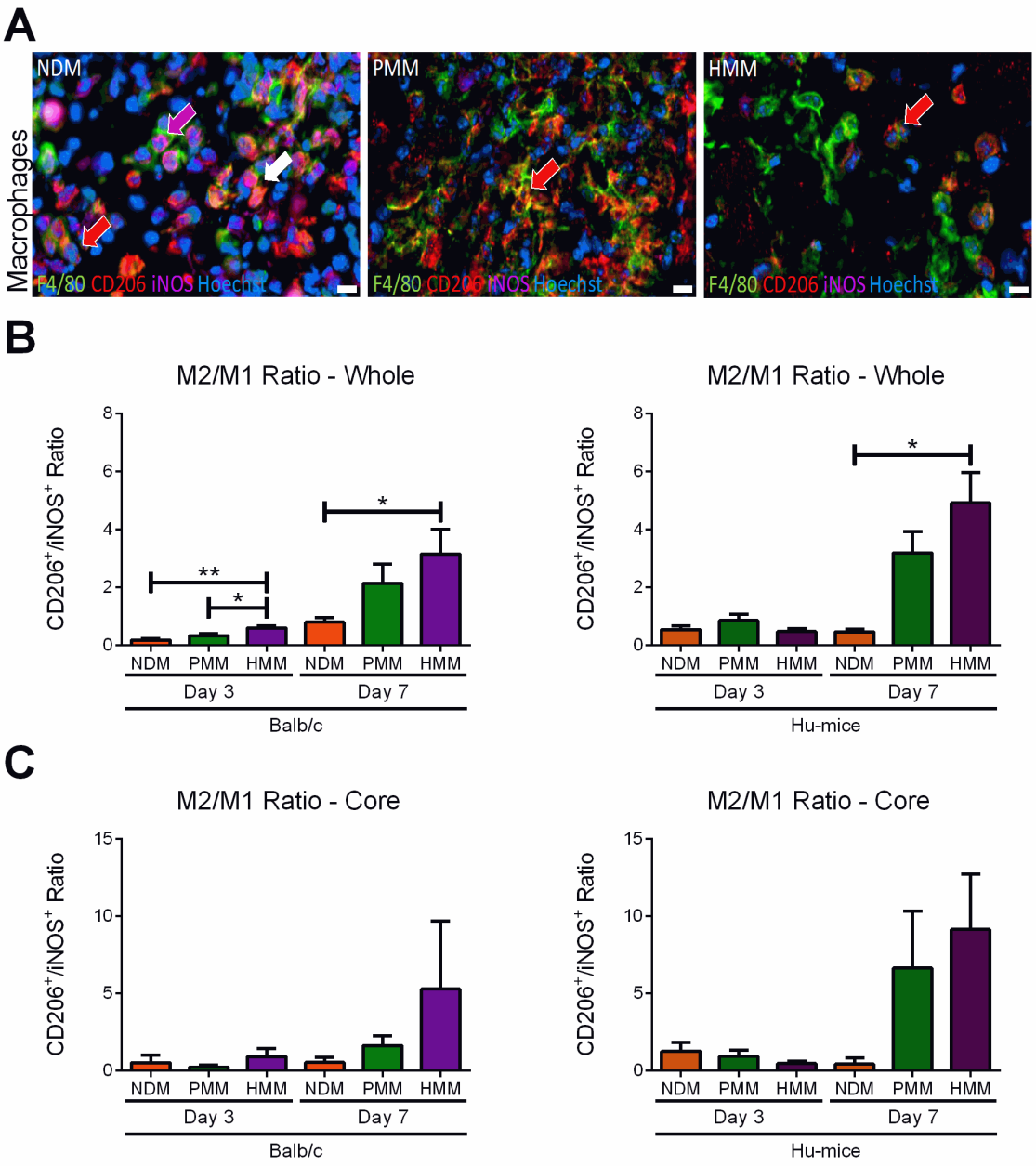

Figure 2.5: Polarized macrophage infiltration. (A) Representative images at one week of polarized macrophage staining with a red arrow indicating a M2 macrophage, a magenta arrow indicating a M1 macrophage and white arrow indicating a macrophage stained with both M2 and M1 markers. Hoechst staining was used to label cellular nuclei (blue). Macrophages were labeled by co-staining with pan-macrophage marker F4/80 (green), M1 marker iNOS (magenta) and M2 marker CD206 (red). Ratios of cell density quantification of $CD206^+$ to $iNOS^+$ macrophages in whole biomaterial (B) and biomaterial core (C) in nondecellularized (NDM), porcine (PMM) and human myocardial matrix (HMM) at day 3 and 7 in Balb/c or Hu-mice. (*p<0.05, **p<0.01). Scale bars are shown at 10 μm.

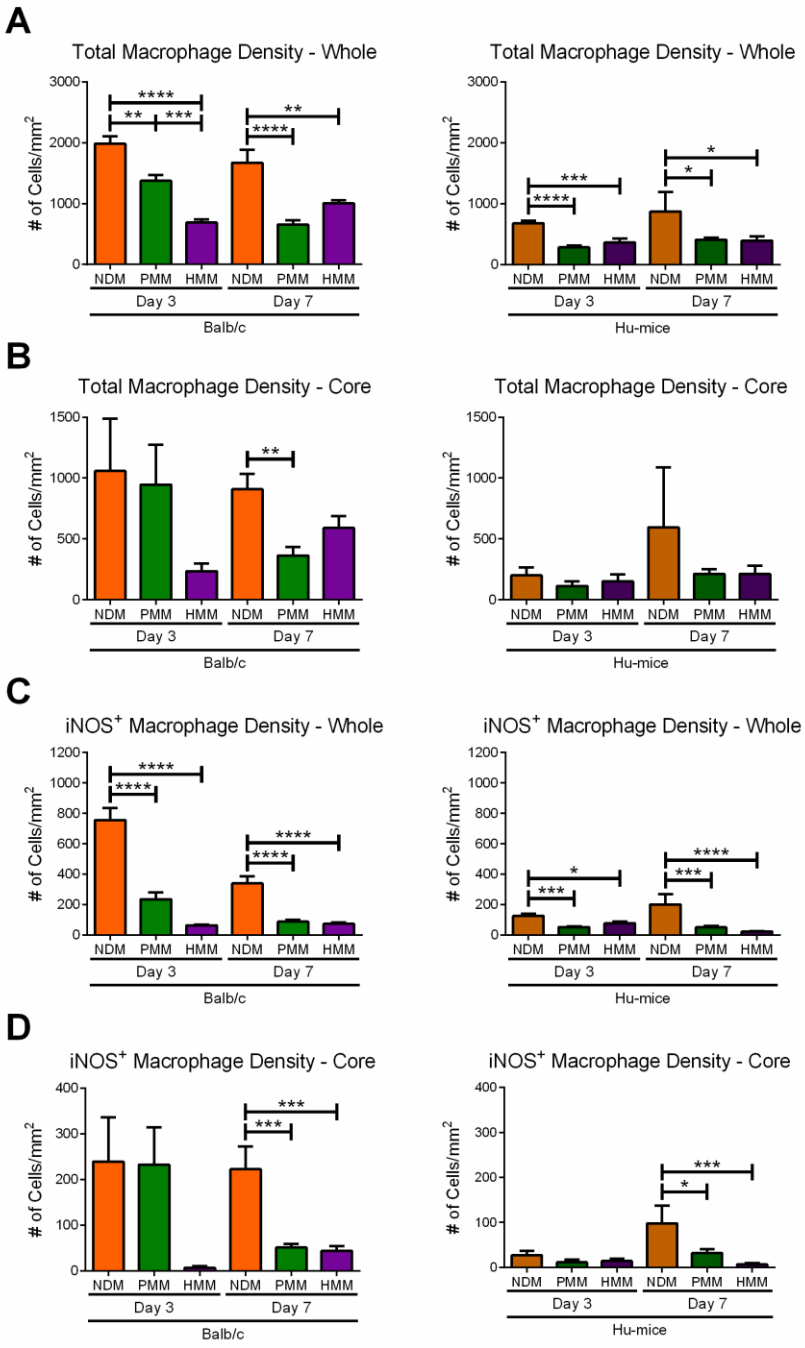

Figure 2.6: Quantified cell density for total macrophages and polarized macrophage phenotypes. (A) and biomaterial core (B) in nondecellularized (NDM), porcine (PMM) and human myocardial matrix (HMM) at three days and one week in Balb/c or Hu-mice. Cell density quantification of iNOS$^+$ macrophages in whole biomaterial (C) and biomaterial core (D). Cell density quantification of CD206$^+$ macrophages in whole biomaterial (E) and biomaterial core (F). Cell density quantification of dual stained iNOS$^+$CD206$^+$ macrophages in whole biomaterial (G) and biomaterial core (H). (*p<0.05, **p<0.01, ***p<0.001, ****p<0.0001).

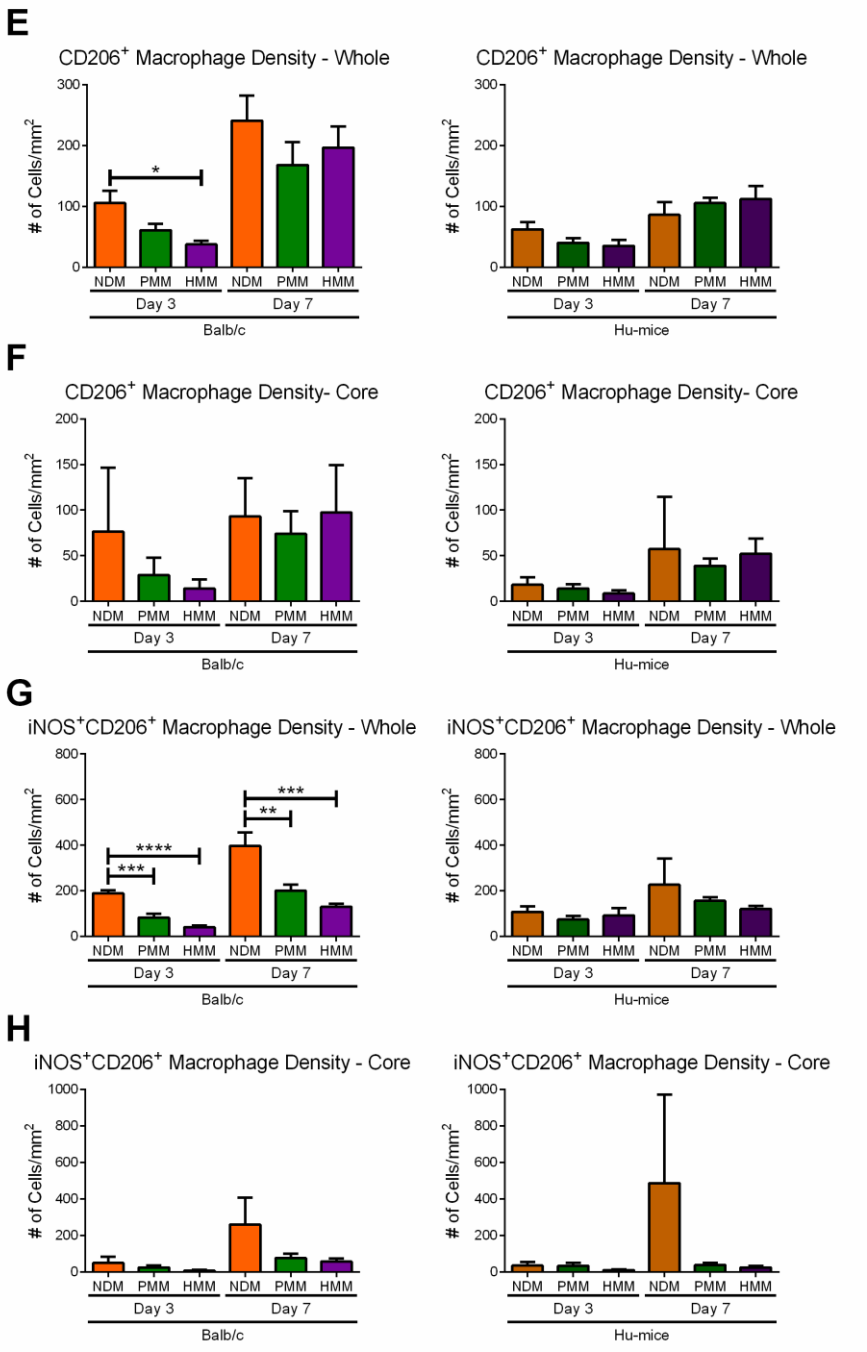

Figure 2.6: Quantified cell density for total macrophages and polarized macrophage phenotypes. (Continued)

2.2.5 Pro-Remodeling Immune Cell Polarization in ECM Biomaterials

Although we determined a T-helper dominant response to our decellularized materials as described above, T-helper cells are known to polarize and show dramatically different phenotypes depending on their local niche[144, 145]. For example, a T-helper cell's dominant response is usually correlated with a pro-remodeling response, but T-helper cell infiltration can be connected with graft rejection as well [146]. Thus, we wanted to more fully characterize the T-helper cell polarization. T-helper cells can be divided into pro-inflammatory Th1 and pro-remodeling Th2 phenotypes[145, 147]. Polarization towards the Th2 phenotype was measured by comparing the ratio of expression of cell-specific master transcription factors GATA3 (Th2) to TBX21 (Th1) for NDM, PMM and HMM in both mouse models[147, 148]. An additional set of human specific T-helper cell markers for receptors CRTH2 (Th2) and CCR5 (Th1) was utilized to further confirm the results in Hu-mice[149-151]. At day 3, polarization was similar for all materials in both animal models (Figure 2.7A, B). This result likely corresponded with the previously determined low T-helper cell presence (Figure 2.4A) at this early time point. By one week, PMM was Th2 trending in Balb/c mice and significantly Th2 polarized in Hu-mice relative to NDM with both sets of T-helper cell markers. In contrast, HMM was only trending towards a Th2 polarization compared to NDM with these markers in the two mouse models (Figure 2.7A, B).

A ratio of related genes expressed in M1 (NOS2) and M2 (ARG1) was also used to measure macrophages polarization with qRT-PCR[142]. At day 3, HMM was significantly M2 polarized compared to NDM in both mouse models. PMM was significantly M2 polarized in Balb/c mice and M2 trending in Hu-mice (Figure 2.7C). Based on the cell staining, these results likely occurred from a greater M1 response in NDM compared to the decellularized materials considering the low M2 macrophage numbers previously shown at this timepoint (Figure 2.5, Figure 2.6). By one week, only PMM was significant in Balb/c mice and upward trending in the Hu-mice compared to NDM (Figure 2.7C). Therefore, notably only PMM elicited a significant

Th2 polarization in the Hu-mice and a significant M2 polarization in the Balb/c mice compared to NDM while HMM was not significant compared to either PMM or NDM at one week.

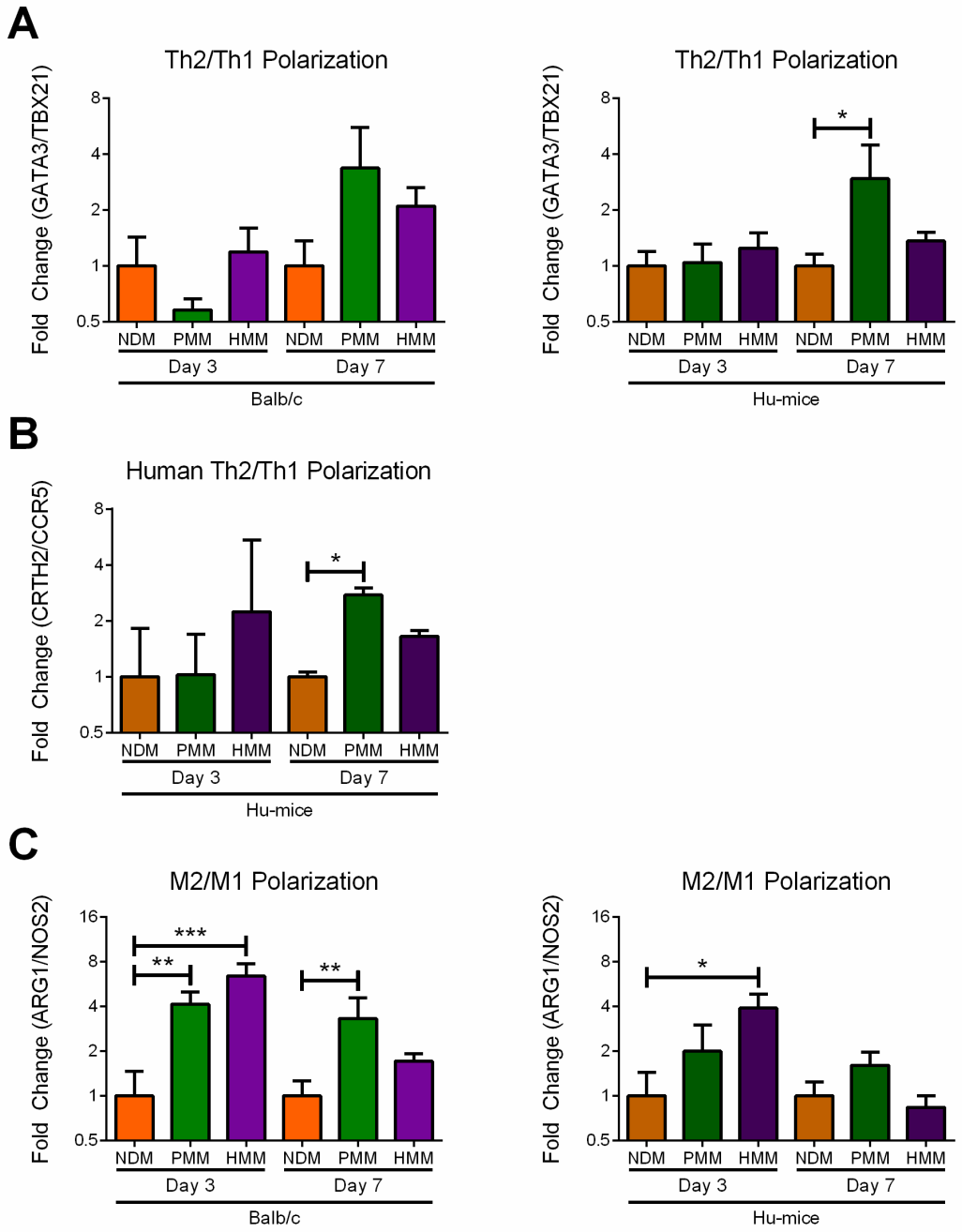

Figure 2.7: Gene expression ratios of T-helper cell and macrophage polarization. qRT-PCR was utilized to determine the degree of polarization of macrophages and T-helper cells at day 3 and one week in Balb/c and Hu-mice. (A) T-helper cell polarization of Th2/Th1 was measured as fold change ratio of GATA3/TBX21 gene expression. (B) A separate human T-helper cell polarization was measured as fold change ratio of CRTH2/CCR5 gene expression. (C) Macrophage polarization of M2/M1 was measured as a fold change ratio of ARG1/NOS2 gene expression. (*p<0.05, **p<0.01, ***p<0.001).

2.3 Discussion

In this study, we investigated the ability of a humanized mouse (Hu-mice) model, which had previously been shown capable of rejecting xenogeneic tissue via a human T-cell mediated immune response[128], to differentiate between allogeneic and xenogeneic decellularized ECM. We tested a xenogeneic biomaterial sourced from porcine myocardial matrix (PMM), which was developed as a therapy for treating hearts post-myocardial infarction[130]. Similarly, a material derived from human cadaveric donor hearts (HMM) was produced as an allogeneic alternative[132]. The Hu-mouse model showed significant differences in the immune response to the allogeneic and xenogeneic materials that differentiated from a wild type animal model, suggesting that the Hu-mouse model could be an advantageous tool in studying the biocompatibility of tissue-derived materials and *in vivo* human immune cell responses.

Investigation of the infiltrating cells showed significant differences in cell densities found in the core of xenogeneic PMM compared to allogeneic HMM material in the Hu-mice. Greater human cell infiltration was observed at one week during the mid-phase immune response, while human cell interaction was similar at the earlier time point. Further evaluation of the infiltrating cells determined that the early day 3 response consisted mainly of M1 ($iNOS^+$) macrophages and cytotoxic T-cells ($CD3^+$, $CD8^+$). These numbers decreased by one week with very few cytotoxic T-cells, and instead predominantly M2 macrophages ($CD206^+$) and T-helper cells ($CD3^+$, $CD4^+$) were present. In contrast, the nondecellularized myocardial matrix (NDM) predominantly contained infiltration of M1 macrophages and cytotoxic T-cells throughout the study. This dynamic shift for the decellularized materials mimics the native wound healing response[143], suggesting that these materials could stimulate similar mechanisms when inducing tissue repair[120, 131]. Infiltration of T-helper cells was particularly distinct in PMM compared to HMM, which has a critical role in supporting a pro-regenerative response to biomaterial therapies[134]. This significantly different response was only observed in the Hu-mouse model

potentially because both PMM and HMM are xenogeneic in the Balb/c, leading to similar levels of T-helper cells and macrophage infiltration.

Gene expression of cell specific markers were utilized to further characterization cell phenotypes towards pro-inflammatory and pro-remodeling subtypes. T-helper subtypes were assessed by cell-specific gene expression ratios towards pro-inflammatory Th1 or pro-remodeling Th2 phenotypes, respectively. This expression is directly correlated with separate phenotypes involving the production of IL-2 and interferon-γ (IFNγ) for Th1 and IL-4, IL-5, and IL-10 for Th2[43]. Similarly, polarized macrophages were assessed towards the pro-remodeling M2 or pro-inflammatory M1 phenotype[142, 152]. M1 macrophages are known to produce inflammatory cytokines of TNF, IL-6, and IL-1β with high levels of IL-12 and IL-23, and low levels of IL-10. Whereas, the M2 polarized macrophages have low levels of IL-12 and IL-23 with high levels of IL-10[141]. Early T-cell and macrophage response to the decellularized materials was Th1 and M2 polarized, respectively, which corresponded with low T-helper cell and lesser M1 macrophage densities from the cell staining analysis. At one week, only PMM was significantly shifted towards the Th2 phenotype and trending towards a M2 polarization compared to NDM in the Hu-mouse model. In contrast, both PMM and HMM were Th2 and M2 polarized in the Balb/c mouse at one week. However, analysis of macrophage cell densities for HMM in the Hu-mice supported that they were similarly more polarized towards a pro-remodeling state. This difference in the magnitude of M2 macrophage polarization measured by qRT-PCR could be due to the lesser presence of T-helper cells in HMM supporting the M2 macrophage phenotype[134].

Potentially, these results could suggest that allogeneic materials elicit lesser human T-helper involvement in the immune response, which reduces immunological concerns, but can also its limit pro-regenerative capability. However, it should be considered that limitations of the allogeneic tissue source might be responsible for these results. The efficacy of tissue decellularization, tissue source age, and cross-linking are crucial parameters that can

significantly impact the host response[153]. For fabrication of the HMM material, older human cadaver hearts were utilized that required additional processing steps such as lipid removal and DNase/RNase treatment[132]. Older ECM is known to shift in composition[113], stimulate a lesser pro-remodeling macrophage response[154], and undergo increased cross-linking and fibrosis[155], which could create less ideal material properties for stimulating tissue repair. Likewise, additional processing steps were required to remove greater adipose tissue commonly found on older human myocardium and reduce nucleotide content to similar acceptable standards for therapeutic applications as the PMM material[132]. These steps could unintentionally strip important biological factors from the material. Previous assessment found that HMM did maintain a complex ECM protein composition with many similar material properties to PMM, though there was notably less sulfated glycosaminoglycan content[132, 156]. As the immune response is mediated by a multitude of cytokine signaling pathways, decreased sGAG content could reduce retention of endogenous chemoattract ant factors and limit the anti-inflammatory response elicited by HMM[157]. Although it could be hypothesized that young human hearts could provide an improved allogeneic scaffold, this is not a viable strategy considering the immediate need for young healthy human hearts for surgical transplantation, prevalence of cardiac diseases[158], and general shortages of healthy human organs[159]. Therefore, these shortcomings could be considered inherent restrictions of cardiac tissue derived allogeneic materials.

These results also demonstrate the insufficiency of immunocompromised NSG mice in modeling the response to biomaterials. There was significantly less cellular infiltration in NSG animals compared to immunocompetent Balb/c animals. Macrophages are present in both animal models, but T-cells are not present in the NSG mice. Therefore, macrophages alone are not sufficient to produce a full immune response to these materials. This is not surprising since the more severe xenogeneic tissue rejection has been shown to be largely a T-cell mediated response and involves the subsequent activation of macrophages[127, 128]. Thus, this raises

concerns utilizing immune compromised animals in studies when a naturally derived material is used.

Although these results demonstrate the potential utility of this model, important limitations should be considered for further studies. One limitation of the Hu-mouse model that should be considered is the inability to measure the role of certain xenogeneic specific epitopes, including the anti-Gal epitope, which is involved in xenogeneic tissue rejection in humans[128]. For processed xenogeneic acellular materials, which have dramatically lower levels of the alpha-Gal epitopes similar to the materials used in this study, this has not been shown or been proven to cause adverse reactions in human patients[153]. Concerns regarding the potential influence of these epitopes could be addressed by evaluating epitope presence in the material, as done in this study, or perform additional tests in knockout mice of these epitopes[160]. The observed lack of human macrophage involvement compared to the larger population of mouse macrophages also limits the model's capability to mimic this component of the human immune response.

Despite these limitation, human T-helper cells in the Hu-mouse model were able to distinguish between these biomaterials, which could indicate increased sensitivity to variations between xenogeneic versus allogeneic ECM or potentially other variables such as ECM age and material processing. The different responses suggested that the xenogeneic PMM is more favorable for eliciting a pro-remodeling immune response compared to the allogeneic HMM material, and supports its use in human trials. This study also demonstrates the utility of the Hu-mouse model for biomaterial testing, providing initial biocompatibility and evaluation of the immune response. With additional variables known to influence the immune response such as differences in the delivery method, location of implantation, and initial inflammatory state of the implantation site, there is much more potential utility with this model for evaluating the human immune cell response to biomaterial therapies. These results also warrant further mechanistic studies to improve our understanding of important human immune cell pathways to stimulate

biomaterial induced tissue repair. Future improvements being tested in Hu-mice models such as earlier maturation of B-cell populations before xenogeneic graft-versus-host disease becomes a concern could allow for assessment of human humoral response to biomaterial implants[161, 162]. These results, therefore, convey that testing a xenogeneic biomaterial in preclinical studies in a wild type or immunocompetent animal could be sufficient for assessing biocompatibility. However, a wild type rodent model is likely to be insufficient to test a human derived, allogeneic material, and the Hu-mouse model provides a more thorough model of the human T-cell response to these materials. Collectively, our results with the Hu-mouse model demonstrate the importance of pursuing more representative preclinical models in the biomaterials field for confirming biocompatibility and improving our understanding the human cell response to biomaterial therapies.

2.4 Methods and Materials

2.4.1 Fabrication of PMM, HMM, and NDM

Stocks of porcine derived non-decellularized (NDM), acting as a pro-inflammatory control, and decellularized myocardial matrix (PMM) along with human myocardial matrix (HMM) were created, developed and characterized according to established protocols as previously described[71, 130, 132]. From the ECM powder stocks, ECM material was partially digested with pepsin into a liquid form as previously described[130, 132]. Material aliquots were lyophilized and stored at -80°C until re-suspending with sterile water prior to injection.

2.4.2 Hydrogel Characterization

Immunohistochemistry was performed on the porcine derived material to assess removal of the alpha-gal epitope. Freshly isolated porcine left ventricular tissue, decellularized porcine myocardium, and porcine myocardial matrix hydrogels were fresh frozen in OTC for cyrosectioning. Sections (20 μm) were mounted onto glass slides, fixed in 4% paraformaldehyde for 10 minutes and permeabilized in acetone for 1.5 min. Slide samples were either stained with hematoxylin and eosin (H&E) or prepared for immunohistochemistry. Samples were blocked with a buffered solution containing bovine serum albumin (BSA) and stained for at least 12 hours at 4°C with M86 anti-alpha-gal (1:10, Enzo Life Sciences, Framingdale, NY) followed by incubation for 30 minutes with secondary anti-mouse Alexa Fluor 488 antibody (1:100, Life technologies, Carlsbad, CA)[163]. Hoechst 33342 was used to stain nuclei. Slides were imaged with a Carl Zeiss Observer D1 and Zeiss AxioVision SE64 software (Carl Zeiss, Jena, Germany).

2.4.3 Humanized Mouse Model

All experiments in this study were performed in accordance with the guidelines established by the committee on Animal Research at the University of California San Diego, and the American Association for Accreditation of Laboratory Animal Care.

NOD.Cg-Prkdc^{scid}Il2rg^{tm1wjl}/SzJ (NSG) (The Jackson Laboratory) mice of 6-10 weeks of age after conditioning with sublethal (2.25 Gy) total body irradiation underwent the following procedure, as previously described, to create the humanized mouse model (Hu-mice) [126]. First, the mice were transplanted under the kidney capsule with a piece of human fetal thymic tissue of about 1 mm^3 that had been previously frozen. Next, the animals were transfused intravenously with 1-5 x 10^5 human CD34$^+$ fetal liver cells from the same patient donor. Human fetal tissue, from Advanced Bioscience Resource, with gestational ages of 17-20 weeks was utilized.

2.4.4 Biomaterial Injection and Harvesting

Animals were briefly put under anesthesia using either 2.5% isoflurane or via injection with ketamine and xylazine. Each mouse was injected with only one type of biomaterial and received four 250 µL evenly spaced subcutaneous injections in the dorsal region. Each injection was premixed with 0.5 µL of sterile india ink to visually label the matrices for ease of identification upon harvesting. The injections, along with neighboring dermal tissue, were harvested three days and 1-week later. Injections were divided in half for either freezing in OCT for histological and immunohistochemistry (n=8-16) analysis, and the other half was flash frozen immediately in liquid nitrogen for processing for qRT-PCR analysis (n=8-12). Injections were performed in Hu-mice, and male wild-type Balb/c (Jackson Laboratories and Harlan Laboratories, respectively) that were age matched for comparison with a wild type immune system.

2.4.5 Quantitative Real-Time Polymerase Chain Reaction (qRT-PCR)

Flash frozen tissue samples were homogenized and then run through an RNEasy kit (Qiagen, Germantown, MD) along with an on-column DNase digestion step (Qiagen) to extract RNA with minimal genomic DNA contamination. Superscript III Reverse Transcriptase kit (Applied Biosystems, Foster City, MA) was used to synthesize cDNA. Then, SYBR Green PCR Master Mix (Applied Biosystems) was used with forward and reverse primers at a final concentration of 1 µM. Primers for T-helper cells were designed as mouse or human specific for analyzing Balb/c and Hu-mice samples, respectively, with lack of amplification with human primers confirmed in mouse samples. Primers included: mouse ARG1 (F: 5'-GAACACGGCAGTGGCTTTAAC-3', R: 5'-TGCTTAGTTCTGTCTGCTTTGC-3'), mouse NOS2 (F: 5'-CAGCTGGGCTGTACAAACCTT-3', R: 5'-CATTGGAAGTGAAGCGTTTCG-3'), mouse GATA3 (F: 5'- CTCGGCCATTCGTACATGGAA-3', R: 5'- GGATACCTCTGCACCGTAGC-3'), mouse TBX21 (F: 5'-AGCAAGGACGGCGAATCTT-3', R: 5'-GGGTGGACATATAAGCGGTTC-3'), human GATA3 (F: 5'-CGGCATCTGTCTTGTCCCTA-3', R: 5'-ATGCACGCTGGTAGCTCATA-3'), human TBX21 (F: 5'-ACAGCTATGAGGCTGAGTTTCGA-3', R: 5'-GGCCTCGGTAGTAGGACATGGT-3'), human CRTH2 (F: 5'-CCCTCTGGGCACTGGTAATC-3', R: 5'-CAGGTGGAGGAATGAGACGG-3') , human CCR5 (F: 5'-CAAAAAGAAGGTCTTCATTACACC-3', R': 5'-CCTGTGCCTCTTCTTCTCATTTCG-3'), and GAPDH (F: 5'-CATCAAGAAGGTGGTGAAGC-3', R: 5'-GTTGTCATACCAGGAAATGAGC-3'). Samples were run in technical duplicates along with negative controls without template cDNA to confirm lack of contamination in PCR reagents. PCR reactions were run on a CFX95™ Real-Time System (Biorad, Hercules, CA) with the following thermal cycler settings: 2 min at 50°C, 10 min at 95°C, 40 cycles of 15s at 95°C, and 1 min at 60-65°C based on pre-determined optimal primer efficiency amplification temperature. After completing 40 cycles of PCR amplification, automated melting curve analysis, consisting of increasing the thermal cycler temperature from 50°C to 95°C at 5°C increments lasting 5s each, was used to confirm formation of a singular

PCR amplicon for each primer set. Bio-Rad CFX Manager™ 3.0 (Biorad) was used for determining cycle threshold (ct) values from recorded SYBR green signal.

Gene expression ratios for assessing immune cell response polarization were calculated by modification of methods by Livak et al. for relative gene expression analysis[164]. The Δct was calculated between representative genes for either macrophage or T-helper cell polarized phenotypes. Fold change was then determined by $2^{-(\text{Gene 1} - \text{Gene 2})}$ and normalized to fold change of corresponding NDM ratios for comparison. Ratios of ARG1/NOS2 and GATA3/TBX21 were selected to quantify macrophage and T-helper cell polarization, respectively, with CRTH2/CCR5 specifically for assessment of human T-helper cells. GAPDH values were determined to confirm consistent loading between PCR reactions.

2.4.6 Histology and Immunohistochemistry

Fresh frozen tissue in OCT were cryosectioned to obtain a transverse section of the biomaterial and neighboring dermal tissue. Cryosections from three different evenly spaced locations were used for all immunohistochemistry. Slides were fixed with acetone or 4% paraformaldehyde and blocked with a buffered solution containing bovine serum albumin, goat serum and/or donkey serum based on the optimized antibody protocol. The following primary antibodies were incubated for 1 hour at room temperature or for 12-18 hours at 4°C: anti- F4/80 (1:200 dilution, eBiosciences, San Diego, CA), anti-iNOS (1:50 dilution, Abcam, Cambridge, MA), anti-CD206 (1:50 dilution, Santa Cruz, Dallas, TX), anti-mCD3 (1:100 dilution, Abcam), anti-mCD4 (1:200 dilution, Bioss, Woburn, MA), anti-mCD8 (1:200 dilution, Bioss), anti-human nuclei (1:250 dilution, Millipore), anti-hCD3 (1:50 dilution, Abcam), anti-hCD4 (1:50 dilution, Becton Dickinson, Franklin Lakes, NJ), anti-hCD8 (1:500 dilution, Becton Dickinson). The following secondary antibodies were incubated for 30-45 minutes at room temperature: anti-rat Alexa Fluor 568 (1:250 dilution), anti-rabbit Alexa Fluor 488 (1:500 dilution), anti-mouse Alexa Fluor 488 (1:500 dilution), anti-rat Alexa Fluor 488 (1:400 dilution), anti-rabbit Alexa Fluor 568

(1:200 dilution), and anti-rabbit Alexa Fluor 647 (1:200 dilution). Bright field images were taken with Leica Aperio ScanScope® CS^2 and fluorescent images with the Leica Ariol® system (Leica). Cellular density and human nuclei quantification were done via an automated counting program as part of the Leica Ariol® system and confirmed with a custom MATLAB script (Mathworks, Natick, MA). Macrophage and T-cell co-staining quantification was done via custom MATLAB scripts. Biomaterial outline was drawn based on initial brightfield scans that was translated to subsequent fluorescent scans on the Ariol® system and core of the biomaterial determined as 200 μm interior to the designated biomaterial outline based on a custom MATLAB script.

2.4.7. Statistics

All data and plots are presented as mean ± SEM. Significance was determined with a one-way ANOVA using a Tukey post-hoc test for histology and qRT-PCR data, and an unpaired student's *t*-test with a $p<0.05$.

2.4 Acknowledgements

The authors would like to thank Matt Joens for his technical expertise in scanning electron microscopy. The authors would also like to thank Lifesharing for their assistance in obtaining the human cardiac tissue. Funding for this work was provided by CIRM (TR3-05559 and TR1-01277 to YX) and the NIH NHLBI (HL113468 to KLC). RMW received funding during the project from the NHLBI as a training grant recipient. TDJ received funding during the project as a Powell Fellow from the Powell Foundation, the NHLBI as a training grant recipient, and the NSF as a graduate student fellow. KLC is co-founder, consultant, board member, and holds equity interest in Ventrix, Inc.

Chapter 2, in part, is a reprint of the material as it is published in: Raymond M. Wang, Todd D. Johnson, Jingjin He, Zhili Rong, Michelle Wong, Vishal Nigam, Atta Behfar, Yang Xu and

Karen L. Christman. “Humanized mouse model for assessing the human immune response to xenogeneic and allogeneic decellularized biomaterials.” Biomaterials 129, 98–110 (2017). The dissertation author was a primary author of this paper.

CHAPTER 3: Mast Cells Contribute to the Immunomodulatory Effect of the Biomaterial Microenvironment in a Gender Specific Manner

3.1 Introduction

Regulation of the immune response contributes to the severity and outcomes in various disease conditions, and bioactive immunomodulatory biomaterials have shown promise for influencing these responses towards a favorable resolution. In this study, we investigated the role of mast cells in the regulation of immune microenvironment response to biomaterial scaffolds. Therapies that stimulate endogenous tissue repair such as decellularized biomaterials derived from isolated tissue extracellular matrix (ECM) are known to induce these effects based on immunomodulatory mechanisms[3]. Although this immunomodulatory influence has been rigorously evaluated with macrophage and T cell populations, potential contribution of mast cells to the immunomodulatory effect of naturally derived materials has been understudied. Notably, myocardial matrix hydrogel delivery in a rat ischemia reperfusion model showed a significantly increased presence of tryptase$^+$c-kit$^+$ mast cell presence in myocardial matrix treated hearts compared to saline controls along with improved cardiac function, reduced fibrosis, and immunomodulation towards an anti-inflammatory/pro-remodeling response[4]. Mast cells in the injured hearts when untreated are largely overlooked due to their limited numbers compared to other immune populations[5] or considered detrimental with studies limiting degranulation or removing mast cell presence in ischemia reperfusion models leading to improved outcomes[6, 7]. However, as efficacy and safe immunological interaction of myocardial matrix hydrogels has extensively evaluated in murine[4, 8], porcine[9], and humanized mice models[10] along with safe deployment in human patients[11], these results suggest the observed increase of mast cell presence does not negatively contribute to myocardial matrix treated cardiac remodeling. As various immune cells are known to take on different phenotypic states based on stimuli, alternative stimuli could promote beneficial mast cell contribution[12]. Therefore, we explored the role mast cells play in regulation of induced immunomodulatory responses,

demonstrating its critical regulatory contribution to the pro-inflammatory to pro-remodeling transition that deviates in a gender specific manner.

In comparison to the study of macrophages and T cells described in Chapter 2, mast cells are an understudied cell population, in particular, from the biomaterials field, despite its capabilities to strongly influence the immune response. This limited scope of study likely stems from their difficulty to work with, lack of cell specific secreted factors, limited numbers *in vivo*, and various functions that have been demonstrated for this cell type. To address these issues, we utilized a mast cell knockout model and rescue model to determine mast cell specific contributions to the immune response to an injectable ECM biomaterial scaffold. In mast cell knockout mice, dysregulation of the expected M1 to M2 macrophage transition from the immunomodulatory effect of an ECM derived biomaterial scaffold was observed. Polarization progression deviated in a gender specific manner with an early transition to an M2 profile in female mice, while the male response was unable to properly transition past a pro-inflammatory M1 state, that were both reversed with mast cell adoptive transfer. Further investigation of the later stage immune response in male mice determined a maintained pro-inflammatory gene expression profile, particularly consisting of members from the IL-1 cytokine family and related downstream pathways. As mast cells are mainly associated with detrimental pro-inflammatory outcomes for biomaterial scaffolds, these results demonstrate their contribution to induced immunomodulatory therapies and support their potential as a critical immune regulatory element that can be manipulated for stimulating endogenous tissue repair.

3.2 Results

The immune response is known to have a necessary role in tissue homeostasis, remodeling, and repair, and our understanding of the involved immune populations and their phenotypic state improves our capacity to treat adverse disease conditions. Mast cells are tissue resident granulocytes classically associated in host defense, proinflammatory responses

and various immune disorders[165]. The granules of mast cells are known to contain a variety of immune mediators demonstrated to contribute to pathological responses such as allergic reactions, inflammatory cell recruitment[166], and fibrosis[167]. While mast cells are also known to secrete a plethora of pro-remodeling/anti-inflammatory cytokines that are relevant for tissue repair, their role in tissue regenerative therapies has not been studied.

Biomaterial scaffolds that influence the immune response are emerging as a viable clinical strategy for tissue repair and regeneration[168]. Although this immunomodulatory influence associated with improved tissue outcomes has been rigorously evaluated with macrophage[169, 170] and T cell populations[171, 172], potential contribution of mast cells to the immunomodulatory effect of naturally derived biomaterials has been largely ignored. Studies have mainly just evaluated shifts in mast cell numbers associated with biomaterial deployment, though their general low numbers in tissue make it difficult to determine conclusive results from this approach[173, 174]. Early studies with synthetic materials have focused on their functional role and mainly produced results characteristic of a classical mast cell phenotype highlighting contributions to early acute inflammatory cell infiltration[166], and fibrous capsule formation[175]. From a general tissue disease perspective, several studies have similarly emphasized their detrimental role to tissue remodeling outcomes[176-178]. However, research has also produced confounding results[179-182] or evidence of their beneficial contributions to select cases of native tissue repair or inflammatory resolution[180, 183, 184], suggesting a greater functional complexity and potential to be utilized in therapeutic design. Based on recent evidence suggesting that mast cells can have beneficially influences on native tissue remodeling outcomes, we explored the role mast cells play in regulation of biomaterial scaffold-induced immunomodulatory responses, demonstrating its critical regulatory contribution to the pro-inflammatory to anti-inflammatory/pro-remodeling transition that deviates in a gender specific manner.

Given the recent clinical and rapidly expanding pre-clinical use of decellularized biomaterials derived from isolated tissue extracellular matrix (ECM), which are known to induce

these effects based on immunomodulatory mechanisms[169, 171, 172],we chose to evaluate this class of biomaterial scaffold in $Kit^{W\text{-}sh}$ mast cell knockout mice. In particular, we used an injectable hydrogel form of myocardial matrix, which was previously shown to be immunomodulatory[185, 186] and recently progressed through a Phase I clinical trial in post-myocardial infarction patients[187]. To study the influence of mast cells on the response to biomaterial scaffolds, we subcutaneously injected the ECM hydrogel into the dorsal region of male and female $Kit^{W\text{-}sh}$ mast cell knockout mice and compared the recruitment of surrounding immune cell populations to wild-type C57BL6/J mice. Day 1 isolated subcutaneous injections showed mast cell presence at low cellular density as early as day 1 post-injection. Mast cells were non-degranulated or minimally degranulated based on toluidine blue staining while knockout mice showed no mast cell presence in the material or throughout the skin (Figure 3.1A, B).

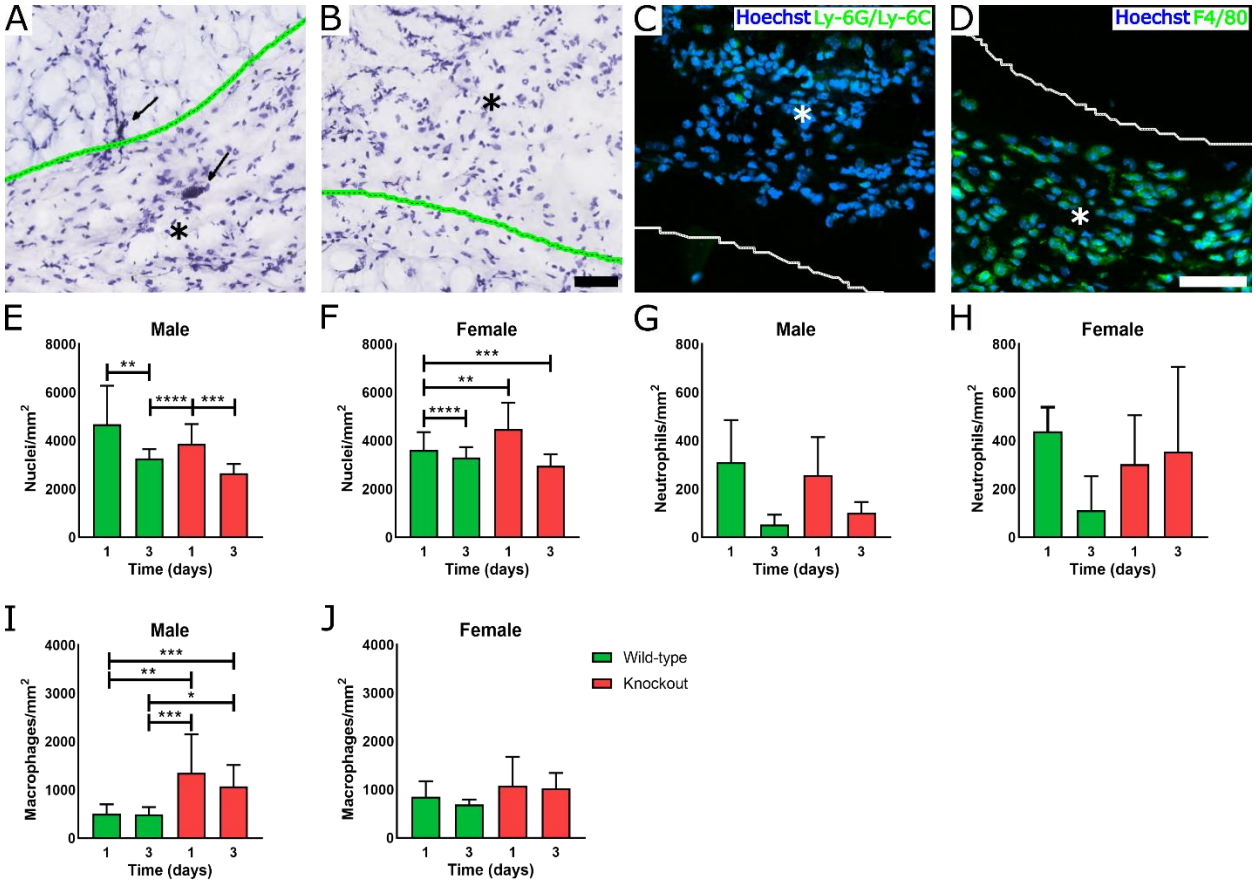

Figure 3.1**:** ECM scaffold promotes early immune cell infiltration with or without mast cells. Representative images of toluidine blue staining of myocardial matrix hydrogel (green outlined with asterisk where material is present) and neighboring dermal tissue in wild-type (A) and knockout (B) mice at day 1 post-injection. Mast cells can be found as early as day 1 showing lack of or minimal degranulation (black arrow). Representative fluorescent images of injected biomaterial (white outlined with asterisk) with Ly-6G/Ly-6C$^+$ neutrophil (C) and F4/80$^+$ pan-macrophage staining (D) in green, and Hoechst nuclei counterstain in blue. Quantification of total nuclei (E, F), neutrophil (G, H) and macrophage (I, J) density at one and three days post-injection for male and female wild-type (green) and knockout (red) mice. Scale bar of 50 μm in toluidine blue (A-B) and fluorescent images (C, D, G, H). (*$p < 0.05$, **$p < 0.01$, ***$p < 0.001$ and ****$p < 0.0001$).

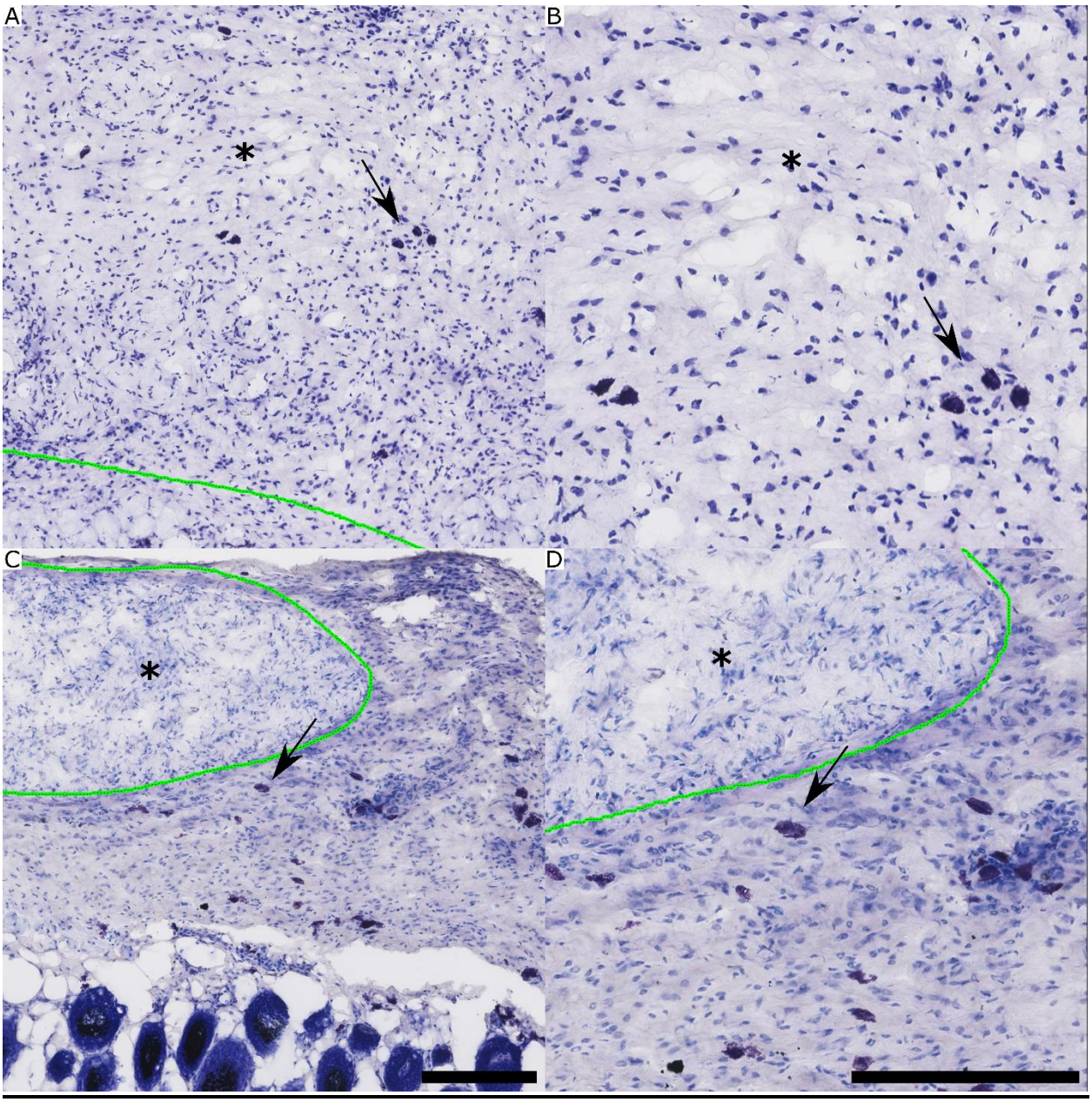

Figure 3.2: Mast cell presence in and/or around ECM injections. Representative images of toluidine blue staining of (A, B) ECM hydrogel scaffold and (C, D) milled urinary bladder matrix (material outlined in green with asterisk on side where material is present) and neighboring dermal tissue in male wild-type 3 days post-injection. Mast cells staining is indicated by a black arrow. Scale bar is 200 µm.

Similar characteristics of mast cells along with greater inward infiltration were observed for the ECM scaffold isolated at 3 days post-injection (Figure 3.2A, B). Comparison with subcutaneous injection of milled urinary bladder matrix showed a similar non-degranulated state

of mast cells bordering the material at day 3 post-injection demonstrating that these observations were not specific to the ECM hydrogel (Figure 3.2C, D). Quantification of total cellular infiltration into the ECM hydrogel scaffold along with staining for Ly-6G/Ly-6C$^+$ neutrophil (Figure 3.1C) and F4/80$^+$ macrophage populations (Figure 3.1D) showed similar or greater infiltration in knockout mice compared to wild-type mice (Figure 3.1E-J). These results contrast with those observed with implanted synthetic materials where mast cell knockout led to decreased infiltration of macrophages and neutrophils[166], which mast cells are known to normally support through release of histamine, causing vasodilatation and increased vascular permeability, and chemokines. *In vitro* assessment of interaction of differentiated bone marrow derived FcƐRI$^+$c-kit$^+$ mast cells with the ECM hydrogel solution at non-gelling concentrations in comparison to collagen and media only controls showed higher alamarBlue^{TM} readings conveying matrix interaction enhanced mast cell viability (Figure 3.3).

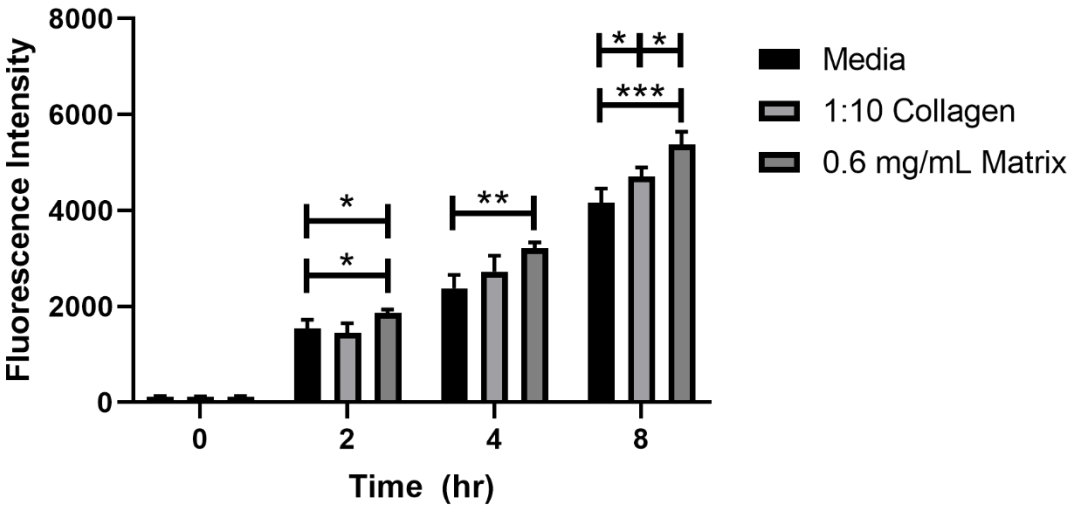

Figure 3.3**:** Increased mast viability with ECM doped into media. Four week differentiated bone marrow derived mast cells were incubated ECM hydrogel material, collagen or culture media control. AlamarBlue^{TM} fluorescent readings were taken at 0, 2, 4, and 8 hours following plate set-up (n = 4 per group). (*$p < 0.05$, **$p < 0.01$, ***$p < 0.001$).

As ECM scaffold injection allowed for cellular infiltration similar to wild-type mice despite the lack of mast cells (Figure 3.1), a screen of immune cell populations and polarized phenotypes through flow cytometry and gene expression markers was utilized to assess if these infiltrating cells were affected by loss of regulatory contributions from mast cells. Transient polarization of immune cells from a pro-inflammatory to a pro-remodeling phenotype is a characteristic of wound healing responses[49, 170, 188] and the immunomodulatory effect of ECM scaffolds promotes this transition[172, 189]. Macrophage polarization assessment based on ratio of M2 pro-remodeling and M1 pro-inflammatory phenotypic markers in male mice showed a significant lack of polarization shift towards M2 for mast cell knockout mice at day 11 post-injection that was observed in wild-type mice (Figure 3.4A) and in previous studies[186].

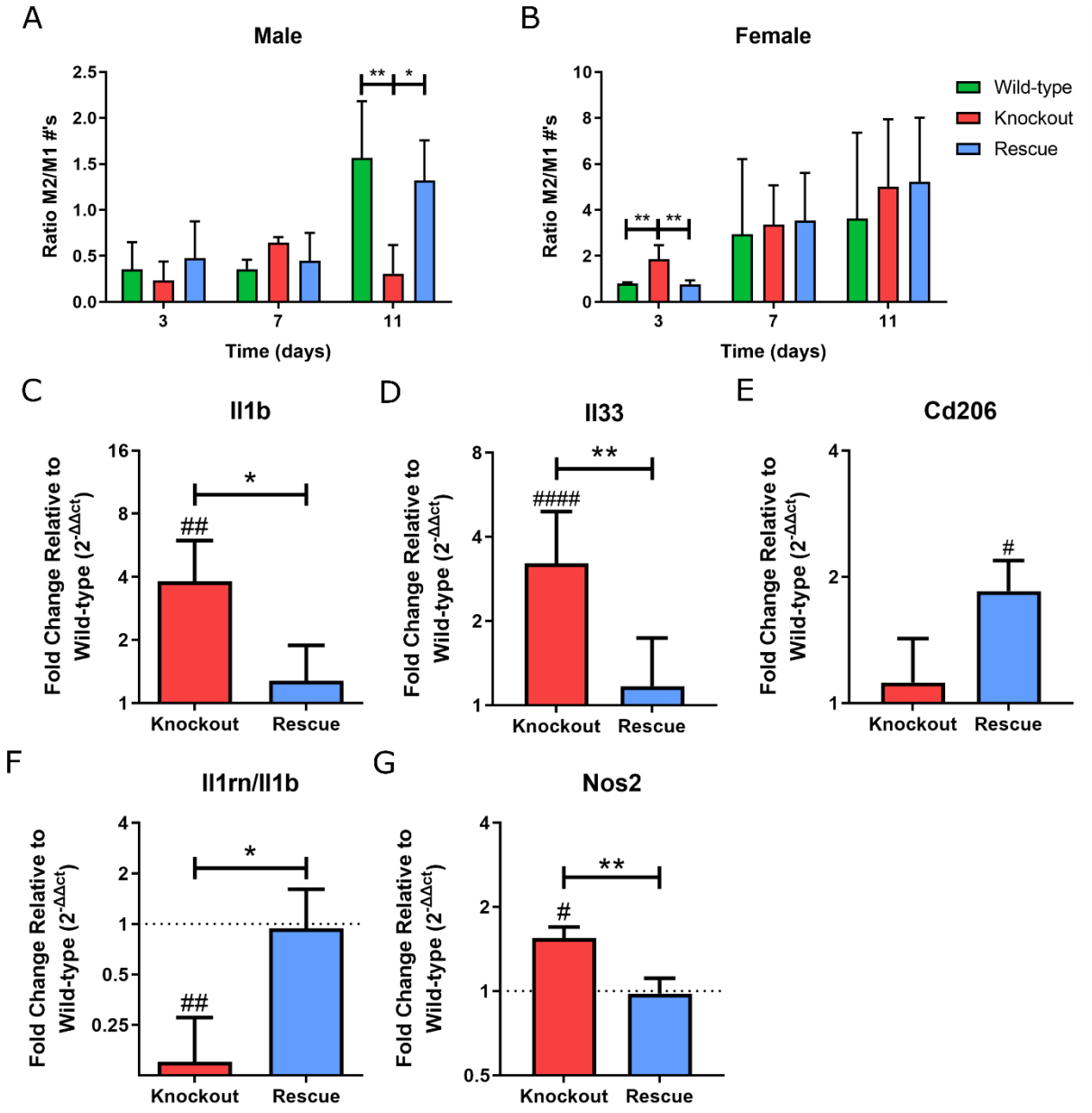

Figure 3.4: Transition from a pro-inflammatory to pro-remodeling macrophage and cytokine immune profile is dysregulated in a gender specific manner. Flow cytometry quantification for macrophages polarization based on a ratio of $CD206^+$ M2 versus $CD86^+$ M1 macrophage counts was assessed at three, seven, and eleven days post-injection between wild-type (green), knockout (red), and rescue (blue) male (A) and female mice (B). Relative gene expression normalized to wild-type expression at day 11 in male mice measured by qPCR for (C) Il1b, (D) Il33, and (H) Cd206 relative to housekeeping gene, Gapdh. (F) Gene expression ratio of Il1b to receptor antagonist, Il1rn. (G) Relative gene expression at day 3 in female mice measured by qPCR for Nos2 relative GAPDH housekeeping gene. # indicates significance relative to wild-type expression, * conveys significance between knockout and rescue, and gene expression plotted as mean ± SEM. ($^{\#}p < 0.05$, $^{\#\#}p < 0.01$, $^{\#\#\#\#}p < 0.0001$, $^{*}p < 0.05$, and $^{**}p < 0.01$).

To confirm that this shift was mast cell specific, mast cell rescue mice where adoptive transfer of bone marrow derived mast cells differentiated *in vitro* were delivered subcutaneously into knockout mice to reconstitute the local resident mast cell population were similarly assessed[190]. These mice showed a restoration of the M2 shift, which was significant to the knockout group (Figure 3.4A). Assessing the individual percentages of M2 and M1 macrophages showed similar percentages of M2 and M21 macrophages (Figure 3.5A, G) for the wild-type and knockout mice while a higher relative number of M1 macrophage was present in knockout mice at the day 11 (Figure 3.5E). Notably, addition of mast cells in the rescue mice had a significantly greater percentage of M2 macrophages compared to knockout mice. This result further supports an alternative mast cell phenotype from ECM scaffold interaction as opposed to a classically activated phenotype that would promote greater M1 macrophage presence. In contrast, female mice showed an M2 dominant presence at the early day 3 timepoint with significant results based on count ratios (Figure 3.4B), which arose from a higher relative percentage of M2 macrophages (Figure 3.5D) and not from differences in M1 or M21 macrophage percentages (Figure 3.5F, H). The early observation of a M2 dominant response could result from influences of female hormones such as estrogen, which has been demonstrated to accelerate resolution of pro-inflammatory responses[191]. Furthermore, female hormones are known to influence mast cell activation contributing to the enhanced host defense and greater incidents of autoimmune disease in females[165, 192]. Notably, there were no changes in either gender in total macrophage numbers (Figure 3.5A, B) and other assayed populations including T-cells subpopulations (Figure 3.6), B cells (Figure 3.7), dendritic cells (Figure 3.8), and mast cells (Figure 3.9). Thus, the results stemmed from phenotypic changes in immune cell polarization versus differences in general immune cell numbers between models.

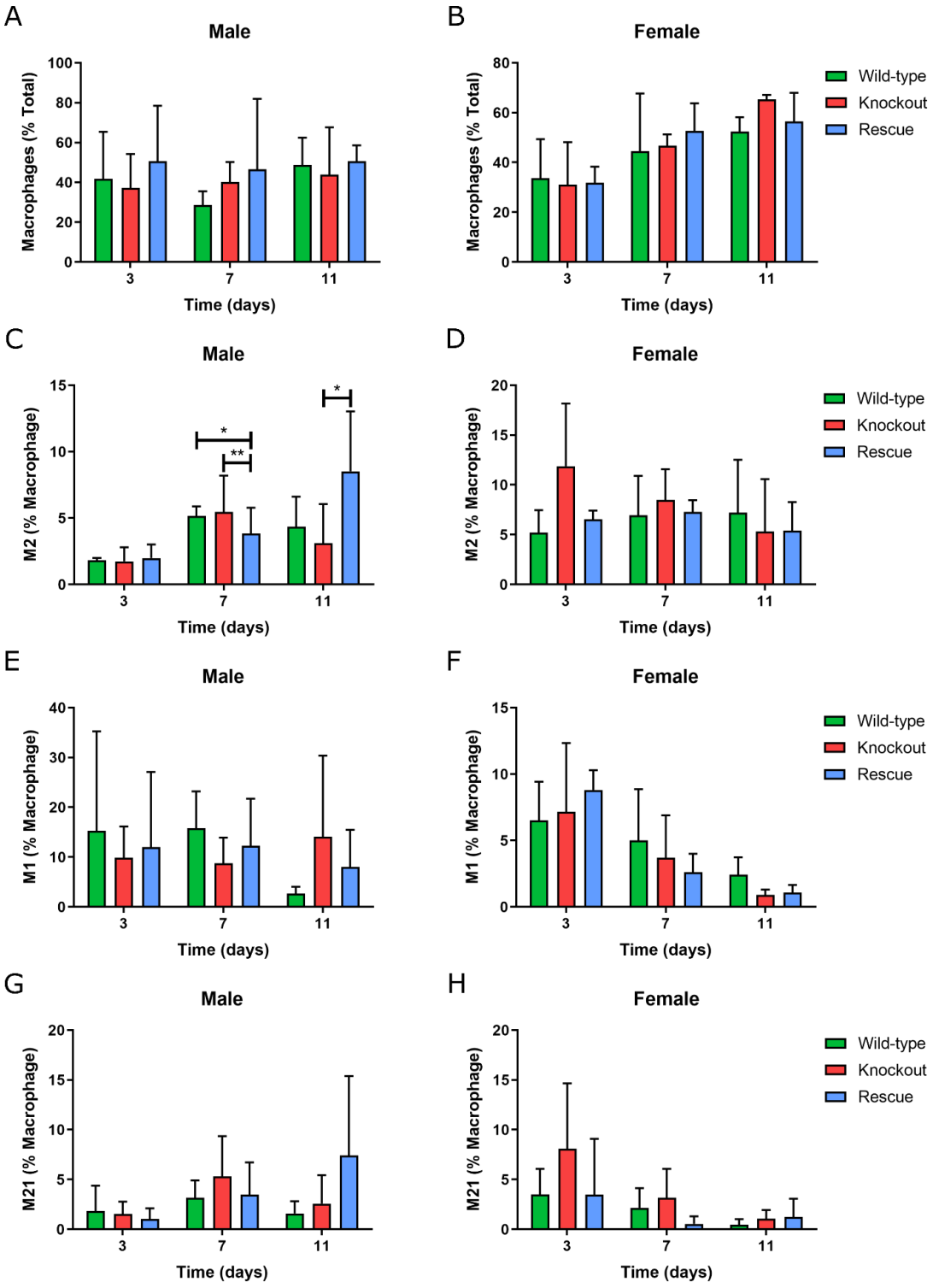

Figure 3.5: Flow cytometry of total and macrophage polarized subpopulations. Percentages of total F4/80^{+} macrophages relative to live cells (A, B), and CD206^{+} M2 (C, D), CD86^{+} M1 (E, F) and co-expressing CD206^{+}CD86^{+} M21 (G, H) macrophages relative to total macrophages at three, seven, and eleven days post-injection between wild-type (green), knockout (red), and rescue (blue) male (A, C, E, G) and female mice (B, D, F, H).

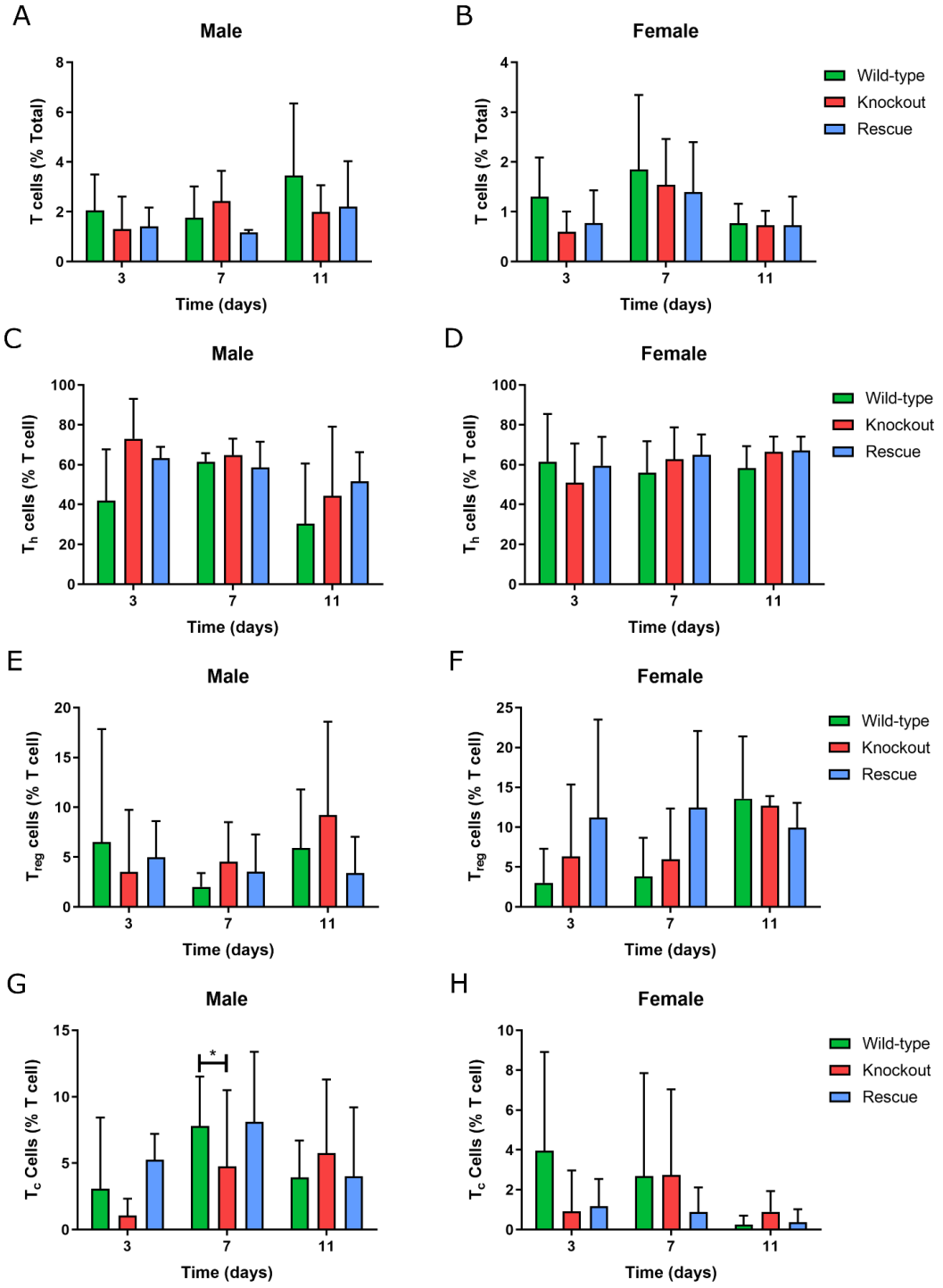

Figure 3.6: Flow cytometry of total T cells and differentiated subpopulations. Percentages of total $CD3^+$ T cells relative to total live cells (A, B), and $CD4^+$ T-helper (T_h) cells (C, D), $CD4^+FOXP3^+$ regulatory T (T_{reg}) cells (E, F) and $CD8^+$ cytotoxic T (T_c) cells (G, H) relative to total T cells at three, seven, and eleven days post-injection between wild-type (green), knockout (red), and rescue (blue) male (A, C, E, G) and female mice (B, D, F, H).

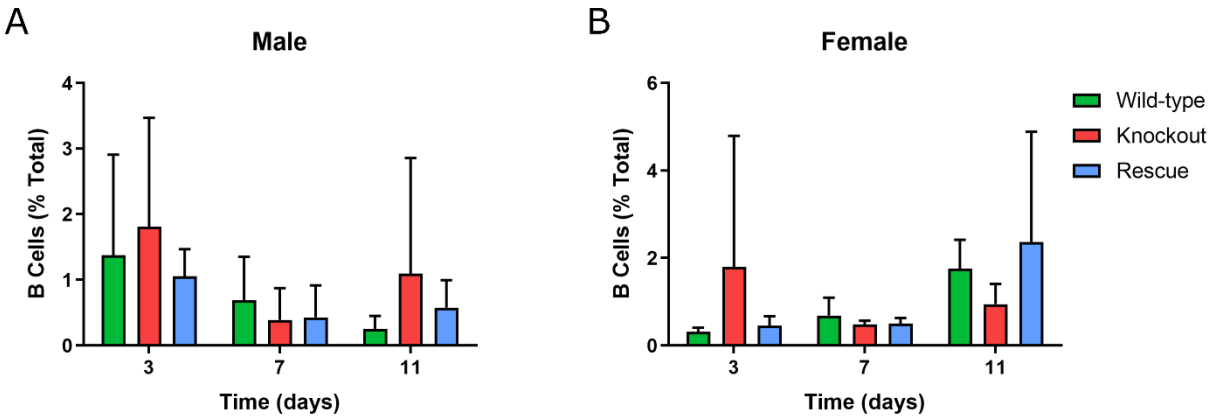

Figure 3.7: Flow cytometry of B-cells. Percentages of $CD19^+$ B cells relative to total live cells at three, seven, and eleven days post-injection between wild-type (green), knockout (red), and rescue (blue) male (A) and female mice (B).

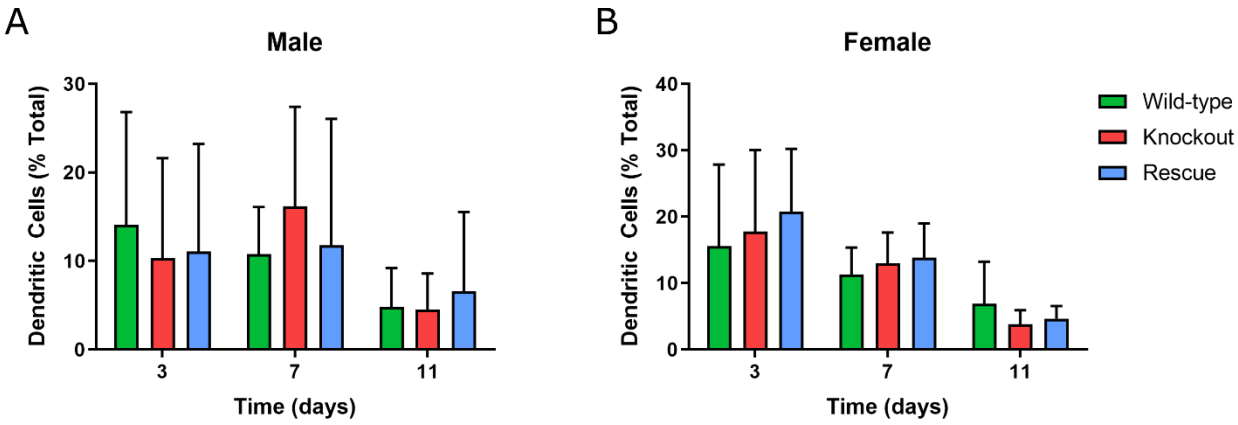

Figure 3.8: Flow cytometry of Dendritic Cells. Percentages of $CD11c^+F4/80^-$ dendritic cells relative to total live cells at three, seven, and eleven days post-injection between wild-type (green), knockout (red), and rescue (blue) male (A) and female mice (B).

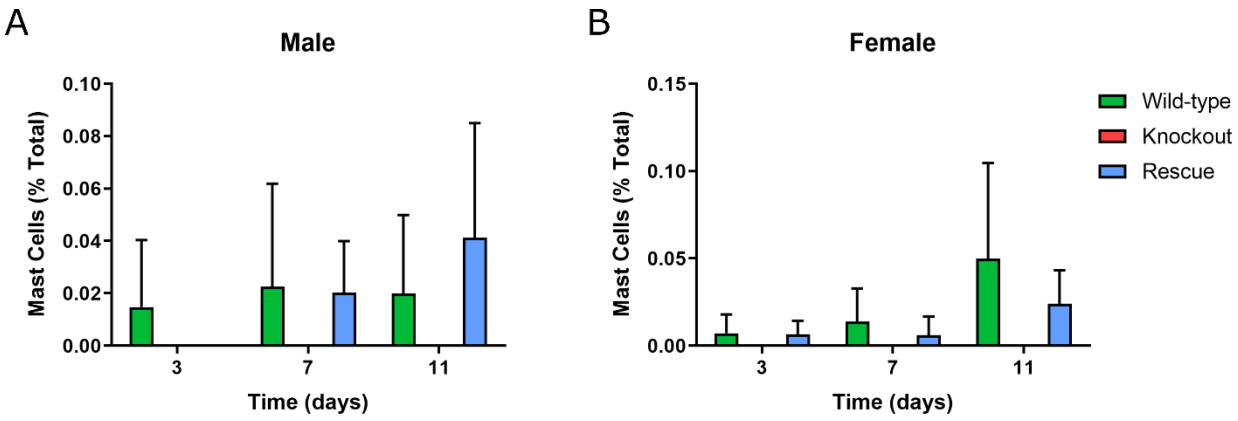

Figure 3.9: Flow cytometry of Mast Cells. Percentages of $CD117^{+}Fc\text{Ɛ}RI^{+}$ mast cells relative to total live cells at three, seven, and eleven days post-injection between wild-type (green), knockout (red, not present), and rescue (blue) male (A) and female mice (B).

A gene expression screen of select pro-inflammatory and pro-remodeling/anti-inflammatory markers between the wild-type and knockout group showed only a significant increase in anti-inflammatory Il38 in knockout compared to wild-type at day 3 post-injection (Figure 3.10A). At day 11 when significant shifts based on flow cytometry were observed, significant differences in the IL-1 family including increases in pro-inflammatory Il1b, and anti-inflammatory Il33 expression, and a decrease in Il38 (Figure 3.10B).

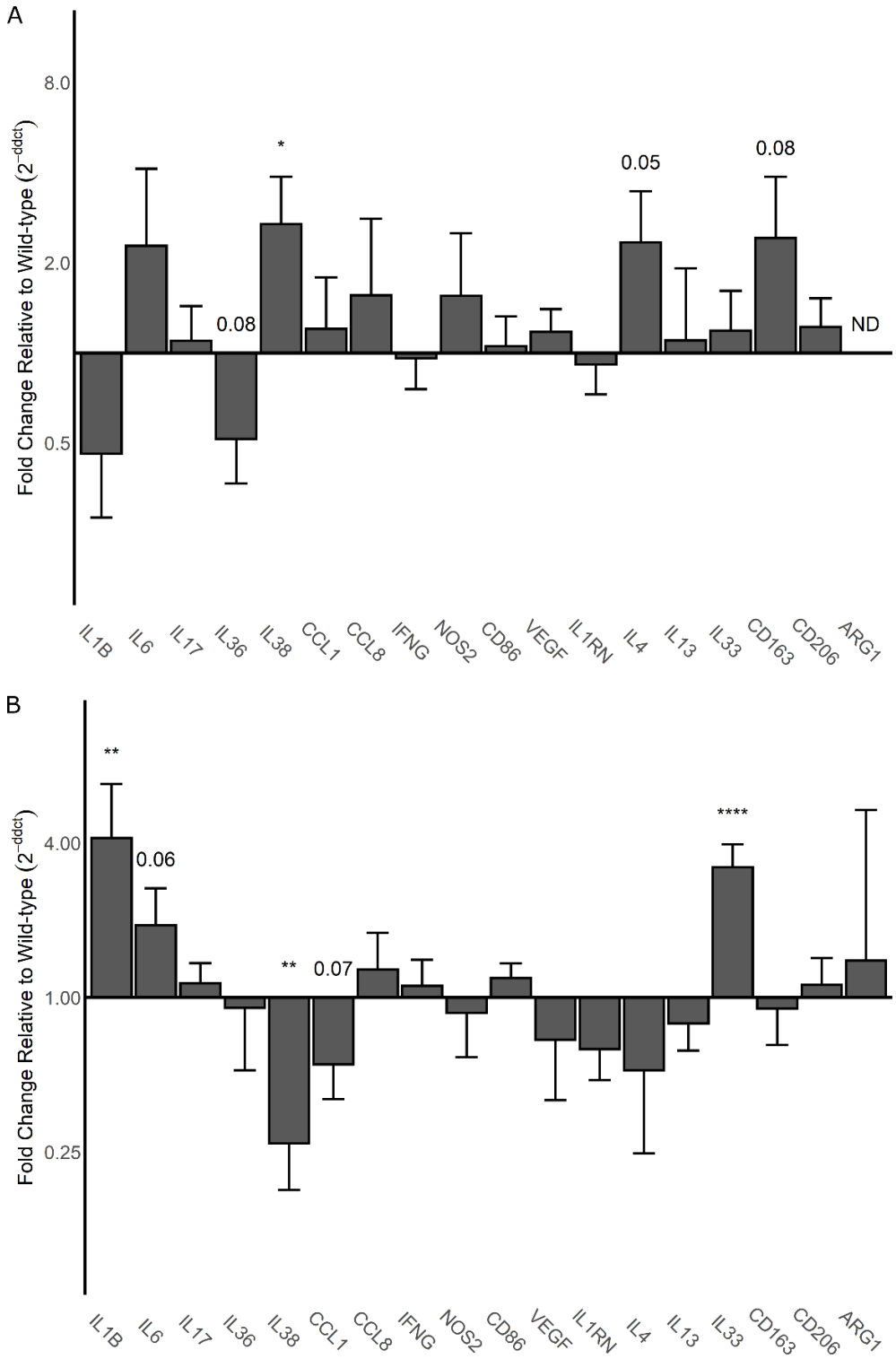

Figure 3.10: Screen of knockout versus wild-type gene expression in male mice. qPCR results of pro-inflammatory versus pro-remodeling immune markers at day 3 (A) and day 11 (B) in male mice. Fold change and significance of knockout mouse sample gene expression was normalized relative to wild-type gene expression. Gene expression plotted as mean ± SEM. (ND = not detected, value displayed for trend $p < 0.1$, *$p < 0.05$, **$p < 0.01$, and ****$p < 0.0001$).

Further comparison with rescue mice showed that increased expression of Il1B relative to housekeeping gene, Gapdh, and IL-1 receptor antagonist, Il1rn, and Il33 in knockout mice were reversed in the rescue mice supporting mast cell influence on the IL-1 cytokine family response (Figure 3.4E, D, F). Although IL-33 is a type 2 T-helper cell associated cytokine, lack of increased gene expression of associated cytokines, Il4 and Il13, suggests an overall pro-inflammatory profile driven by increased expression Il1b and decreased expression of Il38 (Figure 3.10B). Notably, expression of Cd206 was significantly upregulated in rescue mice compared to wild-type controls, matching previous flow cytometry results of an increased M2 macrophage transition from mast cell interaction with the ECM scaffold (Figure 3.4E, Figure 3.5C).

Similar assessment for female mice at day 3 when dysregulation of macrophage polarization was observed by flow cytometry (Figure 3.4B) determined only a significant upregulation of M1 marker Nos2 in knockout mice compared to wild-type that was reversed in rescue mice (Figure 3.4G, 3.11).

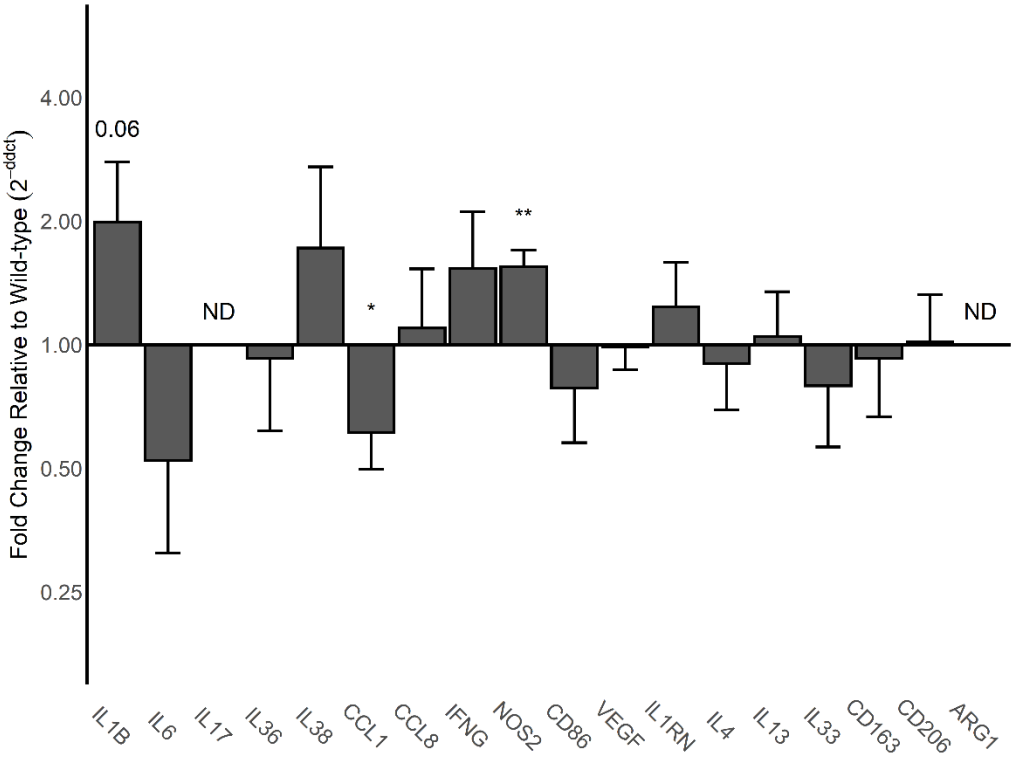

Figure 3.11: Screen of knockout versus wild-type gene expression in female mice. qPCR results of pro-inflammatory versus pro-remodeling immune markers at day 3 in female mice. Fold change and significance of knockout mouse sample gene expression was normalized relative to wild-type gene expression. Gene expression plotted as mean ± SEM. (ND = not detected, value displayed for trend $p < 0.1$, *$p < 0.05$, **$p < 0.01$).

Though this result could be considered contradictory to the flow cytometry results suggesting a greater M2 profile at this timepoint (Figure 3.4B), studies on the influence of female hormones have shown specific upregulated expression of Nos2[193, 194], potentially suggesting the known interaction of mast cell with female hormones helps to regulate these responses[195]. Overall, loss of mast cells in male mice inhibited pro-inflammatory to pro-remodeling transition of macrophage and cytokine profiles, while this transition was accelerated in female mice.

There are known limitations to summarizing the immune response with a few selected markers as a wide array of immune cell populations and cytokine mediators are known to influence the immune response. Thus, a more comprehensive multiplex analysis was carried

out through a Nanostring panel directly probing the RNA molecular content for 561 of immune related targets. Day 11 male mouse samples were assessed as results supported a lack of pro-inflammatory resolution in knockout mice at this timepoint. PCA analysis showed that the majority of wild-type and rescue samples clustered together. Knockout samples were mostly separately grouped and not tightly clustered conveying increased variance due to removal of regulatory influence from mast cells (Figure 3.12).

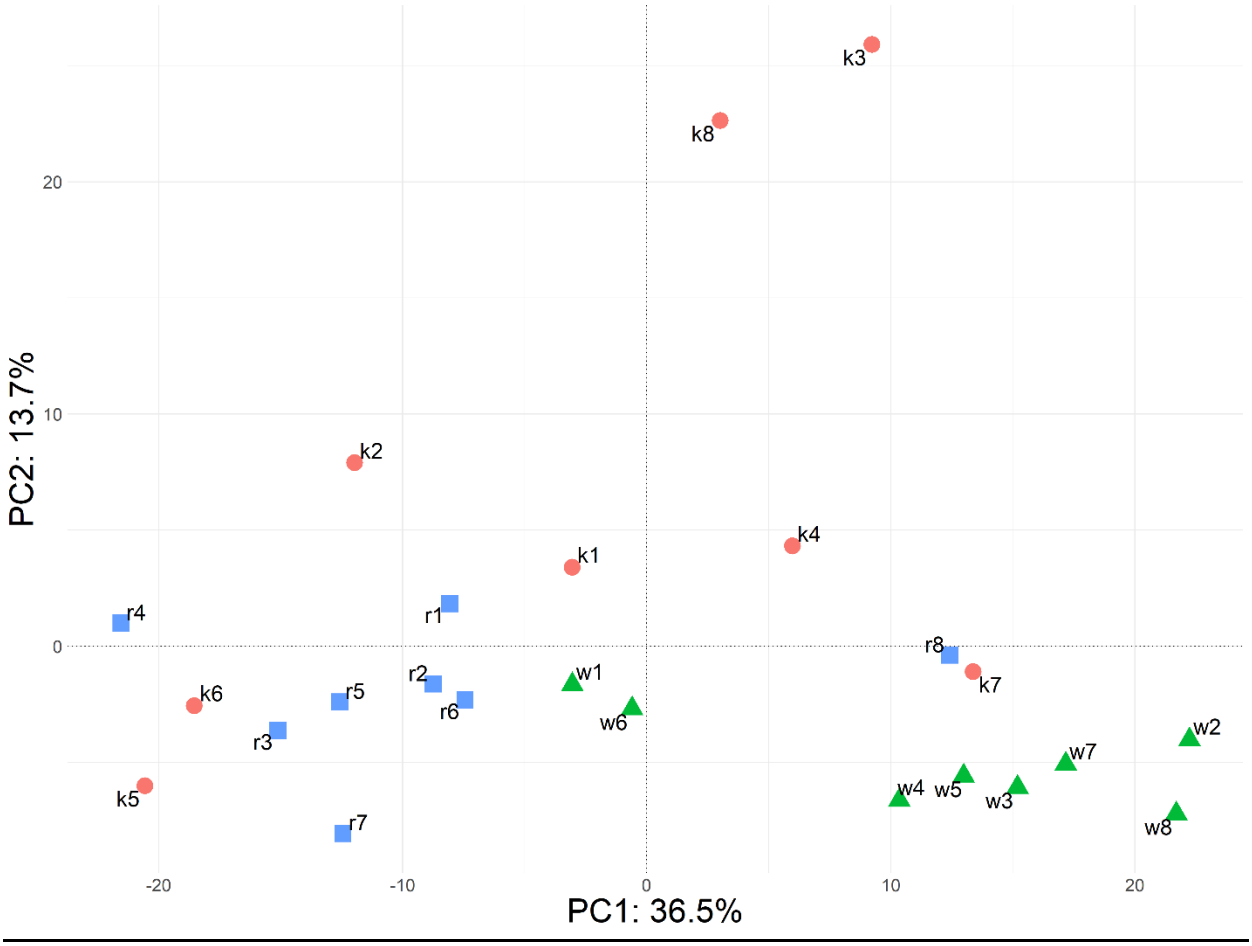

Figure 3.12: Principal component analysis plot of Nanostring nCounter data. PC1 (36.5% of variance) versus PC2 (13.7% of variance) of normalized gene expression based on the NanostringDiff package method with wild-type, w1-w8 (green triangles), knockout, k1-k8 (red circles), and rescue, r1-r8 (blue squares).

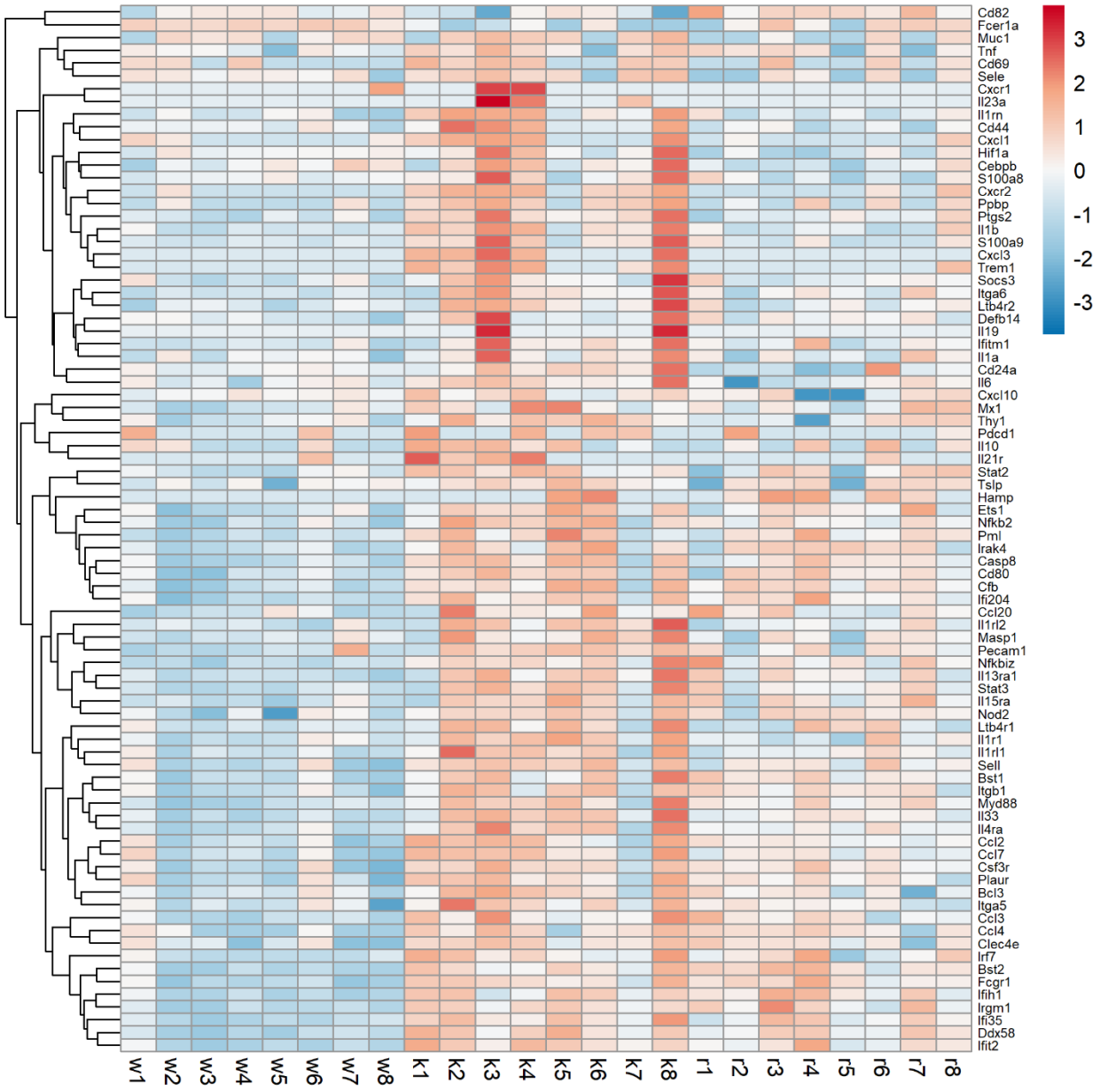

Figure 3.13: Heatmap of wild-type, knockout, rescue gene expression. Z-scores of Nanostring nCounter gene expression data normalized based on the NanostringDiff package method and displayed with pheatmap package in R. Sample ID of wild-type (w1-w8), knockout (k1-k8), and rescue mouse sample (r1-r8) for male mice at day 11 post-injection. Upregulated expression in red and downregulated in blue.

Similarly, Z-score heatmap of normalized gene expression showed a differing profile of immune knockout samples compared to wild-type and rescue samples (Figure 3.13).

Differential expression analysis of the knockout compared to the wild-type and rescue response

determined differentially upregulated genes for a host of pro-inflammatory cytokines (Il1b, Il6, Ifng, Tnf) and chemokines (Ccl3, Ccl4, Ccl7, Cxcl1, Cxcl3) (Figure 3.14, Table 3.1).

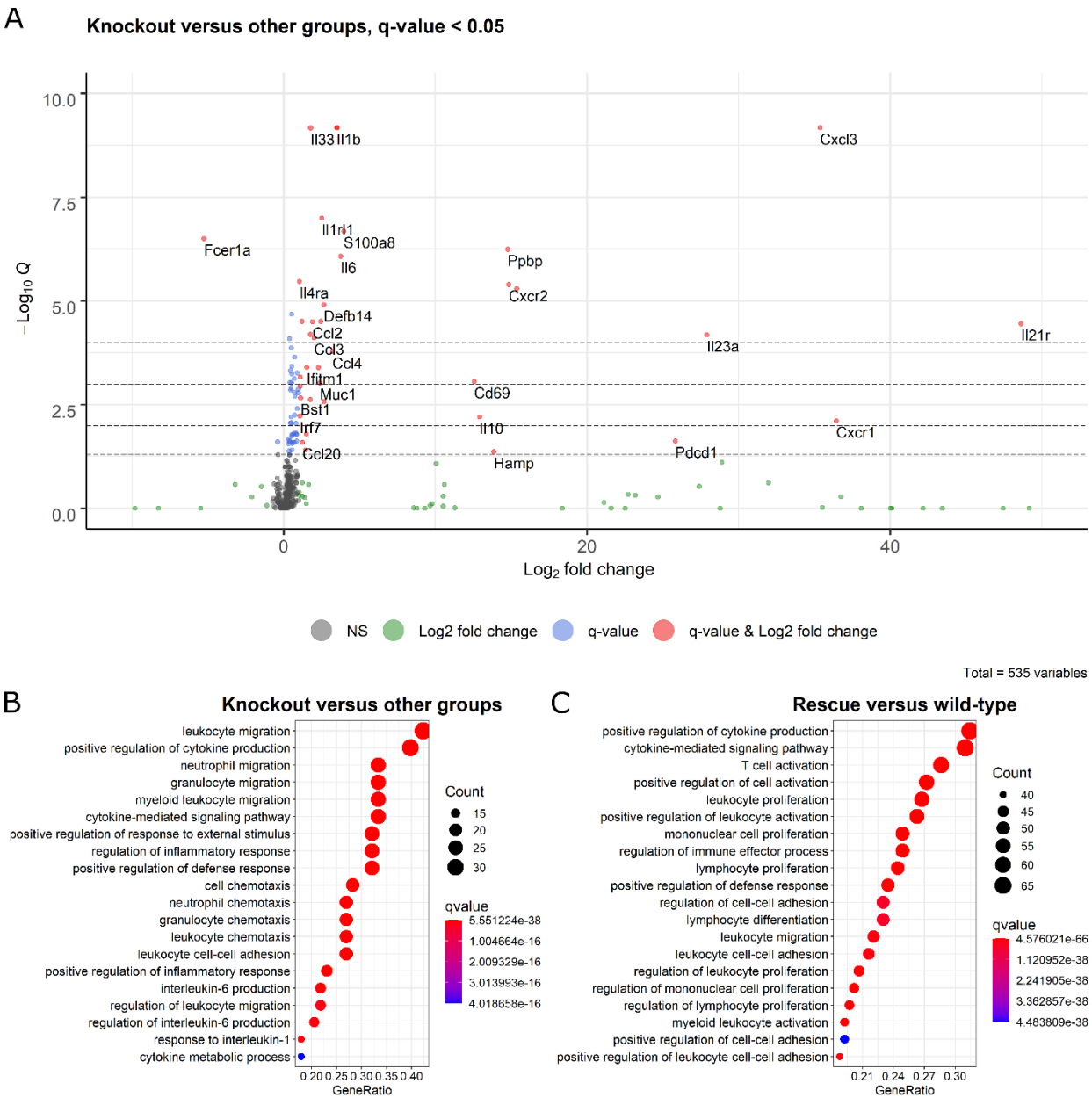

Figure 3.14: Mast cell knockout in male mice maintains late pro-inflammatory response to biomaterial implantation while rescue restores immunomodulatory effects. (A) Differential expression with dots indicating false discovery rate less than 0.05 (blue, red), absolute fold change greater than 1.5 (green, red) or non-significant (black). Dashed lines indicating different significance thresholds (*q < 0.05, **q < 0.01, ***q < 0.001 and ****q < 0.0001). Dot plot of top 20 biological process GO terms based on differential expressed genes with a false discovery rate of q-value < 0.05 between the (B) knockout versus wild-type and rescue groups, and (C) the rescue versus the wild-type group. GO terms were sorted by gene ratio with size representing total counts and color representing q-value.

Compensatory upregulation of anti-inflammatory markers such as Il33, Il10, Il19, and Cxcl10 was also observed, which are commonly occuring in cases of pathological tissue remodeling and foreign body responses[196, 197]. Pairwise analysis showed similar pro-inflammatory differential response profile between knockout with either wild-type or rescue expression. As expected, mast cell marker, Fcer1a, was decreased compared to mast cell containing models (Figure 3.15, Table 3.2, 3.3).

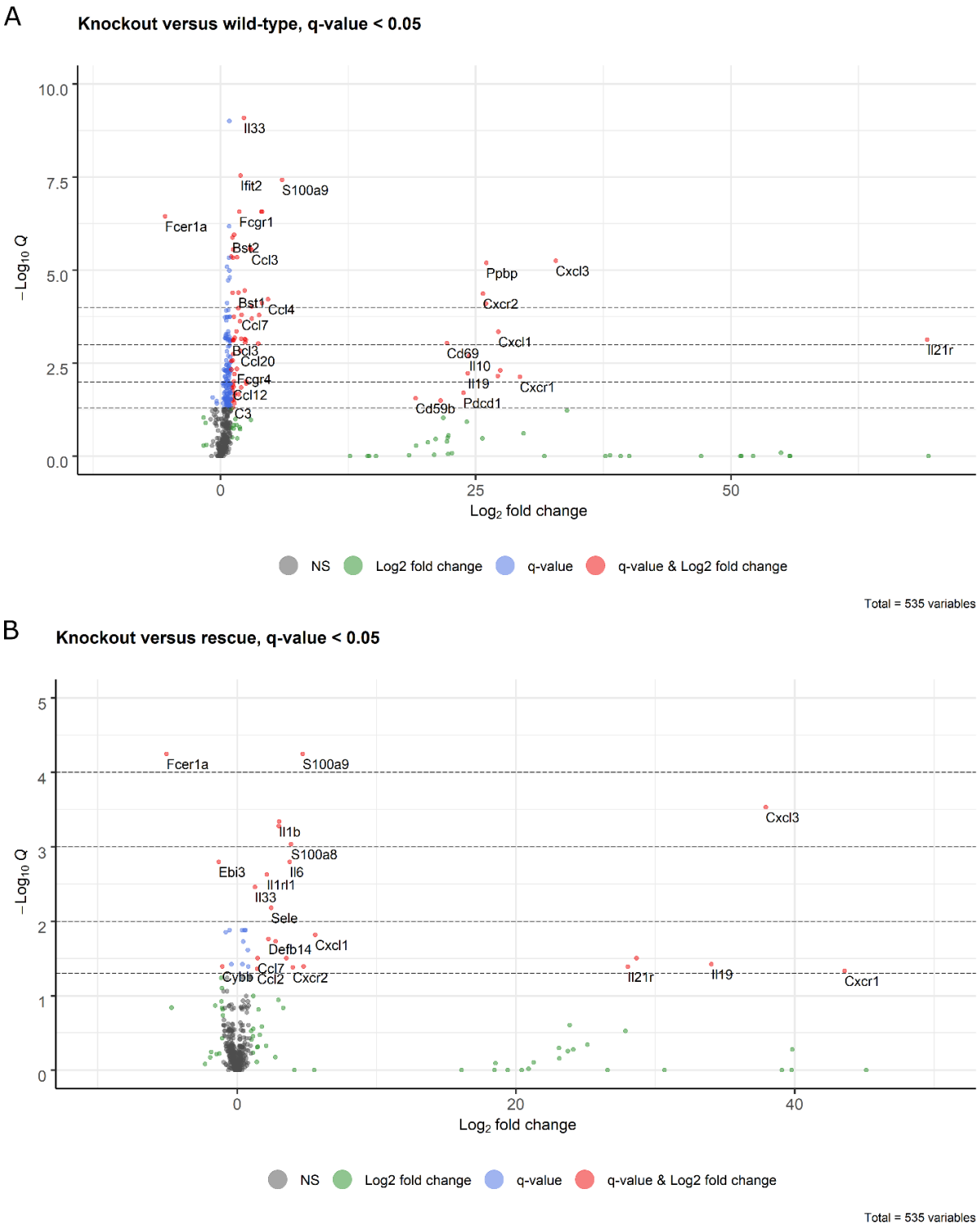

Figure 3.15: Volcano plots of pairwise comparisons for knockout response. Differential expression between knockout versus (A) wild-type and (B) rescue sample groups with dots indicating false discovery rate less than 0.05 (blue, red), absolute fold change greater than 1.5 (green, red) or non-significant (black). Dashed lines indicating different significance thresholds (*q < 0.05, **q < 0.01, ***q < 0.001 and ****q < 0.0001).

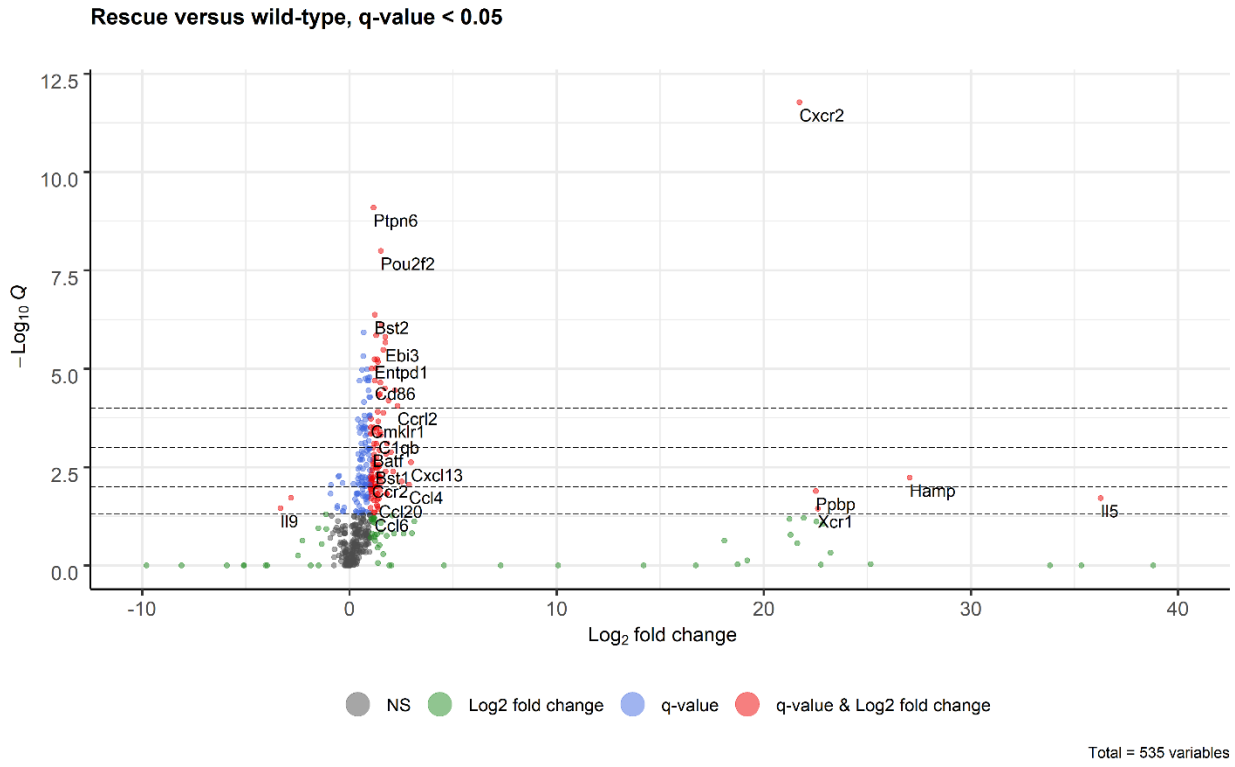

Figure 3.16: Volcano plot of pairwise comparison between rescue and wild-type sample. Differential expression of rescue sample versus wild-type with dots indicating false discovery rate less than 0.05 (blue, red), absolute fold change greater than 1.5 (green, red) or non-significant (black). Dashed lines indicating different significance thresholds (*q < 0.05, **q < 0.01, ***q < 0.001 and ****q < 0.0001).

Notably, differential expression of genes between the rescue and wild-type samples lacked several pro-inflammatory markers particularly associated with the IL1 cytokine family and mainly consisted of cellular processes, cell cycle, and migration markers (Figure 3.16, Table 3.4).

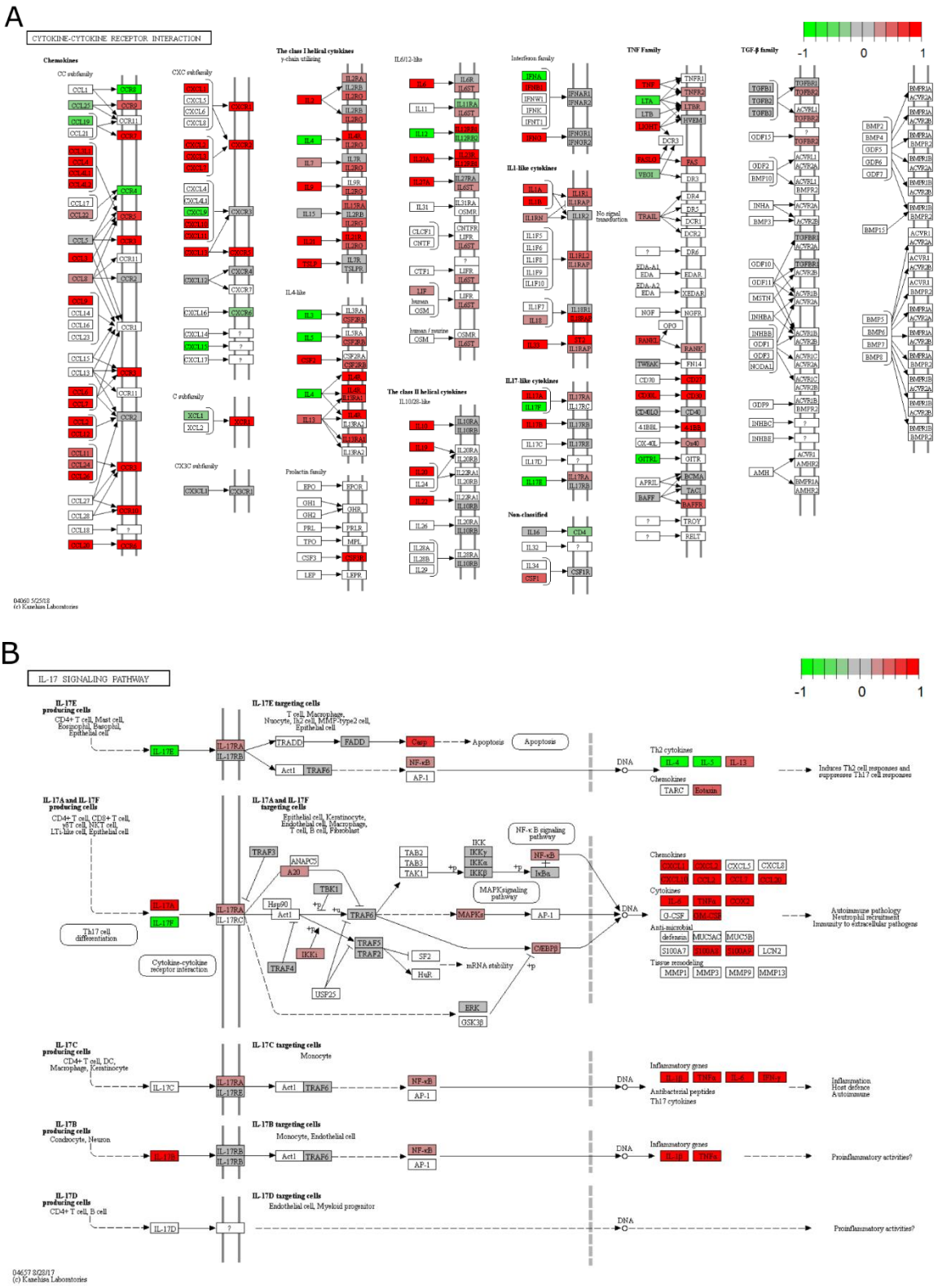

Figure 3.17: Pathview of KEGG Gene Enrichment Analysis. Top 3 relevant enriched KEGG pathways. (A) Cytokine-cytokine receptor interaction: mmu04060. (B) IL-17 signaling pathway: mmu04657. (C) TNF signaling pathway: mmu04668.

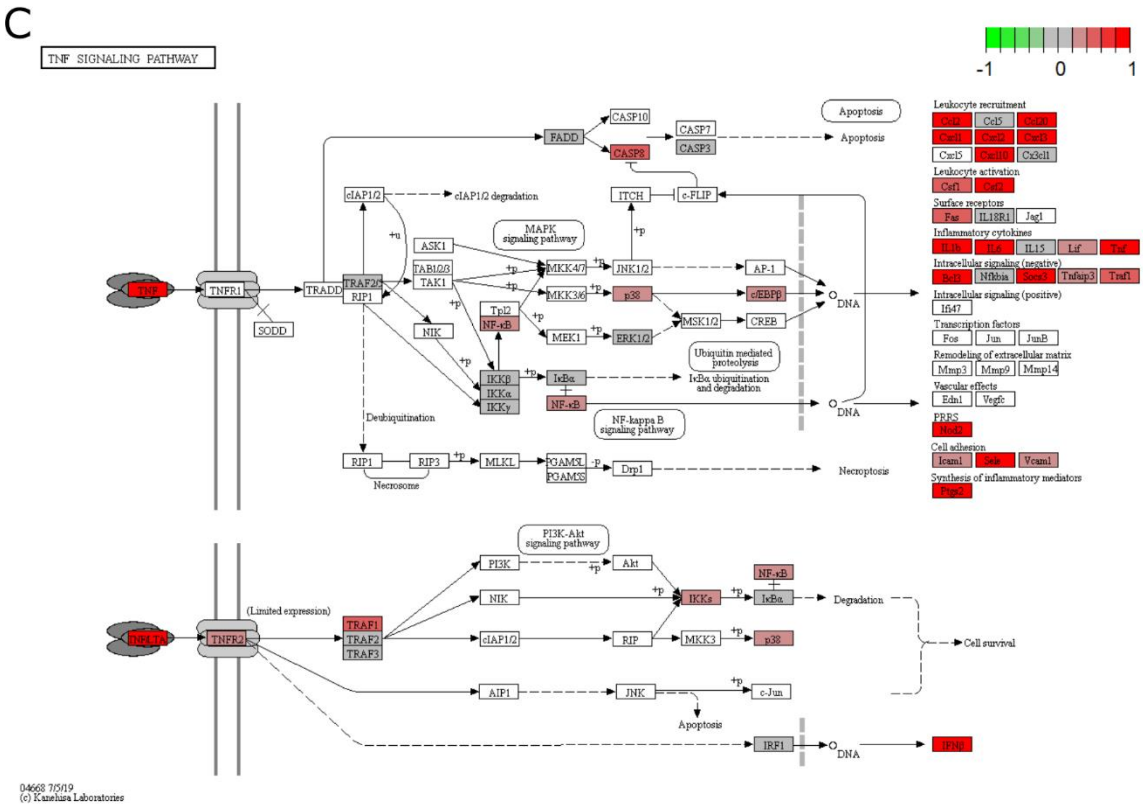

Figure 3.17: Pathview of KEGG Gene Enrichment. (continued)

Gene enrichment analysis between the knockout versus the wild-type and rescue response through KEGG pathway analysis highlighted several pro-inflammatory pathways such as TNF, IL-17, and NF-κB, and cellular stress pathways such a necroptosis and apoptosis (Figure 3.17, Table 3.5). Enrichment analysis through the top 20 GO terms similarly supported lack of transition from a pro-inflammatory to pro-remodeling response in the knockout with enrichment of pathways related to neutrophils, inflammatory responses and pro-inflammatory cytokines such as IL-6 and IL-1 (Figure 3.14B, Table 3.6). In comparison, GO term analysis between the rescue versus wildtype response lacked these enriched inflammatory pathways instead highlighting pathways related to general immune cell proliferation, activation, regulation, and adhesion. Ultimately, this comprehensive gene expression profiling demonstrated that mast cells play a role in the immunomodulatory transition from a pro-inflammatory to pro-

remodeling response and support enhanced regulation of immune cellular processes for ECM based biomaterial scaffolds.

This study demonstrated that mast cells contribute to the dynamic immunomodulatory response to pro-regenerative biomaterial scaffolds. Therapeutics targeting regulatory immune cell populations such as T cells have allowed for the creation and advancement of various immuno- and biomaterial therapies. Our work suggests that attention and targeting to the immunoregulatory effects of mast cells could translate to further synergistic coordination of tissue remodeling responses for improved tissue regeneration therapies.

Table 3.1: Differential expression fold change and statistics of knockout to other groups for genes with false discovery rate < 0.05

Gene	logFC	pvalue	qvalue
Bcl3	0.96	1.05E-04	1.34E-03
Bst1	1.12	1.91E-04	2.18E-03
Bst2	0.54	2.00E-03	1.69E-02
Casp8	0.42	6.35E-05	9.15E-04
Ccl2	1.90	1.15E-06	3.14E-05
Ccl20	1.24	3.55E-03	2.59E-02
Ccl3	2.00	3.42E-06	7.78E-05
Ccl4	3.21	8.32E-06	1.69E-04
Ccl7	1.76	2.57E-06	6.39E-05
Cd24a	0.61	3.48E-03	2.57E-02
Cd44	0.49	9.75E-05	1.27E-03
Cd69	12.56	5.91E-05	8.74E-04
Cd80	0.72	5.34E-04	5.61E-03
Cd82	-0.39	3.22E-03	2.48E-02
Cebpb	0.35	6.05E-03	4.14E-02
Cfb	0.72	1.31E-04	1.60E-03
Clec4e	2.65	2.43E-04	2.66E-03
Csf3r	0.81	9.62E-04	8.92E-03
Cxcl1	16.41	0.00E+00	0.00E+00
Cxcl10	1.45	5.63E-03	3.90E-02
Cxcl3	35.38	5.86E-12	6.72E-10
Cxcr1	36.44	7.95E-04	7.76E-03
Cxcr2	14.84	1.02E-07	4.00E-06
Ddx58	0.52	6.51E-07	2.09E-05
Defb14	2.65	3.60E-07	1.23E-05
Ets1	0.36	2.61E-03	2.13E-02
Fcer1a	-5.26	5.77E-09	3.15E-07
Fcgr1	0.97	1.38E-04	1.64E-03
Hamp	13.87	6.40E-03	4.32E-02
Hif1a	0.49	6.30E-04	6.27E-03
Ifi204	0.89	3.68E-04	3.94E-03
Ifi35	0.53	1.98E-05	3.73E-04
Ifih1	0.42	3.28E-03	2.50E-02
Ifit2	1.21	1.08E-06	3.12E-05
Ifitm1	1.53	2.19E-05	4.00E-04
Il10	12.91	6.13E-04	6.21E-03
Il13ra1	0.72	1.15E-05	2.25E-04
Il15ra	0.55	5.56E-03	3.90E-02
Il19	29.11	0.00E+00	0.00E+00
Il1a	0.78	1.65E-03	1.51E-02
Il1b	3.50	6.56E-12	6.72E-10
Il1r1	0.44	2.80E-05	4.79E-04
Il1rl1	2.50	1.49E-09	1.02E-07
Il1rl2	0.50	6.40E-06	1.35E-04
Il1rn	0.38	3.74E-06	8.18E-05
Il21r	48.62	1.35E-06	3.52E-05
Il23a	27.90	2.75E-06	6.54E-05
Il33	1.78	8.66E-12	6.76E-10
Il4ra	1.05	8.11E-08	3.41E-06
Il6	3.76	1.84E-08	8.37E-07
Irak4	0.40	7.49E-03	5.00E-02
Irf7	1.07	5.74E-04	5.92E-03
Irgm1	0.56	3.78E-03	2.72E-02
Itga5	0.74	1.71E-04	1.99E-03
Itga6	0.70	4.89E-05	7.44E-04
Itgb1	0.32	3.89E-03	2.76E-02
Ltb4r1	0.63	1.87E-03	1.63E-02
Ltb4r2	0.88	3.28E-05	5.44E-04
Masp1	1.08	4.36E-05	6.82E-04
Muc1	2.38	6.79E-05	9.46E-04
Mx1	0.70	3.42E-03	2.57E-02
Myd88	0.52	6.92E-05	9.46E-04
Nfkb2	0.45	1.14E-04	1.41E-03
Nfkbiz	0.51	9.03E-04	8.66E-03
Nod2	0.85	3.06E-03	2.39E-02
Pdcd1	25.82	3.02E-03	2.39E-02
Pecam1	0.53	2.15E-03	1.78E-02
Plaur	0.86	1.93E-03	1.65E-02
Pml	0.37	2.91E-03	2.34E-02
Ppbp	14.78	1.14E-08	5.65E-07
Ptgs2	3.53	7.37E-12	6.72E-10
S100a8	3.96	3.41E-09	2.07E-07
S100a9	5.37	0.00E+00	0.00E+00
Sele	2.45	1.05E-06	3.12E-05
Sell	1.76	2.12E-04	2.37E-03
Socs3	1.10	8.46E-05	1.13E-03
Stat2	0.82	1.88E-03	1.63E-02
Stat3	0.51	3.53E-05	5.68E-04
Thy1	0.44	9.29E-04	8.77E-03
Tnf	2.29	2.28E-05	4.02E-04
Trem1	15.38	1.39E-07	5.07E-06
Tslp	1.50	1.82E-03	1.63E-02

Table 3.2: Differential expression fold change and statistics of knockout to wild-type for genes with false discovery rate < 0.05

Gene	logFC	pvalue	qvalue
Ahr	0.56	1.60E-02	4.34E-02
Arhgdib	0.74	7.20E-04	4.23E-03
B2m	0.73	1.61E-04	1.14E-03
Batf	0.98	9.85E-04	5.15E-03
Bcap31	0.19	2.52E-03	1.10E-02
Bcl3	1.16	9.73E-05	7.80E-04
Bcl6	0.43	7.65E-03	2.60E-02
Bid	0.60	2.23E-04	1.55E-03
Bst1	1.75	1.98E-06	4.00E-05
Bst2	1.15	2.91E-08	1.32E-06
Btk	0.78	1.47E-02	4.12E-02
C1qa	0.83	1.28E-02	3.72E-02
C1ra	0.67	7.83E-03	2.63E-02
C1s	0.65	1.10E-02	3.32E-02
C3	1.36	1.32E-02	3.79E-02
Card9	0.84	5.36E-04	3.29E-03
Casp1	0.47	7.29E-05	6.76E-04
Casp3	0.25	1.31E-02	3.78E-02
Casp8	0.63	3.29E-07	8.17E-06
Ccl12	1.19	2.89E-03	1.20E-02
Ccl2	2.36	1.68E-06	3.54E-05
Ccl20	1.95	2.15E-04	1.50E-03
Ccl3	3.00	7.70E-08	2.81E-06
Ccl4	4.65	3.34E-06	6.08E-05
Ccl6	1.43	5.82E-03	2.08E-02
Ccl7	2.06	1.11E-05	1.60E-04
Ccl9	1.31	9.73E-03	3.06E-02
Ccr5	1.11	1.06E-02	3.22E-02
Ccrl2	2.02	7.69E-05	7.01E-04
Cd109	0.44	4.95E-03	1.87E-02
Cd14	1.54	3.94E-05	4.40E-04
Cd244	1.04	2.35E-03	1.05E-02
Cd274	0.91	7.62E-03	2.60E-02
Cd44	0.45	2.35E-03	1.05E-02
Cd53	1.11	9.79E-03	3.06E-02
Cd59b	19.10	8.29E-03	2.77E-02
Cd69	22.16	1.25E-04	9.24E-04
Cd80	1.18	2.08E-06	4.05E-05
Cd86	0.73	2.97E-03	1.22E-02
Cd97	0.73	1.04E-02	3.20E-02
Ceacam1	0.68	9.96E-03	3.09E-02
Cfb	1.21	7.26E-08	2.81E-06
Cfh	0.81	1.40E-02	3.95E-02
Cfp	1.08	3.74E-03	1.45E-02
Clec4a4	21.55	1.04E-02	3.20E-02
Clec4e	3.69	1.29E-04	9.38E-04
Clec5a	0.89	5.71E-03	2.07E-02
Cmklr1	0.65	6.06E-03	2.14E-02
Csf1	0.90	1.31E-05	1.78E-04
Csf2rb	0.99	2.62E-03	1.11E-02
Csf3r	1.29	1.34E-05	1.78E-04
Ctnnb1	-0.38	1.34E-02	3.83E-02
Ctsc	0.34	1.84E-02	4.94E-02
Cxcl1	27.22	4.22E-05	4.53E-04
Cxcl10	1.77	6.25E-03	2.19E-02
Cxcl13	2.49	2.60E-03	1.11E-02
Cxcl3	32.83	2.04E-07	5.58E-06
Cxcr1	29.30	1.55E-03	7.43E-03
Cxcr2	25.70	2.29E-06	4.31E-05
Ddx58	0.85	5.37E-12	9.80E-10
Defb14	3.05	5.83E-06	9.38E-05
Entpd1	0.87	1.47E-04	1.06E-03
Ets1	0.55	6.90E-05	6.62E-04
Fas	0.79	6.38E-04	3.80E-03
Fasl	1.20	1.86E-02	4.97E-02
Fcer1a	-5.44	5.91E-09	3.59E-07
Fcer1g	0.95	2.60E-03	1.11E-02
Fcgr1	1.83	3.94E-09	2.69E-07
Fcgr4	1.57	7.88E-04	4.53E-03
Gm10499	0.75	3.07E-04	2.02E-03
H2-K1	0.54	4.22E-04	2.68E-03
H2-Q10	2.49	2.15E-03	9.82E-03
Hamp	27.39	9.20E-04	4.99E-03
Icam1	0.58	8.70E-04	4.81E-03
Ifi204	1.61	1.40E-07	4.50E-06
Ifi35	0.84	1.20E-08	6.59E-07
Ifih1	0.85	4.35E-07	1.03E-05
Ifit2	1.96	2.10E-10	2.87E-08
Ifitm1	1.89	2.10E-05	2.39E-04
Ifnar1	0.29	3.13E-03	1.28E-02
Ifnar2	0.66	2.11E-03	9.70E-03
Ifngr1	0.73	8.91E-03	2.87E-02

Table 3.2: Differential expression fold change and statistics of knockout to wild-type for genes with false discovery rate < 0.05 (continued)

Gene	logFC	pvalue	qvalue
Ikbke	0.74	7.97E-05	7.03E-04
Ikzf1	0.98	8.76E-03	2.85E-02
Il10	24.33	3.06E-04	2.02E-03
Il10ra	0.72	1.78E-02	4.80E-02
Il10rb	0.63	1.24E-02	3.63E-02
Il13ra1	1.03	1.27E-07	4.35E-06
Il15ra	0.91	1.10E-04	8.33E-04
Il16	0.61	1.52E-02	4.21E-02
Il17ra	0.49	9.50E-04	5.10E-03
Il18	0.54	1.21E-02	3.59E-02
Il18rap	1.36	6.65E-03	2.32E-02
Il19	24.21	1.15E-03	5.90E-03
Il1a	0.88	2.85E-03	1.19E-02
Il1b	3.98	3.93E-09	2.69E-07
Il1r1	0.50	5.79E-05	5.86E-04
Il1rl1	2.88	6.36E-08	2.67E-06
Il1rl2	0.55	1.95E-05	2.26E-04
Il1rn	0.42	1.54E-05	1.87E-04
Il21r	69.22	8.58E-05	7.34E-04
Il23a	27.15	1.45E-03	7.02E-03
Il2rg	0.89	1.19E-03	6.00E-03
Il33	2.28	2.98E-12	8.16E-10
Il4ra	1.32	2.25E-08	1.12E-06
Il6	3.76	1.15E-05	1.61E-04
Il6ra	0.70	1.06E-02	3.22E-02
Il6st	0.43	9.36E-03	2.98E-02
Irak2	0.54	8.28E-06	1.22E-04
Irak3	0.68	1.17E-03	5.93E-03
Irak4	0.71	4.96E-05	5.22E-04
Irf5	0.66	7.32E-03	2.52E-02
Irf7	1.72	6.80E-06	1.06E-04
Irf8	0.87	5.14E-03	1.93E-02
Irgm1	1.20	1.61E-07	4.63E-06
Itga4	0.81	9.81E-04	5.15E-03
Itga5	0.91	1.01E-04	7.81E-04
Itga6	0.89	1.42E-05	1.80E-04
Itgal	0.79	1.35E-03	6.65E-03
Itgam	1.16	4.41E-03	1.70E-02
Itgb1	0.53	5.10E-05	5.26E-04
Jak1	0.66	1.43E-05	1.80E-04
Jak2	0.45	1.60E-03	7.60E-03
Jak3	0.65	1.07E-02	3.23E-02
Kit	-4.96	0.00E+00	0.00E+00
Lcp2	1.33	1.26E-03	6.27E-03
Lilrb3	1.14	2.31E-04	1.58E-03
Lilrb4	1.03	5.76E-03	2.07E-02
Litaf	0.52	6.96E-03	2.41E-02
Ltb4r1	0.80	8.30E-04	4.68E-03
Ltb4r2	0.97	1.01E-04	7.81E-04
Ltbr	0.32	8.39E-04	4.68E-03
Ly96	0.72	4.08E-05	4.46E-04
Masp1	1.25	9.03E-05	7.50E-04
Msr1	1.30	2.17E-03	9.82E-03
Muc1	2.01	3.60E-03	1.43E-02
Mx1	0.99	4.70E-04	2.92E-03
Myd88	0.82	1.54E-07	4.63E-06
Ncf4	0.87	1.52E-02	4.21E-02
Nfatc1	0.71	9.50E-05	7.76E-04
Nfatc2	0.55	3.68E-03	1.44E-02
Nfkb1	0.44	7.17E-05	6.76E-04
Nfkb2	0.64	4.40E-06	7.68E-05
Nfkbia	0.55	4.76E-03	1.81E-02
Nfkbiz	0.90	6.90E-07	1.57E-05
Nod2	1.39	6.75E-05	6.60E-04
Nox4	0.99	5.66E-03	2.07E-02
Pdcd1	23.80	5.39E-03	1.99E-02
Pecam1	0.67	1.08E-03	5.55E-03
Plau	0.73	1.48E-02	4.13E-02
Plaur	1.18	4.15E-04	2.67E-03
Pml	0.63	1.45E-05	1.80E-04
Pou2f2	0.71	2.04E-03	9.44E-03
Ppbp	26.04	2.45E-07	6.37E-06
Psmb10	0.76	2.42E-03	1.07E-02
Psmb9	0.62	8.40E-03	2.77E-02
Ptafr	0.91	4.43E-03	1.70E-02
Ptger4	-0.39	1.11E-02	3.32E-02
Ptgs2	4.07	3.16E-09	2.69E-07
Ptpn22	0.99	9.42E-03	2.98E-02
Ptpn6	0.74	7.75E-06	1.18E-04
Ptprc	0.78	1.57E-02	4.31E-02
Rela	0.35	2.69E-03	1.13E-02
Relb	0.51	2.52E-03	1.10E-02

Table 3.2: Differential expression fold change and statistics of knockout to wild-type for genes with false discovery rate < 0.05 (continued)

Gene	logFC	pvalue	qvalue
S100a8	4.05	4.49E-06	7.68E-05
S100a9	6.03	3.42E-10	3.74E-08
Sele	2.47	9.05E-05	7.50E-04
Sell	2.37	8.24E-05	7.16E-04
Smad3	0.29	8.62E-03	2.82E-02
Socs3	1.23	2.70E-04	1.82E-03
Stat1	0.88	6.39E-05	6.35E-04
Stat2	1.23	9.84E-05	7.80E-04
Stat3	0.72	8.62E-07	1.89E-05
Stat5a	0.56	1.81E-03	8.47E-03
Stat6	0.40	9.21E-04	4.99E-03
Syk	0.85	3.45E-03	1.38E-02
Tap1	0.62	5.64E-04	3.43E-03
Tapbp	0.49	3.38E-03	1.37E-02
Tbk1	0.37	8.38E-03	2.77E-02
Tcf7	-0.78	7.83E-03	2.63E-02
Tgfb1	0.55	8.84E-03	2.86E-02
Tgfbi	0.92	7.51E-04	4.37E-03
Tgfbr2	0.72	3.68E-03	1.44E-02
Thy1	0.52	9.89E-04	5.15E-03
Tirap	0.44	1.45E-03	7.02E-03
Tlr1	1.06	8.29E-04	4.68E-03
Tlr2	1.05	4.41E-04	2.77E-03
Tlr3	0.46	9.21E-03	2.95E-02
Tlr4	0.90	5.19E-03	1.93E-02
Tlr5	0.67	6.00E-03	2.13E-02
Tlr8	0.98	1.58E-02	4.31E-02
Tlr9	0.84	1.68E-03	7.90E-03
Tmem173	0.58	1.38E-02	3.92E-02
Tnf	3.05	1.69E-05	2.01E-04
Tnfaip3	0.70	7.83E-05	7.02E-04
Tnfrsf11a	0.94	3.33E-04	2.17E-03
Tnfrsf14	0.64	1.36E-02	3.87E-02
Tnfrsf1b	0.82	1.60E-02	4.34E-02
Tnfrsf4	0.57	5.95E-04	3.58E-03
Tnfsf14	1.25	3.40E-03	1.37E-02
Trem1	26.00	4.78E-06	7.92E-05
Tslp	2.40	1.18E-04	8.83E-04
Vcam1	0.82	1.23E-02	3.61E-02
Xbp1	0.34	5.53E-03	2.03E-02
Zeb1	0.55	1.13E-02	3.35E-02

Table 3.3: Differential expression fold change and statistics of knockout to rescue for genes with false discovery rate < 0.05

Gene	logFC	pvalue	qvalue
Ccl2	1.44	2.62E-03	4.34E-02
Ccl7	1.47	1.37E-03	3.13E-02
Cd44	0.53	3.45E-04	1.31E-02
Cd82	-0.54	3.53E-04	1.31E-02
Cxcl1	5.59	4.72E-04	1.52E-02
Cxcl3	37.92	1.61E-06	2.93E-04
Cxcr1	43.57	2.87E-03	4.62E-02
Cxcr2	3.98	2.43E-03	4.16E-02
Cybb	-1.07	2.20E-03	4.05E-02
Defb14	2.24	5.68E-04	1.73E-02
Ebi3	-1.32	2.32E-05	1.59E-03
Fcer1a	-5.07	2.06E-07	5.65E-05
Hif1a	0.60	3.43E-04	1.31E-02
Il19	34.01	1.73E-03	3.77E-02
Il1b	3.01	3.34E-06	4.57E-04
Il1r1	0.39	1.86E-03	3.77E-02
Il1rl1	2.12	3.88E-05	2.36E-03
Il1rl2	0.44	6.85E-04	1.87E-02
Il1rn	0.35	3.60E-04	1.31E-02
Il21r	28.01	2.30E-03	4.07E-02
Il23a	28.64	1.37E-03	3.13E-02
Il33	1.27	6.34E-05	3.47E-03
Il4ra	0.77	9.36E-04	2.44E-02
Il6	3.76	2.22E-05	1.59E-03
Ltb4r2	0.80	2.22E-03	4.05E-02
Muc1	2.75	6.46E-04	1.86E-02
Pou2f2	-0.81	4.09E-04	1.40E-02
Ppbp	3.53	1.36E-03	3.13E-02
Ptgs2	2.99	4.81E-06	5.26E-04
S100a8	3.87	1.01E-05	9.17E-04
S100a9	4.71	1.81E-07	5.65E-05
Sele	2.43	1.33E-04	6.61E-03
Tgfbr1	-0.41	1.85E-03	3.77E-02
Trem1	4.76	2.16E-03	4.05E-02

Table 3.4: Differential expression fold change and statistics of rescue to wild-type for genes with false discovery rate < 0.05

Gene	logFC	pvalue	qvalue
Ahr	0.75	1.35E-03	5.74E-03
Arhgdib	0.96	1.29E-05	1.64E-04
B2m	0.97	6.04E-07	1.65E-05
Batf	1.14	1.45E-04	1.02E-03
Bcap31	0.20	2.27E-03	8.40E-03
Bcl6	0.71	1.19E-05	1.55E-04
Bid	0.60	2.87E-04	1.69E-03
Blnk	0.84	1.87E-04	1.22E-03
Bst1	1.26	5.37E-04	2.77E-03
Bst2	1.22	3.87E-09	4.23E-07
Btk	1.06	1.04E-03	4.76E-03
C1qa	1.30	1.11E-04	8.01E-04
C1qb	1.40	5.74E-05	4.69E-04
C1ra	0.80	1.62E-03	6.43E-03
C1s	0.96	1.98E-04	1.26E-03
C2	0.77	6.26E-03	1.81E-02
Card9	0.93	1.58E-04	1.06E-03
Casp1	0.61	3.68E-07	1.06E-05
Casp8	0.42	7.14E-04	3.49E-03
Ccbp2	1.95	3.41E-04	1.94E-03
Ccl12	0.94	1.90E-02	4.60E-02
Ccl20	1.42	7.00E-03	1.98E-02
Ccl3	2.00	2.09E-04	1.31E-03
Ccl4	2.87	2.44E-03	8.76E-03
Ccl6	1.21	1.82E-02	4.47E-02
Ccr2	1.08	1.52E-03	6.13E-03
Ccrl1	0.75	8.54E-03	2.32E-02
Ccrl2	2.33	5.85E-06	8.65E-05
Cd109	0.47	2.58E-03	8.89E-03
Cd14	1.50	6.01E-05	4.83E-04
Cd22	0.93	4.89E-03	1.49E-02
Cd244	0.90	8.51E-03	2.32E-02
Cd274	1.04	2.47E-03	8.76E-03
Cd36	1.03	3.49E-03	1.13E-02
Cd4	0.81	1.74E-02	4.34E-02
Cd48	1.07	1.90E-03	7.33E-03
Cd74	1.32	4.82E-03	1.48E-02
Cd79b	1.77	2.37E-04	1.46E-03
Cd80	0.92	2.50E-04	1.50E-03
Cd81	0.37	4.81E-03	1.48E-02
Cd83	1.18	8.00E-03	2.20E-02
Cd86	1.23	8.76E-07	1.99E-05
Cd97	0.77	7.04E-03	1.98E-02
Ceacam1	0.64	1.85E-02	4.52E-02
Cfb	0.99	1.11E-05	1.52E-04
Cfd	1.34	7.71E-03	2.13E-02
Cfh	1.03	1.84E-03	7.17E-03
Cfp	1.07	4.07E-03	1.30E-02
Ciita	1.03	1.31E-02	3.41E-02
Clec5a	1.11	6.89E-04	3.39E-03
Cmklr1	1.03	1.50E-05	1.86E-04
Crlf2	1.13	4.18E-04	2.26E-03
Csf1	0.96	3.24E-06	5.21E-05
Csf1r	1.18	2.55E-04	1.52E-03
Csf2rb	0.90	6.23E-03	1.81E-02
Csf3r	0.96	1.29E-03	5.64E-03
Ctnnb1	-0.49	1.16E-03	5.19E-03
Ctsc	0.51	3.65E-04	2.04E-03
Ctss	1.53	2.09E-03	7.89E-03
Cul9	0.64	5.70E-03	1.68E-02
Cx3cr1	1.88	4.11E-06	6.42E-05
Cxcl12	0.66	3.60E-05	3.39E-04
Cxcl13	2.97	4.41E-04	2.36E-03
Cxcl9	1.79	4.95E-03	1.49E-02
Cxcr2	21.72	6.11E-15	1.67E-12
Cxcr3	0.86	6.54E-03	1.88E-02
Cxcr4	0.74	2.45E-03	8.76E-03
Cybb	1.70	1.61E-06	3.15E-05
Ddx58	0.66	1.05E-07	4.78E-06
Ebi3	1.74	3.90E-08	2.13E-06
Emr1	1.69	3.24E-05	3.20E-04
Entpd1	1.21	1.46E-07	5.72E-06
Ets1	0.39	5.17E-03	1.54E-02
Fas	0.66	4.75E-03	1.48E-02
Fcamr	-0.92	4.79E-03	1.48E-02
Fcer1g	1.32	3.25E-05	3.20E-04
Fcgr1	1.73	2.54E-08	1.54E-06
Fcgr2b	1.22	2.87E-03	9.62E-03
Fcgr3	1.41	5.37E-04	2.77E-03
Fcgr4	1.83	1.09E-04	7.97E-04
Fcgrt	0.95	1.62E-03	6.43E-03
Fkbp5	1.11	1.51E-03	6.13E-03

Table 3.4: Differential expression fold change and statistics of rescue to wild-type for genes with false discovery rate < 0.05 (continued)

Gene	logFC	pvalue	qvalue
Gm10499	0.86	5.42E-05	4.50E-04
Gpr183	1.03	2.58E-03	8.89E-03
H2-Aa	1.47	1.38E-03	5.75E-03
H2-Ab1	1.30	2.96E-03	9.80E-03
H2-DMa	1.42	1.34E-03	5.74E-03
H2-DMb2	1.35	1.22E-02	3.21E-02
H2-Eb1	1.25	5.70E-03	1.68E-02
H2-K1	0.77	7.08E-07	1.76E-05
H2-Q10	2.53	1.89E-03	7.32E-03
Hamp	27.04	1.41E-03	5.84E-03
Hcst	1.39	1.45E-02	3.71E-02
Hfe	0.91	6.13E-03	1.79E-02
Hlx	0.61	1.50E-02	3.83E-02
Icam1	0.56	1.44E-03	5.94E-03
Ifi204	1.42	2.72E-06	4.65E-05
Ifi35	0.61	3.27E-05	3.20E-04
Ifih1	0.86	3.38E-07	1.03E-05
Ifit2	1.49	1.11E-06	2.25E-05
Ifnar1	0.48	8.88E-07	1.99E-05
Ifnar2	1.00	3.23E-06	5.21E-05
Ifngr1	1.17	2.94E-05	3.10E-04
Ifngr2	0.58	1.08E-04	7.97E-04
Ikbke	0.93	9.59E-07	2.02E-05
Ikzf1	1.06	4.79E-03	1.48E-02
Ikzf2	0.90	2.49E-03	8.80E-03
Il10ra	1.36	8.63E-06	1.24E-04
Il10rb	1.03	5.22E-05	4.46E-04
Il13ra1	0.63	1.25E-03	5.50E-03
Il15	0.66	1.58E-02	4.02E-02
Il15ra	0.72	2.81E-03	9.49E-03
Il16	1.33	1.42E-07	5.72E-06
Il17ra	0.51	6.30E-04	3.19E-03
Il18r1	1.16	3.34E-04	1.93E-03
Il22ra2	2.10	8.72E-04	4.08E-03
Il2rg	0.83	2.43E-03	8.76E-03
Il33	1.02	1.35E-03	5.74E-03
Il4ra	0.55	1.90E-02	4.60E-02
Il5	36.27	6.81E-03	1.94E-02
Il6ra	1.12	4.91E-05	4.27E-04
Il7r	1.37	5.34E-03	1.59E-02
Il9	-3.34	1.35E-02	3.51E-02
Irak1	0.31	1.65E-02	4.17E-02
Irak2	0.69	1.52E-08	1.19E-06
Irak3	1.07	3.07E-07	9.86E-06
Irak4	0.62	3.73E-04	2.04E-03
Irf1	0.83	3.40E-05	3.26E-04
Irf5	1.03	2.80E-05	3.07E-04
Irf7	1.29	6.54E-04	3.28E-03
Irf8	1.48	2.48E-06	4.38E-05
Irgm1	1.29	2.06E-08	1.41E-06
Itga4	1.27	2.78E-07	9.49E-06
Itgal	0.95	1.52E-04	1.05E-03
Itgam	1.25	2.33E-03	8.54E-03
Itgb1	0.41	1.52E-03	6.13E-03
Itgb2	1.22	3.18E-03	1.05E-02
Jak1	0.70	4.63E-06	7.03E-05
Jak2	0.47	1.13E-03	5.13E-03
Kit	-5.72	0.00E+00	0.00E+00
Klrc1	1.32	1.08E-02	2.89E-02
Klrc2	-2.83	6.70E-03	1.92E-02
Klrk1	1.03	7.13E-03	2.00E-02
Lair1	1.52	1.33E-03	5.74E-03
Lcp2	1.43	5.96E-04	3.05E-03
Lilrb3	1.26	5.39E-05	4.50E-04
Lilrb4	1.49	8.73E-05	6.81E-04
Litaf	0.75	1.00E-04	7.62E-04
Ltb	1.00	2.76E-03	9.39E-03
Ly86	1.49	4.55E-05	4.08E-04
Ly96	0.87	9.10E-07	1.99E-05
Map4k1	1.19	1.82E-02	4.47E-02
Mapk14	0.34	4.93E-03	1.49E-02
Mapkapk2	0.41	1.59E-05	1.94E-04
Mbp	1.74	8.64E-04	4.08E-03
Msr1	1.40	1.01E-03	4.68E-03
Myd88	0.58	1.94E-04	1.25E-03
Ncf4	1.15	1.36E-03	5.74E-03
Nfatc1	0.68	2.23E-04	1.39E-03
Nfatc2	0.91	1.95E-06	3.57E-05
Nfkb1	0.46	2.94E-05	3.10E-04
Nfkb2	0.36	9.25E-03	2.49E-02
Nfkbia	0.78	6.36E-05	5.04E-04
Nfkbiz	0.78	1.66E-05	1.98E-04

Table 3.4: Differential expression fold change and statistics of rescue to wild-type for genes with false discovery rate < 0.05 (continued)

Gene	logFC	pvalue	qvalue
Nod2	1.07	2.76E-03	9.39E-03
Notch1	-0.59	1.15E-02	3.07E-02
Nox4	1.06	3.32E-03	1.09E-02
Pdcd2	-0.29	1.71E-02	4.28E-02
Pdgfb	0.61	1.92E-03	7.33E-03
Pml	0.52	3.58E-04	2.02E-03
Pou2f2	1.52	7.36E-11	1.01E-08
Pparg	0.82	5.33E-04	2.77E-03
Ppbp	22.51	4.02E-03	1.28E-02
Prdm1	-0.59	1.31E-02	3.41E-02
Prkcd	0.65	7.24E-04	3.50E-03
Psmb10	0.95	1.61E-04	1.07E-03
Psmb5	-0.26	1.28E-02	3.36E-02
Psmb9	0.93	8.84E-05	6.81E-04
Psmd7	-0.33	2.15E-03	8.01E-03
Ptafr	1.39	1.86E-05	2.16E-04
Ptpn22	1.44	1.77E-04	1.17E-03
Ptpn6	1.16	4.39E-12	8.00E-10
Ptprc	1.13	4.73E-04	2.51E-03
Rela	0.43	2.41E-04	1.47E-03
Relb	0.71	3.00E-05	3.10E-04
Rorc	0.79	7.35E-03	2.05E-02
Ski	0.36	1.74E-02	4.34E-02
Slamf7	1.63	9.36E-06	1.31E-04
Smad5	-0.33	1.63E-02	4.13E-02
Spn	1.36	6.69E-04	3.33E-03
Stat1	0.97	1.15E-05	1.53E-04
Stat2	0.83	9.20E-03	2.49E-02
Stat3	0.42	4.56E-03	1.44E-02
Stat5a	0.43	1.82E-02	4.47E-02
Stat5b	0.61	1.98E-03	7.52E-03
Stat6	0.49	4.78E-05	4.22E-04
Syk	0.98	7.92E-04	3.80E-03
Tagap	2.19	1.96E-06	3.57E-05
Tap1	0.90	6.48E-07	1.69E-05
Tapbp	0.70	3.66E-05	3.39E-04
Tbk1	0.44	2.15E-03	8.01E-03
Tcf7	-0.89	2.56E-03	8.89E-03
Tgfb1	0.81	1.36E-04	9.65E-04
Tgfbi	0.98	3.71E-04	2.04E-03
Tgfbr1	0.56	2.08E-05	2.37E-04
Tgfbr2	0.75	2.43E-03	8.76E-03
Tlr1	1.31	3.73E-05	3.40E-04
Tlr2	1.64	6.61E-08	3.29E-06
Tlr3	0.47	1.17E-02	3.10E-02
Tlr4	0.98	2.53E-03	8.86E-03
Tlr8	1.34	1.10E-03	5.02E-03
Tlr9	1.56	8.49E-09	7.74E-07
Tnfaip3	0.75	2.57E-05	2.87E-04
Tnfrsf11a	1.38	1.85E-07	6.74E-06
Tnfrsf13b	0.77	2.89E-03	9.65E-03
Tnfrsf14	0.99	1.56E-04	1.06E-03
Tnfrsf1b	1.07	1.67E-03	6.58E-03
Tnfsf12	1.20	1.06E-04	7.91E-04
Tollip	0.28	7.40E-03	2.05E-02
Trem2	1.48	3.77E-03	1.21E-02
Trp53	-0.53	1.22E-03	5.43E-03
Tslp	1.80	5.05E-03	1.52E-02
Tyrobp	1.31	3.03E-04	1.77E-03
Vcam1	1.10	8.05E-04	3.83E-03
Xcr1	22.61	1.39E-02	3.59E-02
Zeb1	0.64	3.57E-03	1.16E-02

Table 3.5: KEGG Gene Enrichment Analysis between knockout and other groups

ID	Description	GeneRatio	pvalue	qvalue
mmu04060	Cytokine-cytokine receptor interaction	29/76	9.56E-24	6.94E-22
mmu04657	IL-17 signaling pathway	14/76	2.42E-14	4.61E-13
mmu04668	TNF signaling pathway	15/76	2.54E-14	4.61E-13
mmu04640	Hematopoietic cell lineage	12/76	2.24E-11	2.71E-10
mmu04620	Toll-like receptor signaling pathway	11/76	6.7E-10	5.4E-09
mmu04630	JAK-STAT signaling pathway	13/76	1.25E-09	8.28E-09
mmu04064	NF-kappa B signaling pathway	11/76	2.1E-09	1.27E-08
mmu04625	C-type lectin receptor signaling pathway	11/76	2.55E-09	1.42E-08
mmu04621	NOD-like receptor signaling pathway	14/76	2.93E-09	1.52E-08
mmu04062	Chemokine signaling pathway	13/76	1.03E-08	4.4E-08
mmu04623	Cytosolic DNA-sensing pathway	7/76	1.16E-06	3.14E-06
mmu04659	Th17 cell differentiation	8/76	2.48E-06	6.44E-06
mmu04380	Osteoclast differentiation	8/76	1.35E-05	3.17E-05
mmu04622	RIG-I-like receptor signaling pathway	6/76	2.69E-05	5.92E-05
mmu04514	Cell adhesion molecules (CAMs)	7/76	0.00069	0.001253
mmu04217	Necroptosis	7/76	0.000714	0.001265
mmu04512	ECM-receptor interaction	4/76	0.007002	0.009971
mmu04010	MAPK signaling pathway	7/76	0.013414	0.018042
mmu04931	Insulin resistance	4/76	0.015038	0.019858

Table 3.6: Top 20 Biological Process GO Terms between knockout and other groups

ID	Description	GeneRatio	pvalue	qvalue
GO:1990266	neutrophil migration	26/78	4.32E-41	5.55E-38
GO:0050900	leukocyte migration	33/78	3.71E-40	2.38E-37
GO:0097530	granulocyte migration	26/78	1.49E-38	6.36E-36
GO:0097529	myeloid leukocyte migration	26/78	2.36E-34	7.58E-32
GO:0001819	positive regulation of cytokine production	31/78	6.29E-33	1.61E-30
GO:0030593	neutrophil chemotaxis	21/78	1E-32	2.14E-30
GO:0071621	granulocyte chemotaxis	21/78	1.15E-30	2.11E-28
GO:0019221	cytokine-mediated signaling pathway	26/78	1.48E-28	2.37E-26
GO:0032103	positive regulation of response to external stimulus	25/78	5.56E-28	7.94E-26
GO:0050727	regulation of inflammatory response	25/78	1.34E-26	1.72E-24
GO:0031349	positive regulation of defense response	25/78	4.07E-26	4.75E-24
GO:0030595	leukocyte chemotaxis	21/78	1.7E-25	1.82E-23
GO:0050729	positive regulation of inflammatory response	18/78	7.39E-24	7.3E-22
GO:0060326	cell chemotaxis	22/78	8.96E-24	8.21E-22
GO:0007159	leukocyte cell-cell adhesion	21/78	1.11E-21	9.48E-20
GO:0032635	interleukin-6 production	17/78	4.08E-21	3.27E-19
GO:0032675	regulation of interleukin-6 production	16/78	6.9E-20	5.21E-18
GO:0070555	response to interleukin-1	14/78	9.65E-20	6.88E-18
GO:0002685	regulation of leukocyte migration	17/78	1.72E-19	1.16E-17
GO:0042107	cytokine metabolic process	14/78	6.26E-18	4.02E-16

3.3 Materials and Methods

3.3.1 ECM Hydrogel Preparation

Myocardial matrix hydrogel was generated from porcine left ventricular tissue based on previously established protocols[130]. In brief, porcine left ventricular tissue was isolated and minced into small pieces. The tissue was decellularized under mechanical agitation in a solution of phosphate buffered saline (PBS) containing 1% (wt/vol) sodium dodecyl sulfate (SDS) (Fischer Scientific, Fair Lawn, NJ) with 0.5% 10,000 U/mL penicillin streptomycin (PS) (Gibco, Life Technologies, Grand Island, NY) until fully decellularized based on previously established criteria[130]. Once decellularized, the decellularized ECM was thoroughly rinsed to remove residual SDS, lyophilized, and milled into a fine powder. ECM powder was partially digested with 1 mg/mL pepsin in 0.1M HCL solution for 48 hours before solution was neutralized to pH of 7.4 and reconstituted to physiological salt concentrations. Partially digested ECM solution was aliquoted, lyophilized and stored at -80°C until re-suspending with sterile water prior to injection which self-assemble into hydrogels *in vivo*.

3.3.2 Mast Cell Knockout Mouse Model

Homozygous mast cell knockout mouse, w-sh mice: B6.Cg-*Kit*$^{W\text{-}sh}$/HNihrJaeBsmJ (Jackson Laboratory, Sacramento, CA) were breed in UCSD vivarium up to 10-13 weeks before being designated for subcutaneous procedures. Both male and female mice were utilized for investigation. Age matched wild-type C57BL6/J mice were used as control animals.

3.3.3 Bone Marrow Derived Differentiated Mast Cell Culture

Bone marrow derived cells were harvested from wild-type C57BL6/J mice that were euthanized by CO2 and cervical dislocation. Each femur was isolated and bone marrow was flushed with 10 mL of media, collected and pipetted into culture flasks incubated in cell culture

incubator at 37ºC and 5% CO_2. Mast cell differentiation media consisting of DMEM media (Gibco) with 10% FBS (Gibco), 1% penicillin streptomycin (Gibco), sterile filtered conditioned culture medium from D11 hybridoma cells as a source of IL3, 100 uM MEM nonessential amino acids (Lonza), 1mM sodium pyruvate (Gibco), 0.1 mM HEPES (Gibco), and 55 uM β-mercaptoethanol (Gibco). Non-adherent cells were passaged at day 3, 7, 10, 14, 18, 22 and 28 before differentiation of mast cells was assessed by flow cytometry with antibody markers for CD117 APC and FcεRI PE (Biolegend, San Diego, CA). Cells at greater than ~95% purity were utilized up to 4-6 weeks from initial isolation before mast cell functionality was expected to subside (Figure 3.18).

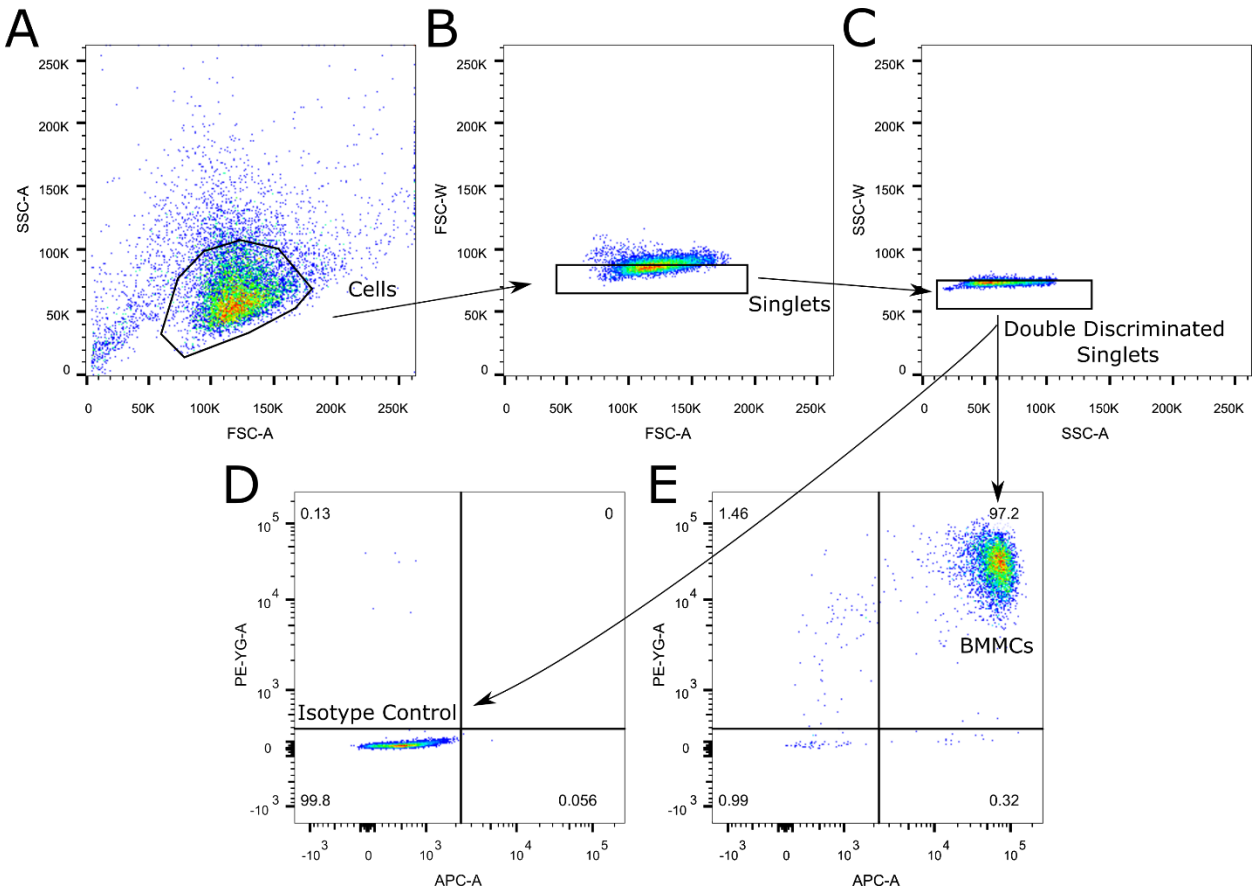

Figure 3.18: Gating for differentiation of bone marrow derived mast cells. Representative gating of bone marrow derived mast cells (BMMCs) for assessing purity at four to six weeks of differentiation protocol. (A) Cells and (B-C) double discrimination of singlets based on forward and side scatter. Quadrant gating cut-offs were set relative to (D) isotype control for (E) $CD117^{+}Fc\varepsilon RI^{+}$ mast cells.

For assessment of cell viability, 100,000 mast cells were plated into a 48 well plate (n = 4) with ECM hydrogel material at nongelling concentrations of 0.6 mg/mL or neutralized Collagen I, Rat Tail at concentrations of equivalent stiffness and collagen content of 0.25 mg/mL concentration[198] (Corning®, Corning, NY) doped into culture media. Media only culture was used as a control. AlamarBlue™ Cell Viability Reagent (Invitrogen, Waltham, MA) was added to each well at a tenth the volume totaling 400 µL solution, and cells were incubated in a 37ºC, 5% CO_2 cell culture incubator. At 0, 2, 4, and 8 hours after plate set-up, fluorescent plate

readings for alamarBlue signal at 560 nm excitation and 590 emission were read on a Synergy™ H4 multi-mode microplate reader and Gen5™ software (Biotek®. Wilnooski, VT). Experimental set-up was repeated to demonstrated relative reproducibility of the results.

3.3.4 Mast Cell Rescue Model Generation

For injection procedures, animals were briefly put under anesthesia at 2 % isoflurane on a nose cone and mice went placed upright to expose the dorsal region. The dorsal region was shaved and cleaned with 3 intervals of betadine and 70% ethanol. Mast cell reconstituted rescue mice were created by subcutaneous injections consisting of a total of 4 million bone marrow differentiated mast cells in DMEM in 100 µL volumes at evenly spaced intervals throughout the dorsal region of 4-6 week old knockout mice. Subsequent procedures were done in rescue mice at 10-13 weeks old. Age matched knockout mice were injected with DMEM alone at similar timepoints for comparative studies. For subsequent procedures, age matched knockout mice with DMEM injections and age matched wild-type mice were utilized as controls.

3.3.5 Biomaterial Injection and Harvesting

For biomaterial injections, animals were briefly put under anesthesia using 2% isoflurane on a nose cone and each mouse was injected with ECM hydrogel material receiving two evenly spaced 200 µL subcutaneous injections in the upper and lower dorsal region. At one, three, seven and eleven days post-injection, mice were euthanized by CO_2 and cervical dislocation. Timepoints were selected based on observation of consistent material retention and clear visibility up to these later timepoints. General dorsal skin tissue was cut and flipped to expose the underside to observe location and area of material injection. The injections, along with neighboring dermal tissue, were excised. Injections were divided into multiple parts with each

used for flow cytometry, staining or gene expression analysis as described below (n= 5-8 mice per group, 10-16 injections per group). Samples were collected across 2-3 batches of animals for demonstrating consistency of results.

3.3.6 Flow Cytometry

Excised subcutaneous injections were minced in ice-cold HBSS (Gibco) and enzymatically digested in a solution consisting of 1:1 solution of HBSS (calcium and magnesium supplemented) and 1% bovine serum albumin in PBS with 1 µM HEPES (Gibco), 300 U/mL collagenase type IV (Worthington Biochemical), 60 U/mL hyaluronidase (Sigma-Aldrich) and 10 U/mL DNase I (Sigma-Aldrich). Material in enzymatic digestion solution were incubated at 37ºC under mechanical agitation at 750 rpm on a thermomixer (Benchmark Scientific) for 40 minutes. Solutions were then kept in ice and FACs buffer consisting of 1% bovine serum albumin and 1mM EDTA in DPBS lacking calcium and magnesium added to inhibit further enzyme reaction. Digested tissue was filtered through a 100µm cell strainer. Cells were centrifuged at 400 rcf centrifugation at 4ºC and resuspended in HBSS. Cell suspension was stained with LIVE/DEAD™ Fixable Aqua (ThermoFisher Scientific) for 10 minutes at 4ºC and excess dye was quenched with FACs buffer. Cells were fixed and permeabilized by BD Cytofix/Cytoperm™ Buffer (BD Biosciences) for 10 minutes and washed in BD Perm/Wash™ Buffer (BD Biosciences). Cells were counted by hemocytometer and stained with antibody panels for immune cell subpopulations. General immune cell populations were stained with the following antibody panel: CD11c BV421 (Biolegend), F4/80 BUV395 (BD Biosciences), CD3 PerCp/Cy5.5 (Biolegend), CD117 APC (Biolegend), FcεRI PE (Biolegend), and CD19 APC-Cy7 (Biolegend). An antibody panel for macrophage and T cell polarization was also stained for consisting of: F4/80 BUV395 (BD Biosciences), CD86 BV786 (Biolegend), CD206 PE (Biolegend), CD3 PerCp/Cy5.5 (Biolegend), CD4 APC (Biolegend), CD8 Alexa Fluor 488 (Biolegend), and FoxP3

BV421 (Biolegend). Antibodies and IgG isotype controls were stained in BD Perm/Wash™ Buffer for 30 minutes at 4ºC before rinsing and resuspending in FACs buffer consisting of 1% bovine serum albumin and 1 mM EDTA in PBS for analysis. Stained cells were analyzed on a BD FACSCanto™ II and BD LSRFortessa™ X-20 (BD Biosciences). Gating was set based on positive, isotype and fluorescence minus one controls utilizing a mixed single cell suspension control sample derived from seven day post-injection biomaterial, isolated spleen cells, and four week differentiated mast cells to ensure all cells of interest were present in distinguishable amounts (Figure 3.19). Gating and flow data were processed in FlowJo (FlowJo LLC, Ashland, OR) (Figure 3.20).

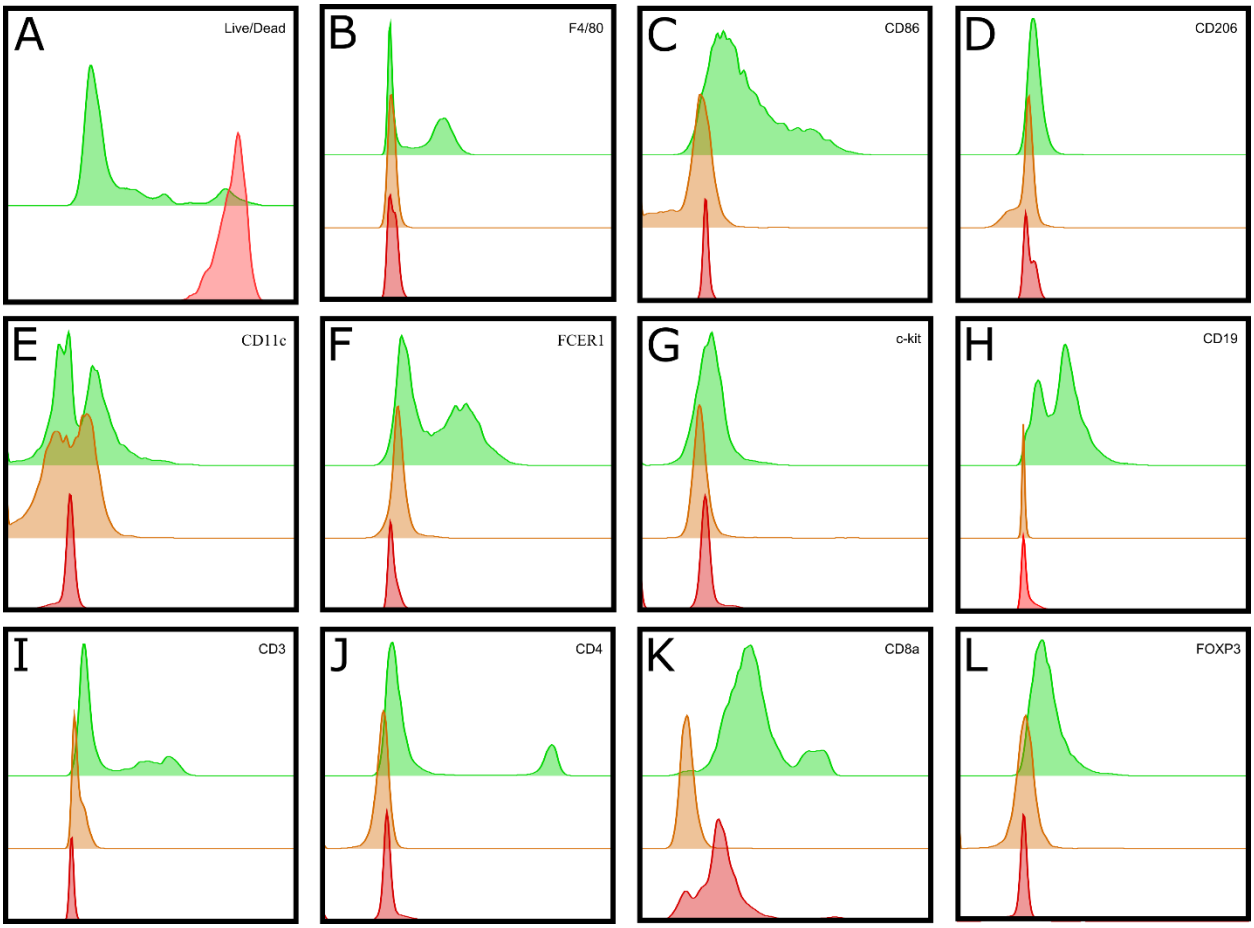

Figure 3.19: Gating controls for flow cytometry markers. (A) LIVE/DEAD™ Aqua thresholds utilized ethanol fixed sample as control (red) for determining live cell gating (green). (B-L) Gating for fluorescent antibody markers was set for positive signal (green) based on isotype (red) and fluorescence minus one controls (orange).

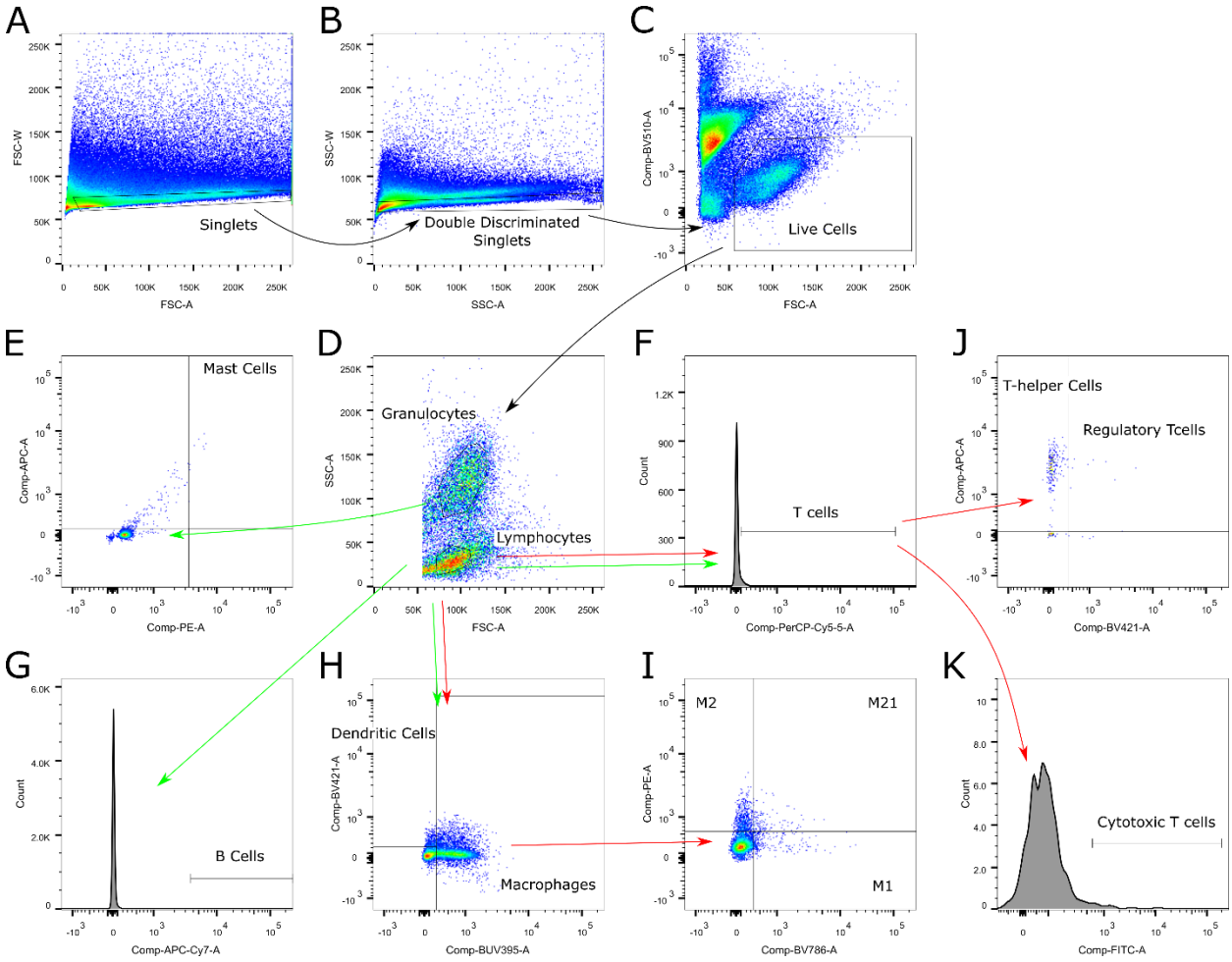

Figure 3.20: Gating Scheme for Flow Cytometry Analysis. Representative gating of single cell suspension isolated of subcutaneously injected ECM hydrogel. (A-B) General gating for both panels (black arrow) for double discrimination of singlets based on forward and side scatter. (C) Live cells were gated based on clustered from lack of stain uptake and forward scatter. (D) Granulocyte cluster based on forward and side scatter with (F) $CD117^{+}Fc\text{Ɛ}RI^{+}$ gated for mast cells. (E) Lymphocyte cluster based on forward and side scatter with (F) $CD3^{+}$ gated for T cells. Total cells based on forward and side scatter distribution were utilized to differentiate (G) B cells, (H) $CD11c^{+}F4/80^{-}$ dendritic cells, and $F4/80^{+}$ macrophages. For Panel 2 (red arrow), macrophages were further differentiated based on (I) M1 $CD86^{+}$ and M2 $CD206^{+}$ markers. T cells were further separated into (J) $CD4^{+}$ T-helper cells, $CD4^{+}FOXP3^{+}$ Regulatory T cells, and (K) $CD8^{+}$ cytotoxic T cells.

3.3.7 Quantitative Real-Time Polymerase Chain Reaction (qRT-PCR)

Flash frozen samples or tissue samples treated in RNAlater™ (Invitrogen) were homogenized with a mechanical rotator and then run through a RNeasy Mini kit (Qiagen, Germantown, MD) to extract RNA based on manufacturer instructions with an on-column DNase I digestion (Qiagen) for minimizing genomic DNA contamination. Superscript IV Reverse Transcriptase kit (Applied Biosystems, Foster City, MA) was used to synthesize cDNA with thermocycler settings of 65ºC for 5 minutes, 23ºC for 10 minutes, 55ºC for 10 minutes and 80ºC for 10 minutes. Eva Green Master Mix (Biotium, Fremont, CA) was used with custom-made forward and reverse primers (Table 3.7) at a final concentration of 0.2 µM for qPCR reactions. Samples were run in technical duplicate along with negative controls without template cDNA to confirm lack of contamination from qPCR reagents. PCR reactions were run on a CFX95™ Real-Time System (Bio-Rad, Hercules, CA) with the following thermal cycler settings: 30s at 50°C, 2 min at 95°C, 40 cycles of 10s at 95°C, and 30s at 55-65°C based on pre-determined optimal primer efficiency amplification temperature. After completing 40 cycles of PCR amplification, automated melting curve analysis, consisting of increasing the thermal cycler temperature from 50°C to 95°C at 5°C increments lasting 5s each, for confirming singular amplicon product in each reaction vessel. Bio-Rad CFX Manager™ 3.0 (Bio-Rad) was used for determining cycle threshold values from recorded signal based on a preset threshold.

Table 3.7: Primers for Pro-inflammatory versus Pro-remodeling Screen

Gene	Forward Primer			Reverse Primer		
Gapdh	5'	CATCAAGAAGGTGGTGAAGC	3'	5'	GTTGTCATACCAGGAAATGAGC	3'
Il1b	5'	TGCCACCTTTTGACAGTGATG	3'	5'	TGATGTGCTGCTGCGAGATT	3'
Il6	5'	TCCAGTTGCCTTCTTGGGAC	3'	5'	AGTCTCCTCTCCGGACTTGT	3'
Il17	5'	AAGCTGGACCACCACATGAA	3'	5'	CCCTGAAAGTGAAGGGGCAG	3'
Il36	5'	AGGGCAAACCAACTTTGCAG	3'	5'	GAAGTGGAGCCCTCTATGCC	3'
Il38	5'	TGCAGGAATGTGCTCCCTTC	3'	5'	GGTCTAGGCCTCGGTTAGGA	3'
Ccl1	5'	AGAAAGAGCTTCCCCTGAAGTTT	3'	5'	TGAGGCGCAGCTTTCTCTACC	3'
Ccl8	5'	CCCCTTCGGGTGCTGAAAAG	3'	5'	TCACTGACCCACTTCTGTGTG	3'
Ifng	5'	CGGCTGACTGAACTCAGATTG	3'	5'	CTGCAGCTCTGAATGTTTCTTAT	3'
Nos2	5'	CAGCTGGGCTGTACAAACCTT	3'	5'	CATTGGAAGTGAAGCGTTTCG	3'
Cd86	5'	GACTTGAACAACCAGACTCCTG	3'	5'	ATCAGCAAGACTGTCACAAAGA	3'
Vegf	5'	GCACATAGAGAGAATGAGCTTCC	3'	5'	CTCCGCTCTGAACAAGGCT	3'
Il1rn	5'	TCGGAGTACCTGTCATGCAAA	3'	5'	GCTTGCATCTTGCAGGGTCT	3'
Il4	5'	GAGACTCTTTCGGGCTTTTCG	3'	5'	CAGTGATGTGGACTTGGACTC	3'
Il13	5'	GAGCAACATCACACAAGACCAGA	3'	5'	GGCCAGGTCCACACTCCATA	3'
Il33	5'	TCCAACTCCAAGATTTCCCCG	3'	5'	CAGTGCAGTAGACATGGCAGAA	3'
Cd163	5'	GAGACACACGGAGCCATCAA	3'	5'	CGTTAGTGACAGCAGAGGCA	3'
Cd206	5'	GTGGACGCTCTAAGTGCCAT	3'	5'	GAATCTGACACCCAGCGGAA	3'
Arg1	5'	GAACACGGCAGTGGCTTTAAC	3'	5'	TGCTTAGTTCTGTCTGCTTTGC	3'

3.3.8 Nanostring Multiplex Gene Expression Analysis

For comprehensive evaluation of the whole immune profile, RNA samples were analyzed by Nanostring nCounter® MAX Analysis System with nCounter® Immunology Panel (Mouse) allowing for multiplexed assessment of 561 genes[199, 200]. Samples were processed according to manufacturer instructions. In brief, RNA sample concentrations were measured on a Qubit 3.0 Fluorometer with a Qubit™ RNA HS Assay kit. 70 µL of hybridization buffer was mixed with Immunology Panel Reporter CodeSet solution, and 8 µL of this master mix was mixed in a separate reaction vessel with 100 ng of RNA per tissue sample and RNA-free water up to 13 µL total. 2 µL of Capture ProbeSet was added to each vessel, mixed and placed on a thermocycler at 65ºC for 16-48 hours before being maintained at 4ºC for less than 24 hours. Nanostring nCounter Prep Station performed automated fluidic sample processing to purify and immobilize hybridized sample to cartridge surface. Digital barcode reads were analyzed by

Nanostring nCounter® Digital Analyzer. Results were analyzed by manufacturer nSolver™ Analysis Software 4.0 and custom R scripts. Gene expression normalization and differential expression was analyzed by the NanostringDiff package with significance at a false discovery rate of qvalue < 0.05[201, 202]. Gene enrichment analysis was performed with the clusterprofiler package[203] and volcano plots created with the EnhancedVolcano package[204] with a threshold at a false discovery rate of qvalue < 0.05.

3.3.9 Immunohistochemistry

Harvested samples were embedded into Tissue-Tel O.C.T. Compound (Sakura®, Torrance, CA) for cryosectioning. Cryosections from three different evenly spaced locations were used for all immunohistochemistry. Transverse sections were taken to obtain a cross-section of the biomaterial injection and neighboring dermal tissue. Histological evaluation of total cell and mast cell infiltration were taken from sections stained with Toluidine Blue Stain, 1% w/v (Ricca Chemical, Arlington, TX) and scanned with a Leica Aperio ScanScope® CS^2 (Leica, Buffalo Brove, IL) system. For fluorescent staining, slides were fixed with 4% paraformaldehyde in PBS (Thermo Scientific™) and blocked with a buffered solution containing 3% bovine serum albumin (Gemini Bio-Products, Inc., West Sacramento, CA)and 0.1% Triton X-100 (Sigma) in PBS. The primary antibodies, pan-macrophage marker anti-mouse F4/80 (eBioscience, San Diego, CA) and anti-mouse Ly-6G/Ly-6C (eBioscience), were incubated for 12-18 hours at 4°C: Secondary antibody Alexa Fluor 488 with Hoechst 33342 (Thermo Scientific™) counterstain was incubated for 30-40 minutes at room temperature. Coverslips were mounted with Fluoromount™ Aqueous Mounting Medium (Sigma) and allowed to dry protected from light. Fluorescent images were scanned with the Leica Ariol® DM6000B system (Leica). Cellular density and co-staining quantification were done with custom MATLAB scripts (Mathworks, Natick, MA).

3.3.10 Statistical Analysis

All data and plots are presented as mean ± SD unless noted otherwise. Statistics were performed in Prism 8 (GraphPad Software, San Diego, CA) or custom R scripts. For two group assessments, an unpaired student's *t*-test was performed while assessments across three or more groups was evaluated with a one-way ANOVA with a Tukey post-hoc with significance taken at $p < 0.05$. For analysis of differential expression of Nanostring data, a false discovery rate threshold of $q < 0.05$ was utilized.

3.4 Acknowledgements

The authors would like to thank Drs. Thomas Gilbert and Adam Young from ACell, Inc. for kindly providing the milled urinary bladder matrix. We would also like to acknowledge Dr. Elsa Molina, Director of the UC San Diego Stem Cell Genomics Core, for technical assistance of NanoString experiments, and Jesus Olvera and Cody Fine of the UC San Diego Human Embryonic Stem Cell Core Facility for technical assistance of flow cytometry experiments with all made possible in part by the CIRM Major Facilities grant (FA1-00607) to the Sanford Consortium for Regenerative Medicine. This work was supported by the NIH NHLBI (R01HL113468, R01HL146147). R.M.W. (F31HL137347). KLC is co-founder, consultant, board member, and holds equity interest in Ventrix, Inc.

Chapter 3, in part is currently being prepared for submission for publication of the material. Raymond M. Wang, Toshiaki Kawakami, Karen L. Christman. "Mast Cells Contribute to the Immunomodulatory Effect of the Biomaterial Microenvironment in a Gender Specific Manner**."** The dissertation author was a primary author of this paper.

Chapter 4 Conclusions and Future Directions

4.1 Summary of Work

In this dissertation, investigations determining several advances were presented on the endogenous cellular responses contributing to the efficacy and safety of tissue derived ECM biomaterial therapies. This work highlights the dynamic interaction of the myocardial matrix material and ECM derived materials with endogenous cell populations and biomolecules, particularly immune cell populations and sources of oxidative stress, that contribute to the observed efficacy and safety of these materials for stimulating repair. The studies described most commonly utilize an injectable myocardial matrix hydrogel material derived from porcine left ventricular tissue, though the results determined can more broadly apply to naturally derived decellularized materials biomaterials, along with providing some insight to the regenerative medicine and immunology fields.

In the first study, properties of the hydrogel in relation to the mitigation of sources of oxidative stress were determined showing that the matrix could act as an ROS scavenger/sink and shield encapsulated cells from oxidative stress. This was determined to be, in part, from amino acids that could be oxidized such as thiol groups in free cysteine residues along with lesser contributions from methionine and histidine residues. Notably, as ECM proteins have different percentages of cysteine residues and are known to have different compositions during development, particularly, an increases in collagen which contains few cysteines, this could contribute to the observed changes in regenerative potential and greater regenerative effect observed with ECM derived or characteristic of tissue from fetal and neonatal stages[205-207]. Investigation of whether matrix aided in the continued proliferation of neonatal derived rat cardiomyocytes *in vitro* also demonstrated greater progeny generation compared to collagen controls along with shielding from activation of stress pathways from oxidative stress. Assessment in a rat ischemia-reperfusion rat showed an increase of thymidine analog uptake in

cardiomyocyte nuclei during the earlier timepoint after injection of the material, however, this required a longer timeframe of delivery to resolve a difference. Furthermore, issues with common proliferative stains showing positive signal in healthy tissue made confirmation of the degree of cell cycle progression difficult to confirm. Thus, these results provide evidence of a proliferative microenvironment for cardiomyocytes, though evaluation of common methods needs to be done to determine the biological relevance of these results.

In the second study, evaluation of the immune response in an immune system humanized mouse model as an improved representative pre-clinical model demonstrated a dynamic immune response to our material from macrophage and T cell populations. Responses were determined with a subcutaneous injection for a focus on immune cell infiltration and response without the additional influence from tissue or injury. At 3 days, an early dominant presence of cytotoxic T cells, Th1 cells, and M1 macrophages were observed. This response shifted to a type 2 dominant response with Th2 cells and M2 macrophages. This type of shift mimicked the immune response observed in physiological tissue repair.

In the final study, the contribution of mast cells to the dynamic immune response stimulated injectable ECM materials was evaluated. Mast cells are known to release a wide array of cytokines and factors related to both physiological and pathological remodeling, however, their function is mainly related to inflammatory responses. This study demonstrated that mast cells aid in the progression of the immune response stimulated from ECM biomaterials. In male mice, mast cells were needed to progress macrophage polarization and presence of cytokines from the IL-1 family and related downstream pathways, which were maintained in mast cell deficient mice, and reversed with mast cell reconstituted mice. In contrast, progression of the immune response was accelerated in female mice with responses suggesting a more dominant response from female hormones on immune cell populations. Therefore, these results demonstrate a major influence of mast cells on the immune response

despite their low cell number and emphasize their potential alterative roles outside their classical pro-inflammatory activated phenotype.

4.2. Future Directions

Demonstrations of efficacy and safety of injectable decellularized ECM therapies have prompted their evaluations in early clinical trial studies[187]. Decellularized materials have provided methods to create materials mimicking the native extracellular microenvironment that cannot be achieved with current engineering techniques, however, this complexity does make the contributing reparative mechanism less straightforward to delineate. Furthermore, approval for continued evaluation of this material in later clinical trial phases and future improvement require a greater understanding of the responses contributing to the observed *in vivo* responses. Based on work in this dissertation, several contributing interactions and cellular responses have been highlighted that could be further investigated or stimulated to enhance repair. However, a major limitation of these methods is the use of distinct animal models or low-throughput methods with knockout models to associate roles with specific cell types. To improve characterization, high throughput omics methods such as single cell RNA-seq would allow improved delineation of the results to specific cell types in a high throughput manner and allow for further discovery of mechanisms contributing to these responses similar to previous bulk transcriptomic studies. Alternatively, improved models of the human response representing characteristics of the expected patient population could also improve translational representation of the results.

References

1. Go AS, Mozaffarian D, Roger VL, Benjamin EJ, Berry JD, Blaha MJ, Dai S, Ford ES, Fox CS, Franco S, Fullerton HJ, Gillespie C, Hailpern SM, Heit JA, Howard VJ, Huffman MD, Judd SE, Kissela BM, Kittner SJ, Lackland DT, Lichtman JH, Lisabeth LD, Mackey RH, Magid DJ, Marcus GM, Marelli A, Matchar DB, McGuire DK, Mohler ER, Moy CS, Mussolino ME, Neumar RW, Nichol G, Pandey DK, Paynter NP, Reeves MJ, Sorlie PD, Stein J, Towfighi A, Turan TN, Virani SS, Wong ND, Woo D and Turner MB. Heart Disease and Stroke Statistics—2014 Update: A Report From the American Heart Association. *Circulation*. 2014;129:399-410.

2. World Health Organization. WHO methods and data sources for country-level causes of death 2000–2015. *Geneva, Switzerland: WHO*. 2017.

3. Kurrelmeyer K, Kalra D, Bozkurt B, Wang F, Dibbs Z, Seta Y, Baumgarten G, Engle D, Sivasubramanian N and Mann DL. Cardiac remodeling as a consequence and cause of progressive heart failure. *Clin Cardiol*. 1998;21:I14-9.

4. Williams ML, Trivedi JR, McCants KC, Prabhu SD, Birks EJ, Oliver L and Slaughter MS. Heart transplant vs left ventricular assist device in heart transplant-eligible patients. *Ann Thorac Surg*. 2011;91:1330-3; discussion 1333-4.

5. OPTN/SRTR. OPTN/SRTR 2016 Annual Data Report: Introduction. *Am J Transplant*. 2018;18 Suppl 1:10-17.

6. Long EF, Swain GW and Mangi AA. Comparative survival and cost-effectiveness of advanced therapies for end-stage heart failure. *Circ Heart Fail*. 2014;7:470-8.

7. Katz JN, Waters SB, Hollis IB and Chang PP. Advanced therapies for end-stage heart failure. *Curr Cardiol Rev*. 2015;11:63-72.

8. Yadav P, Yadav H, Shah VG, Shah G and Dhaka G. Biomedical Biopolymers, their Origin and Evolution in Biomedical Sciences: A Systematic Review. *Journal of Clinical and Diagnostic Research*. 2015;9:ZE21-ZE25.

9. Rane AA and Christman KL. Biomaterials for the treatment of myocardial infarction: a 5-year update. *J Am Coll Cardiol*. 2011;58:2615-29.

10. Christman KL, Fok HH, Sievers RE, Fang Q and Lee RJ. Fibrin glue alone and skeletal myoblasts in a fibrin scaffold preserve cardiac function after myocardial infarction. *Tissue Eng*. 2004;10:403-9.

11. Christman KL, Vardanian AJ, Fang Q, Sievers RE, Fok HH and Lee RJ. Injectable fibrin scaffold improves cell transplant survival, reduces infarct expansion, and induces neovasculature formation in ischemic myocardium. *J Am Coll Cardiol*. 2004;44:654-60.

12. Spang MT and Christman KL. Extracellular matrix hydrogel therapies: In vivo applications and development. *Acta Biomater*. 2018;68:1-14.

13. Hernandez MJ and Christman KL. Designing Acellular Injectable Biomaterial Therapeutics for Treating Myocardial Infarction and Peripheral Artery Disease. *JACC: Basic to Translational Science*. 2017;2:212-226.

14. Ungerleider JL and Christman KL. Concise review: injectable biomaterials for the treatment of myocardial infarction and peripheral artery disease: translational challenges and progress. *Stem Cells Transl Med*. 2014;3:1090-9.

15. Johnson TD and Christman KL. Injectable hydrogel therapies and their delivery strategies for treating myocardial infarction. *Expert Opin Drug Deliv*. 2013;10:59-72.

16. Moriarty TF. The law of Laplace. Its limitations as a relation for diastolic pressure, volume, or wall stress of the left ventricle. *Circ Res*. 1980;46:321-31.

17. Oz MC, Konertz WF, Kleber FX, Mohr FW, Gummert JF, Ostermeyer J, Lass M, Raman J, Acker MA and Smedira N. Global surgical experience with the Acorn cardiac support device. *J Thorac Cardiovasc Surg*. 2003;126:983-91.

18. Mann DL, Kubo SH, Sabbah HN, Starling RC, Jessup M, Oh JK and Acker MA. Beneficial effects of the CorCap cardiac support device: five-year results from the Acorn Trial. *J Thorac Cardiovasc Surg*. 2012;143:1036-42.

19. Klodell CT, Jr., McGiffin DC, Rayburn BK, Sun B, Abraham WT, Conte JV, Russell SD, Pae WE, Jr., Boehmer JP and Aranda JM, Jr. Initial United States experience with the Paracor HeartNet myocardial constraint device for heart failure. *J Thorac Cardiovasc Surg*. 2007;133:204-9.

20. Costanzo MR, Ivanhoe RJ, Kao A, Anand IS, Bank A, Boehmer J, Demarco T, Hergert CM, Holcomb RG, Maybaum S, Sun B, Vassiliades TA, Jr., Rayburn BK and Abraham WT. Prospective evaluation of elastic restraint to lessen the effects of heart failure (PEERLESS-HF) trial. *J Card Fail*. 2012;18:446-58.

21. Klodell CT, Jr., Aranda JM, Jr., McGiffin DC, Rayburn BK, Sun B, Abraham WT, Pae WE, Jr., Boehmer JP, Klein H and Huth C. Worldwide surgical experience with the Paracor HeartNet cardiac restraint device. *J Thorac Cardiovasc Surg*. 2008;135:188-95.

22. Abraham WT, Anand I, Aranda JM, Jr., Boehmer J, Costanzo MR, DeMarco T, Holcomb R, Ivanhoe R, Kolber M and Rayburn B. Randomized controlled trial of ventricular elastic support therapy in the treatment of symptomatic heart failure: rationale and design. *Am Heart J*. 2012;164:638-45.

23. Wall ST, Walker JC, Healy KE, Ratcliffe MB and Guccione JM. Theoretical impact of the injection of material into the myocardium: a finite element model simulation. *Circulation*. 2006;114:2627-35.

24. Wenk JF, Eslami P, Zhang Z, Xu C, Kuhl E, Gorman JH, Robb JD, Ratcliffe MB, Gorman RC and Guccione JM. A Novel Method for Quantifying the In-Vivo Mechanical Effect of Material Injected into a Myocardial Infarction. *The Annals of thoracic surgery*. 2011;92:935-941.

25. Genet M, Lee LC, Nguyen R, Haraldsson H, Acevedo-Bolton G, Zhang Z, Ge L, Ordovas K, Kozerke S and Guccione JM. Distribution of normal human left ventricular myofiber stress at end diastole and end systole: a target for in silico design of heart failure treatments. *Journal of Applied Physiology*. 2014;117:142-152.

26. Rane AA, Chuang JS, Shah A, Hu DP, Dalton ND, Gu Y, Peterson KL, Omens JH and Christman KL. Increased infarct wall thickness by a bio-inert material is insufficient to prevent negative left ventricular remodeling after myocardial infarction. *PLoS One*. 2011;6:e21571.

27. McGarvey JR, Pettaway S, Shuman JA, Novack CP, Zellars KN, Freels PD, Echols RL, Jr., Burdick JA, Gorman JH, 3rd, Gorman RC and Spinale FG. Targeted injection of a biocomposite material alters macrophage and fibroblast phenotype and function following myocardial infarction: relation to left ventricular remodeling. *J Pharmacol Exp Ther*. 2014;350:701-9.

28. Leor J, Tuvia S, Guetta V, Manczur F, Castel D, Willenz U, Petnehazy O, Landa N, Feinberg MS, Konen E, Goitein O, Tsur-Gang O, Shaul M, Klapper L and Cohen S. Intracoronary injection of in situ forming alginate hydrogel reverses left ventricular remodeling after myocardial infarction in Swine. *J Am Coll Cardiol*. 2009;54:1014-23.

29. Tse JR and Engler AJ. Stiffness gradients mimicking in vivo tissue variation regulate mesenchymal stem cell fate. *PLoS One*. 2011;6:e15978.

30. McCain ML, Sheehy SP, Grosberg A, Goss JA and Parker KK. Recapitulating maladaptive, multiscale remodeling of failing myocardium on a chip. *Proc Natl Acad Sci U S A*. 2013;110:9770-5.

31. Young JL, Kretchmer K, Ondeck MG, Zambon AC and Engler AJ. Mechanosensitive kinases regulate stiffness-induced cardiomyocyte maturation. *Sci Rep*. 2014;4:6425.

32. Ifkovits JL, Tous E, Minakawa M, Morita M, Robb JD, Koomalsingh KJ, Gorman JH, 3rd, Gorman RC and Burdick JA. Injectable hydrogel properties influence infarct expansion and extent of postinfarction left ventricular remodeling in an ovine model. *Proc Natl Acad Sci U S A*. 2010;107:11507-12.

33. Notari M, Ventura-Rubio A, Bedford-Guaus SJ, Jorba I, Mulero L, Navajas D, Marti M and Raya A. The local microenvironment limits the regenerative potential of the mouse neonatal heart. *Sci Adv*. 2018;4:eaao5553.

34. Huang NF, Yu J, Sievers R, Li S and Lee RJ. Injectable biopolymers enhance angiogenesis after myocardial infarction. *Tissue Eng*. 2005;11:1860-6.

35. Lu WN, Lu SH, Wang HB, Li DX, Duan CM, Liu ZQ, Hao T, He WJ, Xu B, Fu Q, Song YC, Xie XH and Wang CY. Functional improvement of infarcted heart by co-injection of embryonic stem cells with temperature-responsive chitosan hydrogel. *Tissue Eng Part A*. 2009;15:1437-47.

36. Lu S, Wang H, Lu W, Liu S, Lin Q, Li D, Duan C, Hao T, Zhou J, Wang Y, Gao S and Wang C. Both the transplantation of somatic cell nuclear transfer- and fertilization-derived mouse embryonic stem cells with temperature-responsive chitosan hydrogel

improve myocardial performance in infarcted rat hearts. *Tissue Eng Part A*. 2010;16:1303-15.

37. Wang H, Zhang X, Li Y, Ma Y, Zhang Y, Liu Z, Zhou J, Lin Q, Wang Y, Duan C and Wang C. Improved myocardial performance in infarcted rat heart by co-injection of basic fibroblast growth factor with temperature-responsive chitosan hydrogel. *J Heart Lung Transplant*. 2010;29:881-7.

38. Xu B, Li Y, Deng B, Liu X, Wang L and Zhu QL. Chitosan hydrogel improves mesenchymal stem cell transplant survival and cardiac function following myocardial infarction in rats. *Exp Ther Med*. 2017;13:588-594.

39. Latinovic O, Hough LA and Daniel Ou-Yang H. Structural and micromechanical characterization of type I collagen gels. *J Biomech*. 2010;43:500-5.

40. Moreno-Arotzena O, Meier JG, Del Amo C and Garcia-Aznar JM. Characterization of Fibrin and Collagen Gels for Engineering Wound Healing Models. *Materials (Basel)*. 2015;8:1636-1651.

41. Johnson TD, Lin SY and Christman KL. Tailoring material properties of a nanofibrous extracellular matrix derived hydrogel. *Nanotechnology*. 2011;22:494015.

42. Mantovani A, Sica A and Locati M. Macrophage polarization comes of age. *Immunity*. 2005;23:344-6.

43. Glimcher LH and Murphy KM. Lineage commitment in the immune system: the T helper lymphocyte grows up. *Genes Dev*. 2000;14:1693-711.

44. Lurier EB, Dalton D, Dampier W, Raman P, Nassiri S, Ferraro NM, Rajagopalan R, Sarmady M and Spiller KL. Transcriptome analysis of IL-10-stimulated (M2c) macrophages by next-generation sequencing. *Immunobiology*. 2017;222:847-856.

45. Park J, Gao W, Whiston R, Strom TB, Metcalfe S and Fahmy TM. Modulation of CD4+ T lymphocyte lineage outcomes with targeted, nanoparticle-mediated cytokine delivery. *Mol Pharm*. 2011;8:143-52.

46. Murray PJ, Allen JE, Biswas SK, Fisher EA, Gilroy DW, Goerdt S, Gordon S, Hamilton JA, Ivashkiv LB, Lawrence T, Locati M, Mantovani A, Martinez FO, Mege JL, Mosser DM, Natoli G, Saeij JP, Schultze JL, Shirey KA, Sica A, Suttles J, Udalova I, van Ginderachter JA, Vogel SN and Wynn TA. Macrophage activation and polarization: nomenclature and experimental guidelines. *Immunity*. 2014;41:14-20.

47. Zemmour D, Zilionis R, Kiner E, Klein AM, Mathis D and Benoist C. Single-cell gene expression reveals a landscape of regulatory T cell phenotypes shaped by the TCR. *Nat Immunol*. 2018;19:291-301.

48. Ahn RS, Taravati K, Lai K, Lee KM, Nititham J, Gupta R, Chang DS, Arron ST, Rosenblum M and Liao W. Transcriptional landscape of epithelial and immune cell populations revealed through FACS-seq of healthy human skin. *Scientific Reports*. 2017;7:1343.

49. Nassiri S, Zakeri I, Weingarten MS and Spiller KL. Relative Expression of Proinflammatory and Antiinflammatory Genes Reveals Differences between Healing and Nonhealing Human Chronic Diabetic Foot Ulcers. *J Invest Dermatol*. 2015;135:1700-1703.

50. Spiller KL, Nassiri S, Witherel CE, Anfang RR, Ng J, Nakazawa KR, Yu T and Vunjak-Novakovic G. Sequential delivery of immunomodulatory cytokines to facilitate the M1-to-M2 transition of macrophages and enhance vascularization of bone scaffolds. *Biomaterials*. 2015;37:194-207.

51. Li WA, Lu BY, Gu L, Choi Y, Kim J and Mooney DJ. The effect of surface modification of mesoporous silica micro-rod scaffold on immune cell activation and infiltration. *Biomaterials*. 2016;83:249-56.

52. Padmore T, Stark C, Turkevich LA and Champion JA. Quantitative analysis of the role of fiber length on phagocytosis and inflammatory response by alveolar macrophages. *Biochim Biophys Acta*. 2017;1861:58-67.

53. McWhorter FY, Davis CT and Liu WF. Physical and mechanical regulation of macrophage phenotype and function. *Cell Mol Life Sci*. 2015;72:1303-16.

54. Irwin EF, Saha K, Rosenbluth M, Gamble LJ, Castner DG and Healy KE. Modulus-dependent macrophage adhesion and behavior. *J Biomater Sci Polym Ed*. 2008;19:1363-82.

55. Andorko JI, Hess KL, Pineault KG and Jewell CM. Intrinsic immunogenicity of rapidly-degradable polymers evolves during degradation. *Acta Biomater*. 2016;32:24-34.

56. Rayahin JE, Buhrman JS, Zhang Y, Koh TJ and Gemeinhart RA. High and low molecular weight hyaluronic acid differentially influence macrophage activation. *Acs Biomater Sci Eng*. 2015;1:481-493.

57. Babensee JE and Paranjpe A. Differential levels of dendritic cell maturation on different biomaterials used in combination products. *J Biomed Mater Res A*. 2005;74:503-10.

58. Dziki JL, Wang DS, Pineda C, Sicari BM, Rausch T and Badylak SF. Solubilized extracellular matrix bioscaffolds derived from diverse source tissues differentially influence macrophage phenotype. *J Biomed Mater Res A*. 2017;105:138-147.

59. Spiller KL, Anfang RR, Spiller KJ, Ng J, Nakazawa KR, Daulton JW and Vunjak-Novakovic G. The role of macrophage phenotype in vascularization of tissue engineering scaffolds. *Biomaterials*. 2014;35:4477-88.

60. Anderson JM, Rodriguez A and Chang DT. Foreign body reaction to biomaterials. *Semin Immunol*. 2008;20:86-100.

61. Badylak SF and Gilbert TW. Immune response to biologic scaffold materials. *Semin Immunol*. 2008;20:109-16.

62. Gretzer C, Emanuelsson L, Liljensten E and Thomsen P. The inflammatory cell influx and cytokines changes during transition from acute inflammation to fibrous repair around implanted materials. *J Biomater Sci Polym Ed*. 2006;17:669-87.

63. Damanik FF, Rothuizen TC, van Blitterswijk C, Rotmans JI and Moroni L. Towards an in vitro model mimicking the foreign body response: tailoring the surface properties of biomaterials to modulate extracellular matrix. *Sci Rep*. 2014;4:6325.

64. Miller KM and Anderson JM. In vitro stimulation of fibroblast activity by factors generated from human monocytes activated by biomedical polymers. *J Biomed Mater Res*. 1989;23:911-30.

65. Giraud MN, Ayuni E, Cook S, Siepe M, Carrel TP and Tevaearai HT. Hydrogel-based engineered skeletal muscle grafts normalize heart function early after myocardial infarction. *Artif Organs*. 2008;32:692-700.

66. Mukherjee R, Zavadzkas JA, Saunders SM, McLean JE, Jeffords LB, Beck C, Stroud RE, Leone AM, Koval CN, Rivers WT, Basu S, Sheehy A, Michal G and Spinale FG. Targeted myocardial microinjections of a biocomposite material reduces infarct expansion in pigs. *Ann Thorac Surg*. 2008;86:1268-76.

67. Pieper JS, Hafmans T, van Wachem PB, van Luyn MJ, Brouwer LA, Veerkamp JH and van Kuppevelt TH. Loading of collagen-heparan sulfate matrices with bFGF promotes angiogenesis and tissue generation in rats. *J Biomed Mater Res*. 2002;62:185-94.

68. Keane TJ, Swinehart IT and Badylak SF. Methods of tissue decellularization used for preparation of biologic scaffolds and in vivo relevance. *Methods*. 2015;84:25-34.

69. Bowers SLK, Banerjee I and Baudino TA. The extracellular matrix: At the center of it all. *Journal of Molecular and Cellular Cardiology*. 2010;48:474-482.

70. Brown BN and Badylak SF. Extracellular matrix as an inductive scaffold for functional tissue reconstruction. *Translational research : the journal of laboratory and clinical medicine*. 2014;163:268-285.

71. Seif-Naraghi SB, Singelyn JM, Salvatore MA, Osborn KG, Wang JJ, Sampat U, Kwan OL, Strachan GM, Wong J, Schup-Magoffin PJ, Braden RL, Bartels K, DeQuach JA, Preul M, Kinsey AM, DeMaria AN, Dib N and Christman KL. Safety and efficacy of an injectable extracellular matrix hydrogel for treating myocardial infarction. *Sci Transl Med*. 2013;5:173ra25.

72. Singelyn JM, Sundaramurthy P, Johnson TD, Schup-Magoffin PJ, Hu DP, Faulk DM, Wang J, Mayle KM, Bartels K, Salvatore M, Kinsey AM, Demaria AN, Dib N and Christman KL. Catheter-deliverable hydrogel derived from decellularized ventricular extracellular matrix increases endogenous cardiomyocytes and preserves cardiac function post-myocardial infarction. *J Am Coll Cardiol*. 2012;59:751-63.

73. Wassenaar JW, Gaetani R, Garcia JJ, Braden RL, Luo CG, Huang D, DeMaria AN, Omens JH and Christman KL. Evidence for Mechanisms Underlying the Functional Benefits of a Myocardial Matrix Hydrogel for Post-MI Treatment. *J Am Coll Cardiol*. 2016;67:1074-86.

74. Duchesne E, Bouchard P, Roussel MP and Cote CH. Mast cells can regulate skeletal muscle cell proliferation by multiple mechanisms. *Muscle Nerve*. 2013;48:403-14.

75. Ngkelo A, Richart A, Kirk JA, Bonnin P, Vilar J, Lemitre M, Marck P, Branchereau M, Le Gall S, Renault N, Guerin C, Ranek MJ, Kervadec A, Danelli L, Gautier G, Blank U, Launay P, Camerer E, Bruneval P, Menasche P, Heymes C, Luche E, Casteilla L, Cousin B, Rodewald H-R, Kass DA and Silvestre J-S. Mast cells regulate myofilament calcium sensitization and heart function after myocardial infarction. *The Journal of Experimental Medicine*. 2016;213:1353.

76. Levick SP, Meléndez GC, Plante E, McLarty JL, Brower GL and Janicki JS. Cardiac mast cells: the centrepiece in adverse myocardial remodelling. *Cardiovascular Research*. 2010;89:12-19.

77. Porrello ER, Mahmoud AI, Simpson E, Hill JA, Richardson JA, Olson EN and Sadek HA. Transient Regenerative Potential of the Neonatal Mouse Heart. *Science*. 2011;331:1078-1080.

78. Drenckhahn JD, Schwarz QP, Gray S, Laskowski A, Kiriazis H, Ming Z, Harvey RP, Du XJ, Thorburn DR and Cox TC. Compensatory growth of healthy cardiac cells in the presence of diseased cells restores tissue homeostasis during heart development. *Dev Cell*. 2008;15:521-33.

79. Zhu W, Zhang E, Zhao M, Chong Z, Fan C, Tang Y, Hunter JD, Borovjagin AV, Walcott GP, Chen JY, Qin G and Zhang J. Regenerative Potential of Neonatal Porcine Hearts. *Circulation*. 2018;138:2809-2816.

80. Ye L, D'Agostino G, Loo SJ, Wang CX, Su LP, Tan SH, Tee GZ, Pua CJ, Pena EM, Cheng RB, Chen WC, Abdurrachim D, Lalic J, Tan RS, Lee TH, Zhang J and Cook SA. Early Regenerative Capacity in the Porcine Heart. *Circulation*. 2018;138:2798-2808.

81. Bergmann O, Bhardwaj RD, Bernard S, Zdunek S, Barnabé-Heider F, Walsh S, Zupicich J, Alkass K, Buchholz BA, Druid H, Jovinge S and Frisén J. Evidence for cardiomyocyte renewal in humans. *Science (New York, NY)*. 2009;324:98-102.

82. Naqvi N, Li M, Calvert JW, Tejada T, Lambert JP, Wu J, Kesteven SH, Holman SR, Matsuda T, Lovelock JD, Howard WW, Iismaa SE, Chan AY, Crawford BH, Wagner MB, Martin DI, Lefer DJ, Graham RM and Husain A. A proliferative burst during preadolescence establishes the final cardiomyocyte number. *Cell*. 2014;157:795-807.

83. Mollova M, Bersell K, Walsh S, Savla J, Das LT, Park SY, Silberstein LE, Dos Remedios CG, Graham D, Colan S and Kuhn B. Cardiomyocyte proliferation contributes to heart growth in young humans. *Proc Natl Acad Sci U S A*. 2013;110:1446-51.

84. Alkass K, Panula J, Westman M, Wu TD, Guerquin-Kern JL and Bergmann O. No Evidence for Cardiomyocyte Number Expansion in Preadolescent Mice. *Cell*. 2015;163:1026-36.

85. Soonpaa MH, Zebrowski DC, Platt C, Rosenzweig A, Engel FB and Field LJ. Cardiomyocyte Cell-Cycle Activity during Preadolescence. *Cell*. 2015;163:781-2.

86. Puente BN, Kimura W, Muralidhar SA, Moon J, Amatruda JF, Phelps KL, Grinsfelder D, Rothermel BA, Chen R, Garcia JA, Santos CX, Thet S, Mori E, Kinter MT, Rindler PM, Zacchigna S, Mukherjee S, Chen DJ, Mahmoud AI, Giacca M, Rabinovitch PS, Aroumougame A, Shah AM, Szweda LI and Sadek HA. The oxygen-rich postnatal environment induces cardiomyocyte cell-cycle arrest through DNA damage response. *Cell*. 2014;157:565-79.

87. Jopling C, Sune G, Faucherre A, Fabregat C and Izpisua Belmonte JC. Hypoxia induces myocardial regeneration in zebrafish. *Circulation*. 2012;126:3017-27.

88. Szibor M, Poling J, Warnecke H, Kubin T and Braun T. Remodeling and dedifferentiation of adult cardiomyocytes during disease and regeneration. *Cell Mol Life Sci*. 2014;71:1907-16.

89. Pohjoismaki JL, Boettger T, Liu Z, Goffart S, Szibor M and Braun T. Oxidative stress during mitochondrial biogenesis compromises mtDNA integrity in growing hearts and induces a global DNA repair response. *Nucleic Acids Res*. 2012;40:6595-607.

90. Zhang Y, Li TS, Lee ST, Wawrowsky KA, Cheng K, Galang G, Malliaras K, Abraham MR, Wang C and Marban E. Dedifferentiation and proliferation of mammalian cardiomyocytes. *PLoS One*. 2010;5:e12559.

91. Kimura W, Xiao F, Canseco DC, Muralidhar S, Thet S, Zhang HM, Abderrahman Y, Chen R, Garcia JA, Shelton JM, Richardson JA, Ashour AM, Asaithamby A, Liang H, Xing C, Lu Z, Zhang CC and Sadek HA. Hypoxia fate mapping identifies cycling cardiomyocytes in the adult heart. *Nature*. 2015;523:226-30.

92. Beltrami AP, Barlucchi L, Torella D, Baker M, Limana F, Chimenti S, Kasahara H, Rota M, Musso E, Urbanek K, Leri A, Kajstura J, Nadal-Ginard B and Anversa P. Adult cardiac stem cells are multipotent and support myocardial regeneration. *Cell*. 2003;114:763-76.

93. Toma C, Pittenger MF, Cahill KS, Byrne BJ and Kessler PD. Human mesenchymal stem cells differentiate to a cardiomyocyte phenotype in the adult murine heart. *Circulation*. 2002;105:93-8.

94. van Berlo JH, Kanisicak O, Maillet M, Vagnozzi RJ, Karch J, Lin SC, Middleton RC, Marban E and Molkentin JD. c-kit+ cells minimally contribute cardiomyocytes to the heart. *Nature*. 2014;509:337-41.

95. Sultana N, Zhang L, Yan J, Chen J, Cai W, Razzaque S, Jeong D, Sheng W, Bu L and Xu M. Resident c-kit+ cells in the heart are not cardiac stem cells. *Nature communications*. 2015;6.

96. Hsieh PC, Segers VF, Davis ME, MacGillivray C, Gannon J, Molkentin JD, Robbins J and Lee RT. Evidence from a genetic fate-mapping study that stem cells refresh adult mammalian cardiomyocytes after injury. *Nat Med*. 2007;13:970-4.

97. Senyo SE, Steinhauser ML, Pizzimenti CL, Yang VK, Cai L, Wang M, Wu TD, Guerquin-Kern JL, Lechene CP and Lee RT. Mammalian heart renewal by pre-existing cardiomyocytes. *Nature*. 2013;493:433-6.

98. Makkar RR, Smith RR, Cheng K, Malliaras K, Thomson LE, Berman D, Czer LS, Marban L, Mendizabal A, Johnston PV, Russell SD, Schuleri KH, Lardo AC, Gerstenblith G and Marban E. Intracoronary cardiosphere-derived cells for heart regeneration after myocardial infarction (CADUCEUS): a prospective, randomised phase 1 trial. *Lancet*. 2012;379:895-904.

99. Malliaras K, Zhang Y, Seinfeld J, Galang G, Tseliou E, Cheng K, Sun B, Aminzadeh M and Marban E. Cardiomyocyte proliferation and progenitor cell recruitment underlie therapeutic regeneration after myocardial infarction in the adult mouse heart. *EMBO Mol Med*. 2013;5:191-209.

100. Seif-Naraghi SB, Singelyn JM, Salvatore MA, Osborn KG, Wang JJ, Sampat U, Kwan OL, Strachan GM, Wong J, Schup-Magoffin PJ, Braden RL, Bartels K, DeQuach JA, Preul M, Kinsey AM, DeMaria AN, Dib N and Christman KL. Safety and Efficacy of an Injectable Extracellular Matrix Hydrogel for Treating Myocardial Infarction. *Sci Transl Med*. 2013;5:173ra25.

101. French KM, Boopathy AV, DeQuach JA, Chingozha L, Lu H, Christman KL and Davis ME. A naturally derived cardiac extracellular matrix enhances cardiac progenitor cell behavior in vitro. *Acta Biomater*. 2012;8:4357-4364.

102. Bergmann O, Zdunek S, Alkass K, Druid H, Bernard S and Frisen J. Identification of cardiomyocyte nuclei and assessment of ploidy for the analysis of cell turnover. *Exp Cell Res*. 2011;317:188-94.

103. Moore-Morris T, Guimaraes-Camboa N, Banerjee I, Zambon AC, Kisseleva T, Velayoudon A, Stallcup WB, Gu Y, Dalton ND, Cedenilla M, Gomez-Amaro R, Zhou B, Brenner DA, Peterson KL, Chen J and Evans SM. Resident fibroblast lineages mediate pressure overload-induced cardiac fibrosis. *J Clin Invest*. 2014;124:2921-34.

104. Puente BN, Kimura W, Muralidhar SA, Moon J, Amatruda JF, Phelps KL, Grinsfelder D, Rothermel BA, Chen R, Garcia JA, Santos CX, Thet S, Mori E, Kinter MT, Rindler PM, Zacchigna S, Mukherjee S, Chen DJ, Mahmoud AI, Giacca M, Rabinovitch PS, Aroumougame A, Shah AM, Szweda LI and Sadek HA. The oxygen-rich postnatal environment induces cardiomyocyte cell-cycle arrest through DNA damage response. *Cell*. 2014;157:565-579.

105. Kimura W, Xiao F, Canseco DC, Muralidhar S, Thet S, Zhang HM, Abderrahman Y, Chen R, Garcia JA, Shelton JM, Richardson JA, Ashour AM, Asaithamby A, Liang H, Xing C, Lu Z, Zhang CC and Sadek HA. Hypoxia fate mapping identifies cycling cardiomyocytes in the adult heart. *Nature*. 2015;523:226.

106. Nakada Y, Canseco DC, Thet S, Abdisalaam S, Asaithamby A, Santos CX, Shah AM, Zhang H, Faber JE, Kinter MT, Szweda LI, Xing C, Hu Z, Deberardinis RJ, Schiattarella G, Hill JA, Oz O, Lu Z, Zhang CC, Kimura W and Sadek HA. Hypoxia induces heart regeneration in adult mice. *Nature*. 2016;541:222.

107. Ungerleider JL, Johnson TD, Rao N and Christman KL. Fabrication and characterization of injectable hydrogels derived from decellularized skeletal and cardiac muscle. *Methods*. 2015;84:53-9.

108. Rasoulpour RJ, Andrus AK, Marty MS, Zhang F, Thomas J, LeBaron MJ, Papineni S, Pottenger LH and Eisenbrandt DL. Pronamide: Human relevance of liver-mediated rat leydig cell tumors. *Regul Toxicol Pharmacol*. 2015;72:394-404.

109. Rao N, Agmon G, Tierney MT, Ungerleider JL, Braden RL, Sacco A and Christman KL. Engineering an Injectable Muscle-Specific Microenvironment for Improved Cell Delivery Using a Nanofibrous Extracellular Matrix Hydrogel. *ACS Nano*. 2017;11:3851-3859.

110. Pashuck ET and Stevens MM. Designing regenerative biomaterial therapies for the clinic. *Sci Transl Med*. 2012;4:160sr4.

111. Turner NJ and Badylak SF. Regeneration of skeletal muscle. *Cell Tissue Res*. 2012;347:759-774.

112. Rane AA and Christman KL. Biomaterials for the treatment of myocardial infarction: a 5-year update. *Journal of the American College of Cardiology*. 2011;58:2615-2629.

113. Tottey S, Johnson SA, Crapo PM, Reing JE, Zhang L, Jiang H, Medberry CJ, Reines B and Badylak SF. The effect of source animal age upon extracellular matrix scaffold properties. *Biomaterials*. 2011;32:128-136.

114. Bowers SL, Banerjee I and Baudino TA. The extracellular matrix: at the center of it all. *Journal of molecular and cellular cardiology*. 2010;48:474-82.

115. Keane TJ, Londono R, Turner NJ and Badylak SF. Consequences of ineffective decellularization of biologic scaffolds on the host response. *Biomaterials*. 2012;33:1771-1781.

116. Badylak SF. Xenogeneic extracellular matrix as a scaffold for tissue reconstruction. *Transpl Immunol*. 2004;12:367-377.

117. Badylak SF and Gilbert TW. Immune response to biologic scaffold materials. *Semin Immunol*. 2008;20:109-116.

118. Sicari BM, Johnson SA, Siu BF, Crapo PM, Daly KA, Jiang H, Medberry CJ, Tottey S, Turner NJ and Badylak SF. The effect of source animal age upon the in vivo remodeling characteristics of an extracellular matrix scaffold. *Biomaterials*. 2012;33:5524-5533.

119. Badylak SF. The extracellular matrix as a biologic scaffold material. *Biomaterials*. 2007;28:3587-3593.

120. Seif-Naraghi SB, Singelyn JM, Salvatore MA, Osborn KG, Wang JJ, Sampat U, Kwan OL, Strachan GM, Wong J, Schup-Magoffin PJ, Braden RL, Bartels K, DeQuach JA, Preul M, Kinsey AM, Demaria AN, Dib N and Christman KL. Safety and efficacy of an injectable extracellular matrix hydrogel for treating myocardial infarction. *Science translational medicine*. 2013;5:173ra25.

121. Mestas J and Hughes CC. Of mice and not men: differences between mouse and human immunology. *J Immunol*. 2004;172:2731-8.

122. Varki NM, Strobert E, Dick EJ, Benirschke K and Varki A. Biomedical differences between human and nonhuman hominids: potential roles for uniquely human aspects of sialic acid biology. *Annu Rev Pathol*. 2011;6:365-393.

123. Říhová B. Biocompatibility of biomaterials: hemocompatibility, immunocompatiblity and biocompatibility of solid polymeric materials and soluble targetable polymeric carriers. *Advanced Drug Delivery Reviews*. 1996;21:157-176.

124. Onuki Y, Bhardwaj U and Papadimitrakopoulos F. A review of the biocompatibility of implantable devices: current challenges to overcome foreign body response. *J Diabetes Sci*. 2008.

125. Legrand N and Weijer K. Experimental Models to Study Development and Function of the Human Immune System In Vivo. *The Journal of Immunology*. 2006.

126. Lan P, Tonomura N, Shimizu A, Wang S and Yang Y-G. Reconstitution of a functional human immune system in immunodeficient mice through combined human fetal thymus/liver and CD34+ cell transplantation. *Blood*. 2006;108:487-492.

127. Zhang B, Duan Z and Zhao Y. Mouse models with human immunity and their application in biomedical research. *Journal of Cellular and Molecular Medicine*. 2009;13:1043-1058.

128. Tonomura N, Shimizu A, Wang S, Yamada K, Tchipashvili V, Weir GC and Yang Y-G. Pig islet xenograft rejection in a mouse model with an established human immune system. *Xenotransplantation*. 2008;15:129-135.

129. Rong Z, Wang M, Hu Z, Stradner M, Zhu S, Kong H, Yi H, Goldrath A, Yang YG, Xu Y and Fu X. An effective approach to prevent immune rejection of human ESC-derived allografts. *Cell Stem Cell*. 2014;14:121-30.

130. Singelyn JM, DeQuach JA, Seif-Naraghi SB, Littlefield RB, Schup-Magoffin PJ and Christman KL. Naturally derived myocardial matrix as an injectable scaffold for cardiac tissue engineering. *Biomaterials*. 2009;30:5409-5416.

131. Singelyn JM, Sundaramurthy P, Johnson TD, Schup-Magoffin PJ, Hu DP, Faulk DM, Wang J, Mayle KM, Bartels K, Salvatore M, Kinsey AM, Demaria AN, Dib N and Christman KL. Catheter-deliverable hydrogel derived from decellularized ventricular extracellular matrix increases endogenous cardiomyocytes and preserves cardiac function post-myocardial infarction. *Journal of the American College of Cardiology*. 2012;59:751-763.

132. Johnson TD, Braden RL and Christman KL. Injectable ECM scaffolds for cardiac repair. *Methods Mol Biol*. 2014;1181:109-20.

133. Yu T, Wang W, Nassiri S, Kwan T, Dang C, Liu W and Spiller KL. Temporal and spatial distribution of macrophage phenotype markers in the foreign body response to glutaraldehyde-crosslinked gelatin hydrogels. *J Biomater Sci Polym Ed*. 2016;27:721-42.

134. Sadtler K, Estrellas K, Allen BW, Wolf MT, Fan H, Tam AJ, Patel CH, Luber BS, Wang H, Wagner KR, Powell JD, Housseau F, Pardoll DM and Elisseeff JH. Developing a pro-

regenerative biomaterial scaffold microenvironment requires T helper 2 cells. *Science*. 2016;352:366-70.

135. Muhamed J, Revi D, Rajan A, Geetha S and Anilkumar TV. Biocompatibility and Immunophenotypic Characterization of a Porcine Cholecyst-derived Scaffold Implanted in Rats. *Toxicol Pathol*. 2015;43:536-45.

136. Valentin JE, Stewart-Akers AM, Gilbert TW and Badylak SF. Macrophage participation in the degradation and remodeling of extracellular matrix scaffolds. *Tissue Eng Part A*. 2009;15:1687-1694.

137. Badylak SF, Valentin JE, Ravindra AK, McCabe GP and Stewart-Akers AM. Macrophage Phenotype as a Determinant of Biologic Scaffold Remodeling. *Tissue Eng Part A*. 2008;14:1835-1842.

138. Mosser D. The many faces of macrophage activation. *J Leukocyte Biol*. 2003.

139. Porcheray F, Viaud S, Rimaniol A-C, Leone C, Samah B, Dereuddre-Bosquet N, Dormont D and Gras G. Macrophage activation switching: an asset for the resolution of inflammation. *Clin Exp Immunol*. 2005;142:481-489.

140. Gordon S. Alternative activation of macrophages. *Nat Rev Immunol*. 2003.

141. Mantovani A, Sica A and Locati M. Macrophage polarization comes of age. *Immunity*. 2005;23:344-346.

142. Brown BN, Valentin JE, Stewart-Akers AM, McCabe GP and Badylak SF. Macrophage phenotype and remodeling outcomes in response to biologic scaffolds with and without a cellular component. *Biomaterials*. 2009;30:1482-1491.

143. Nassiri S, Zakeri I, Weingarten MS and Spiller KL. Relative Expression of Proinflammatory and Antiinflammatory Genes Reveals Differences between Healing and Nonhealing Human Chronic Diabetic Foot Ulcers. *J Invest Dermatol*. 2015;135:1700-3.

144. Brown BN, Ratner BD, Goodman SB, Amar S and Badylak SF. Macrophage polarization: An opportunity for improved outcomes in biomaterials and regenerative medicine. *Biomaterials*. 2012;33:3792-3802.

145. Reiner SL. Helper T cell differentiation, inside and out. *Current opinion in immunology*. 2001;13:351-5.

146. Pierson RN. Xenogeneic skin graft rejection is especially dependent on CD4+ T cells. *Journal of Experimental Medicine*. 1989;170:991-996.

147. Chakir H, Wang H, Lefebvre DE, Webb J and Scott FW. T-bet/GATA-3 ratio as a measure of the Th1/Th2 cytokine profile in mixed cell populations: predominant role of GATA-3. *Journal of immunological methods*. 2003;278:157-69.

148. Allman A, McPherson T, Badylak S, Merrill L, Kallakury B, Sheehan C, Raeder R and Metzger D. Xenogeneic extracellular matrix grafts elicit a Th2-restricted immune response. *Transplantation*. 2001;71:1631-1640.

149. De Fanis U, Mori F, Kurnat RJ, Lee WK, Bova M, Adkinson NF and Casolaro V. GATA3 up-regulation associated with surface expression of CD294/CRTH2: a unique feature of human Th cells. *Blood*. 2007;109:4343-50.

150. Jenner RG, Townsend MJ, Jackson I, Sun K, Bouwman RD, Young RA, Glimcher LH and Lord GM. The transcription factors T-bet and GATA-3 control alternative pathways of T-cell differentiation through a shared set of target genes. *Proc Natl Acad Sci U S A*. 2009;106:17876-81.

151. Boin F, De Fanis U, Bartlett SJ, Wigley FM, Rosen A and Casolaro V. T cell polarization identifies distinct clinical phenotypes in scleroderma lung disease. *Arthritis Rheum*. 2008;58:1165-74.

152. Kigerl KA, Gensel JC, Ankeny DP, Alexander JK, Donnelly DJ and Popovich PG. Identification of two distinct macrophage subsets with divergent effects causing either neurotoxicity or regeneration in the injured mouse spinal cord. *The Journal of neuroscience : the official journal of the Society for Neuroscience*. 2009;29:13435-44.

153. Badylak SF. Decellularized Allogeneic and Xenogeneic Tissue as a Bioscaffold for Regenerative Medicine: Factors that Influence the Host Response. *Ann Biomed Eng*. 2014;42:1517-1527.

154. Sicari BM, Johnson SA, Siu BF, Crapo PM, Daly KA, Jiang H, Medberry CJ, Tottey S, Turner NJ and Badylak SF. The effect of source animal age upon the in vivo remodeling characteristics of an extracellular matrix scaffold. *Biomaterials*. 2012;33:5524-33.

155. de Souza RR. Aging of myocardial collagen. *Biogerontology*. 2002;3:325-35.

156. Johnson TD, Hill RC, Dzieciatkowska M, Nigam V, Behfar A, Christman KL and Hansen KC. Quantification of decellularized human myocardial matrix: A comparison of six patients. *Proteomics Clin Appl*. 2016;10:75-83.

157. Hempel U, Matthaus C, Preissler C, Moller S, Hintze V and Dieter P. Artificial matrices with high-sulfated glycosaminoglycans and collagen are anti-inflammatory and pro-osteogenic for human mesenchymal stromal cells. *J Cell Biochem*. 2014;115:1561-71.

158. Writing Group M, Mozaffarian D, Benjamin EJ, Go AS, Arnett DK, Blaha MJ, Cushman M, Das SR, de Ferranti S, Despres JP, Fullerton HJ, Howard VJ, Huffman MD, Isasi CR, Jimenez MC, Judd SE, Kissela BM, Lichtman JH, Lisabeth LD, Liu S, Mackey RH, Magid DJ, McGuire DK, Mohler ER, 3rd, Moy CS, Muntner P, Mussolino ME, Nasir K, Neumar RW, Nichol G, Palaniappan L, Pandey DK, Reeves MJ, Rodriguez CJ, Rosamond W, Sorlie PD, Stein J, Towfighi A, Turan TN, Virani SS, Woo D, Yeh RW, Turner MB, American Heart Association Statistics C and Stroke Statistics S. Heart Disease and Stroke Statistics-2016 Update: A Report From the American Heart Association. *Circulation*. 2016;133:e38-360.

159. Saidi RF and Hejazii Kenari SK. Challenges of organ shortage for transplantation: solutions and opportunities. *Int J Organ Transplant Med*. 2014;5:87-96.

160. Galili U. The alpha-gal epitope and the anti-Gal antibody in xenotransplantation and in cancer immunotherapy. *Immunol Cell Biol*. 2005;83:674-86.

161. Vuyyuru R, Patton J and Manser T. Human immune system mice: current potential and limitations for translational research on human antibody responses. *Immunologic research*. 2011;51:257-66.

162. Seung E and Tager AM. Humoral immunity in humanized mice: a work in progress. *J Infect Dis*. 2013;208 Suppl 2:S155-9.

163. Galili U, LaTemple DC and Radic MZ. A sensitive assay for measuring alpha-Gal epitope expression on cells by a monoclonal anti-Gal antibody. *Transplantation*. 1998;65:1129-1132.

164. Livak KJ and Schmittgen TD. Analysis of relative gene expression data using real-time quantitative PCR and the 2(-Delta Delta C(T)) Method. *Methods*. 2001;25:402-8.

165. Christy AL and Brown MA. The Multitasking Mast Cell: Positive and Negative Roles in the Progression of Autoimmunity. *The Journal of Immunology*. 2007;179:2673.

166. Tang L, Jennings TA and Eaton JW. Mast cells mediate acute inflammatory responses to implanted biomaterials. *Proceedings of the National Academy of Sciences*. 1998;95:8841.

167. Thevenot PT, Baker DW, Weng H, Sun MW and Tang L. The pivotal role of fibrocytes and mast cells in mediating fibrotic reactions to biomaterials. *Biomaterials*. 2011;32:8394-403.

168. Christman KL. Biomaterials for tissue repair. *Science*. 2019;363:340.

169. Badylak SF, Valentin JE, Ravindra AK, McCabe GP and Stewart-Akers AM. Macrophage Phenotype as a Determinant of Biologic Scaffold Remodeling. *Tissue Eng Pt A*. 2008;14:1835-1842.

170. Godwin JW, Pinto AR and Rosenthal NA. Macrophages are required for adult salamander limb regeneration. *Proceedings of the National Academy of Sciences*. 2013;110:9415.

171. Allman AJ, McPherson TB, Badylak SF, Merrill LC, Kallakury B, Sheehan C, Raeder RH and Metzger DW. XENOGENEIC EXTRACELLULAR MATRIX GRAFTS ELICIT A TH2-RESTRICTED IMMUNE RESPONSE1. *Transplantation*. 2001;71.

172. Sadtler K, Estrellas K, Allen BW, Wolf MT, Fan H, Tam AJ, Patel CH, Luber BS, Wang H, Wagner KR, Powell JD, Housseau F, Pardoll DM and Elisseeff JH. Developing a pro-regenerative biomaterial scaffold microenvironment requires T helper 2 cells. *Science (New York, NY)*. 2016;352:366-370.

173. Methe KN, Nayakawde N, Banerjee D, Sihlbom C, Agbajogu C, Travnikova G and Olausson M. Differential Activation of Immune Cells for Genetically Different Decellularized Cardiac Tissues. *Tissue Eng Pt A*. 2020.

174. Ibrahim M, Bond J, Medina MA, Chen L, Quiles C, Kokosis G, Bashirov L, Klitzman B and Levinson H. Characterization of the Foreign Body Response to Common Surgical Biomaterials in a Murine Model. *Eur J Plast Surg*. 2017;40:383-392.

175. Avula MN, Rao AN, McGill LD, Grainger DW and Solzbacher F. Foreign body response to subcutaneous biomaterial implants in a mast cell-deficient Kitw-Sh murine model. *Acta Biomaterialia*. 2014;10:1856-1863.

176. Bhattacharya K, Farwell K, Huang M, Kempuraj D, Donelan J, Papaliodis D, Vasiadi M and Theoharides TC. Mast cell deficient W/Wv mice have lower serum IL-6 and less cardiac tissue necrosis than their normal littermates following myocardial ischemia-reperfusion. *Int J Immunopathol Pharmacol*. 2007;20:69-74.

177. Arac A, Grimbaldeston MA, Nepomuceno ARB, Olayiwola O, Pereira MP, Nishiyama Y, Tsykin A, Goodall GJ, Schlecht U, Vogel H, Tsai M, Galli SJ, Bliss TM and Steinberg GK. Evidence that Meningeal Mast Cells Can Worsen Stroke Pathology in Mice. *The American Journal of Pathology*. 2014;184:2493-2504.

178. Jolly S, Detilleux J and Desmecht D. Extensive mast cell degranulation in bovine respiratory syncytial virus-associated paroxystic respiratory distress syndrome. *Vet Immunol Immunopathol*. 2004;97:125-36.

179. Janicki JS, Brower GL and Levick SP. The emerging prominence of the cardiac mast cell as a potent mediator of adverse myocardial remodeling. *Methods in molecular biology (Clifton, NJ)*. 2015;1220:121-139.

180. Wulff BC and Wilgus TA. Mast cell activity in the healing wound: more than meets the eye? *Exp Dermatol*. 2013;22:507-510.

181. Legere SA, Haidl ID, Légaré J-F and Marshall JS. Mast Cells in Cardiac Fibrosis: New Insights Suggest Opportunities for Intervention. *Frontiers in Immunology*. 2019;10.

182. Willenborg S, Eckes B, Brinckmann J, Krieg T, Waisman A, Hartmann K, Roers A and Eming SA. Genetic Ablation of Mast Cells Redefines the Role of Mast Cells in Skin Wound Healing and Bleomycin-Induced Fibrosis. *Journal of Investigative Dermatology*. 2014;134:2005-2015.

183. Lennon EM, Borst LB, Edwards LL and Moeser AJ. Mast Cells Exert Anti-Inflammatory Effects in an IL10^{−/−} Model of Spontaneous Colitis. *Mediators of Inflammation*. 2018;2018:7817360.

184. Shiota N, Nishikori Y, Kakizoe E, Shimoura K, Niibayashi T, Shimbori C, Tanaka T and Okunishi H. Pathophysiological Role of Skin Mast Cells in Wound Healing after Scald Injury: Study with Mast Cell-Deficient W/W^V Mice. *International Archives of Allergy and Immunology*. 2010;151:80-88.

185. Wassenaar JW, Gaetani R, Garcia JJ, Braden RL, Luo CG, Huang D, DeMaria AN, Omens JH and Christman KL. Evidence for Mechanisms Underlying the Functional Benefits of a Myocardial Matrix Hydrogel for Post-MI Treatment. *J Am Coll Cardiol*. 2016;67:1074-1086.

186. Wang RM, Johnson TD, He J, Rong Z, Wong M, Nigam V, Behfar A, Xu Y and Christman KL. Humanized mouse model for assessing the human immune response to xenogeneic and allogeneic decellularized biomaterials. *Biomaterials*. 2017;129:98-110.

187. Traverse JH, Henry TD, Dib N, Patel AN, Pepine C, Schaer GL, DeQuach JA, Kinsey AM, Chamberlin P and Christman KL. First-in-Man Study of a Cardiac Extracellular Matrix Hydrogel in Early and Late Myocardial Infarction Patients. *JACC: Basic to Translational Science*. 2019;4:659.

188. Hasegawa T, Hall CJ, Crosier PS, Abe G, Kawakami K, Kudo A and Kawakami A. Transient inflammatory response mediated by interleukin-1β is required for proper regeneration in zebrafish fin fold. *Elife*. 2017;6.

189. Huleihel L, Dziki JL, Bartolacci JG, Rausch T, Scarritt ME, Cramer MC, Vorobyov T, LoPresti ST, Swineheart IT, White LJ, Brown BN and Badylak SF. Macrophage phenotype in response to ECM bioscaffolds. *Semin Immunol*. 2017;29:2-13.

190. Ando T, Xiao W, Gao P, Namiranian S, Matsumoto K, Tomimori Y, Hong H, Yamashita H, Kimura M, Kashiwakura J-i, Hata Tissa R, Izuhara K, Gurish Michael F, Roers A, Rafaels Nicholas M, Barnes Kathleen C, Jamora C, Kawakami Y and Kawakami T. Critical Role for Mast Cell Stat5 Activity in Skin Inflammation. *Cell Reports*. 2014;6:366-376.

191. Villa A, Rizzi N, Vegeto E, Ciana P and Maggi A. Estrogen accelerates the resolution of inflammation in macrophagic cells. *Scientific Reports*. 2015;5:15224.

192. Vliagoftis H, Dimitriadou V, Boucher W, Rozniecki JJ, Correia I, Raam S and Theoharides TC. Estradiol augments while tamoxifen inhibits rat mast cell secretion. *Int Arch Allergy Immunol*. 1992;98:398-409.

193. You HJ, Kim JY and Jeong HG. 17 beta-estradiol increases inducible nitric oxide synthase expression in macrophages. *Biochem Biophys Res Commun*. 2003;303:1129-34.

194. Dai R, Phillips RA, Karpuzoglu E, Khan D and Ahmed SA. Estrogen regulates transcription factors STAT-1 and NF-kappaB to promote inducible nitric oxide synthase and inflammatory responses. *J Immunol*. 2009;183:6998-7005.

195. Zierau O, Zenclussen AC and Jensen F. Role of female sex hormones, estradiol and progesterone, in mast cell behavior. *Frontiers in immunology*. 2012;3:169-169.

196. Aurora AB, Porrello ER, Tan W, Mahmoud AI, Hill JA, Bassel-Duby R, Sadek HA and Olson EN. Macrophages are required for neonatal heart regeneration. *J Clin Invest*. 2014;124:1382-92.

197. Higgins DM, Basaraba RJ, Hohnbaum AC, Lee EJ, Grainger DW and Gonzalez-Juarrero M. Localized Immunosuppressive Environment in the Foreign Body Response to Implanted Biomaterials. *The American Journal of Pathology*. 2009;175:161-170.

198. Ungerleider JL, Johnson TD, Rao N and Christman KL. Fabrication and characterization of injectable hydrogels derived from decellularized skeletal and cardiac muscle. *Methods*. 2015;84:53-59.

199. Jardine L, Wiscombe S, Reynolds G, McDonald D, Fuller A, Green K, Filby A, Forrest I, Ruchaud-Sparagano M-H, Scott J, Collin M, Haniffa M and Simpson AJ.

Lipopolysaccharide inhalation recruits monocytes and dendritic cell subsets to the alveolar airspace. *Nature Communications*. 2019;10:1999.

200. Hussain S, Johnson CG, Sciurba J, Meng X, Stober VP, Liu C, Cyphert-Daly JM, Bulek K, Qian W, Solis A, Sakamachi Y, Trempus CS, Aloor JJ, Gowdy KM, Foster WM, Hollingsworth JW, Tighe RM, Li X, Fessler MB and Garantziotis S. TLR5 participates in the TLR4 receptor complex and promotes MyD88-dependent signaling in environmental lung injury. *Elife*. 2020;9.

201. Waggott D, Chu K, Yin S, Wouters BG, Liu F-F and Boutros PC. NanoStringNorm: an extensible R package for the pre-processing of NanoString mRNA and miRNA data. *Bioinformatics (Oxford, England)*. 2012;28:1546-1548.

202. Wang H, Horbinski C, Wu H, Liu Y, Sheng S, Liu J, Weiss H, Stromberg AJ and Wang C. NanoStringDiff: a novel statistical method for differential expression analysis based on NanoString nCounter data. *Nucleic Acids Research*. 2016;44:e151-e151.

203. Yu G, Wang L-G, Han Y and He Q-Y. clusterProfiler: an R Package for Comparing Biological Themes Among Gene Clusters. *OMICS: A Journal of Integrative Biology*. 2012;16:284-287.

204. Blighe K RS, Lewis M (2020). EnhancedVolcano: Publication-ready volcano plots with enhanced colouring and labeling. R package version 1.6.0.

205. Bassat E, Mutlak YE, Genzelinakh A, Shadrin IY, Baruch Umansky K, Yifa O, Kain D, Rajchman D, Leach J, Riabov Bassat D, Udi Y, Sarig R, Sagi I, Martin JF, Bursac N, Cohen S and Tzahor E. The extracellular matrix protein agrin promotes heart regeneration in mice. *Nature*. 2017;547:179-184.

206. Baehr A, Umansky Kfir B, Bassat E, Jurisch V, Klett K, Bozoglu T, Hornaschewitz N, Solyanik O, Kain D, Ferraro B, Cohen-Rabbi R, Krane M, Cyran C, Soehnlein O, Laugwitz Karl L, Hinkel R, Kupatt C and Tzahor E. Agrin Promotes Coordinated Therapeutic Processes Leading to Improved Cardiac Repair in Pigs. *Circulation*. 0.

207. Williams C, Quinn KP, Georgakoudi I and Black LD, 3rd. Young developmental age cardiac extracellular matrix promotes the expansion of neonatal cardiomyocytes in vitro. *Acta biomaterialia*. 2014;10:194-204.